Measurement of time integrated CP asymmetry in $D^0 \to K_S^0 K_S^0$ decay at Belle and Belle II experiments

Submitted in partial fulfillment for the award of degree of

Doctor of Philosophy

in

Physics

by

Sanjeeda Bharati Das
2018RPY9055

Under the supervision of
Dr. Kavita Lalwani

DEPARTMENT OF PHYSICS

MALAVIYA NATIONAL INSTITUTE OF TECHNOLOGY JAIPUR

Declaration

I, Sanjeeda Bharati Das, declare that this thesis titled, **"Measurement of time integrated CP Asymmetry in $D^0 \to K^0_s K^0_s$ decay at Belle and Belle II experiments"** and the work presented in it, are my own. I confirm that:

- This work was done wholly or mainly while in candidature for a research degree at this institute.
- Where any part of this thesis has previously been submitted for a degree or any other qualification at this university or any other institution, this has been clearly stated.
- Where I have consulted the published work of others, this is always clearly attributed.
- Where I have quoted from the work of others, the source is always given. With the exception of such quotations, this thesis is entirely my own work.
- I have acknowledged all main sources of help.
- Where the thesis is based on work done by myself, jointly with others, I have made clear exactly what was done by others and what I have contributed myself.

Date:

Sanjeeda Bharati Das
(2018RPY9055)

Certificate

This is to certify that the thesis titled **"Measurement of time integrated CP asymmetry in $D^0 \to K_S^0 K_S^0$ decay at Belle and Belle II experiments"** submitted by Ms. Sanjeeda Bharati Das (2018RPY9055) is a bonafide research work carried out under my supervision and guidance in fulfillment of the requirement for the award of the degree of Doctor of Philosophy in the Department of Physics, Malaviya National Institute of Technology Jaipur, India. The matter embodied in this thesis is original and has not been submitted to any other university or institute for the award of any other degree.

Dr. Kavita Lalwani (Supervisor)
Assistant Professor
Department of Physics
MNIT Jaipur

Date:

Place:

Acknowledgement

First of all, I would like to express my gratitude to the Almighty, for giving me the patience and strength for the completion of my thesis.

I would want to thank my PhD supervisor, Dr. Kavita Lalwani, for all of his help and support during this time. I owe her a debt of gratitude for the last five and a half years of patiently and encouragingly coaching me. I also want to thank him for giving me the wonderful chance and tools to work on the Belle and Belle II collaborations. I want to thank Dr. Angelo Di Canto, associate physicist at Brookhaven National Laboratory, New York, USA who has always provided me with prompt assistance with the analysis throughout the course of my PhD. This thesis would not have been possible without his dedicated supervision, advice and constructive criticisms. I consider myself privileged to have worked with him.

I am grateful to the Belle and Belle II collaboration for giving me the opportunity to work at KEK and for providing financial support during my visit. My sincere gratitude to Dr. Katsuro Nakamura for hosting me during the Athena program.

I would like to express my gratitude to all of the members of the Belle India Group who helped and supported me throughout my doctorate, particularly the faculty members of the partner institutions who started the Belle analysis workshops (BAW), which give us an opportunity to interact with our peers.

I thank the Ministry of Human Resource and Development, Govt. of India for financial support during my PhD. I am grateful to all of the faculty members and non-teaching staff at MNIT Jaipur's Department of Physics for their support.

I extend gratitude to my seniors and colleagues: Dr. Manish Chahal, Dr. Karam Chand, my collegues Chanchal Sharma, Priyanka Boora, Dr. Deepak Negi, Dr. Jaspreet Kaur, Ruksar Sultana, Chinu S Kumar, Meenu Suhag, Anuj Malik, Dr. Pooja Pareek, Jyoti Lakhera, Saisandri Saini, Radhika Goswami and Monika Shrivastav who would never let me feel low during my stay at MNIT.

Lastly, I thank my grandmother, parents, Bu, Pishu, Naireet, Tua, Tureen, Anil and my dog Shinu for their unconditional love and support.

Abstract

The Belle detector, a versatile magnetic spectrometer offering extensive solid angle coverage, is specifically crafted for investigating the Charge-conjugation-Parity (CP) violation asymmetry in the decays of B and D mesons. Positioned at the interaction region in Tsukuba, Japan, featuring a 1.5 T superconducting solenoid along with iron structure and it accumulated close to 1 ab^{-1} of data at various center-of-mass energies.

Belle II, the successor to Belle and a second-generation B-factory, is currently under operational in Tsukuba, Japan. As an experiment at the intensity frontier, Belle II aims to amass a data sample approximately 50 times larger than its predecessor (Belle). The primary objective is to unveil physics beyond the standard model (SM), commonly referred to as New Physics (NP), through precise investigations of rare or suppressed decays. In essence, Belle II represents a dedicated pursuit of New Physics.

We measure the time-integrated CP asymmetry, $\mathcal{A}_{CP}$, in $D^0 \to K^0_S K^0_S$ decays reconstructed in $e^+e^- \to c\bar{c}$ events collected by Belle and Belle II. The full Belle data sample is used, corresponding to an integrated luminosity of $980\,\text{fb}^{-1}$. For Belle II, the data collected before Long Shutdown 1 (LS1) are used, and correspond to an integrated luminosity of $420\,\text{fb}^{-1}$. The D^0 decays are required to come from the flavor-conserving $D^{*+} \to D^0\pi^+$ decay (D^{*+} tag) to determine the charm flavor at production time. A control sample of D^{*+}-tagged $D^0 \to K^+K^-$ is used to correct for production and detection asymmetries.

I also participated in the particle identification of charged pions using $K^0_S \to \pi^+\,\pi^-$ decays in the context of the `Belle II Systematics Correction Framework`. I have also contributed to studying the data/MC comparison of the cluster properties of the Belle II Silicon Vertex Detector.

Contents

List of Figures

List of Tables

Chapter 1

Introduction

The Standard Model (SM) of particle physics is the most successful explanation of matter, but it cannot provide an explanation for the matter-antimatter asymmetry. One of the conditions for matter-antimatter asymmetry is Charge Parity Violation (*CP* Violation or CPV), suggested by Andrei Sakharov [1]. In the SM, CPV is caused due to an irreducible phase in the Cabbibo Kobayashi Maskawa (CKM) matrix [2,3]. This phase is not enough to account for the extent of the matter-antimatter asymmetry of the universe. While the K and the B meson systems have been studied extensively in this regard, the D meson sector is relatively unexplored. Nonetheless, the charm sector is viewed with renewed interest after the discovery of *CP* violation in decays of neutral charm mesons that has recently been observed by LHCb by measuring the difference between the *CP* asymmetries in $D^0 \to \pi^+\pi^-$ and $D^0 \to K^+K^-$ decays [4].

Charmed hadrons are unique because the charm quark in them is the only '*up*' type quark can transition into a '*down*' type quark. This feature makes charmed hadrons a special tool to probe *CP* Violating couplings which may not present in the $K$and B sector.

In this chapter, the rationale behind the analysis performed in this thesis are introduced, following a brief overview of the theoretical background, where we address the linkages between the charmed meson decays and *CP* violation in the SM.

1.1 Literature review

This section gives a chronological introduction to *CP* violation and also provides a review of the formalism that is developed to describe *CP* violation in the standard model, in particular for the decays of neutral mesons.

1.1.1 CP Violation

Symmetries play a pivotal role in nature. As per the Noether's theorem, these symmetries lead to conservation laws [5]. In this section, we focus on *CP* violation, where 'C' denotes the charge conjugation and 'P' stands for parity. The 'C' and 'P' are two discrete symmetries of nature, studied in Particle Physics. The operation of charge conjugation changes the sign of all the quantum numbers that follow the laws of simple scalar addition leaving all other quantities like position, momentum and spin unchanged. To understand better, we can consider the case of the neutral pion (π^0) and the neutron. The π^0 is its own anti-particle, as it has no spin whereas, the neutron has a distinct anti-neutron. The parity operator on the other hand inverts the spatial dimensions, leaving other variables unchanged. In variance of the laws of physics under the *CP* operation implies that *CP* is conserved.

Prior to 1950s, C,P and T were believed to be conserved in all interactions, where 'T' is the time reversal operator, which inverts the temporal dimension of space-time ($t \to -t$). In 1956, two theoretical physicists C.N. Yang and T.D. Lee demonstrated that there parity invariance was not supported by any evidence [6]. The following year's experiments unequivocally confirmed that parity is broken in the beta decays of both pions and nuclear matter [7,8]. These experiment also revealed charge conjugation asymmetry. It was thus proved that C and P are not separately conserved in nature. *CP* was thus established as a symmetry of nature.

In 1964, Cronin and Fitch found the first evidence of *CP* violation in the neutral K meson system [9]. The neutral kaons were expected to decay into three pions only but in the experiment it was found that only neutral kaons decay into two pions in a small percentage of the time thereby violating the *CP* symmetry. This experiment also led to the introduction of a new quantum number "*strangeness*" *(S)* to describe the kaons. The problem of the observed phenomenology of neutral kaons remained unresolved till 1973, when Kobayashi and Maskawa hypothesised that the occurrence of a complex phase, if are at least six quarks, may accommodate *CP* violation in the electroweak model [3]. However only u, d and s quarks were known to exist till then. Eventually, in 1974 and 1977, respectively, the charm [10,11] and bottom [12] quarks were confirmed to exist. The top quark, or sixth particle, was not found until 1995 [13,14].

The Kobayashi- Maskawa hypothesis was confirmed for the first time, when direct *CP* violation was discovered in the neutral kaons system through the $K^0 \to \pi^0\pi^0$ decay [15,16]. More pronounced effects were observed in the $B^0 - \bar{B}^0$ system [17,18] and in two-body charmless decays of B^0 [19,20].

1.1.2 CP violation in the Standard Model

After the first observation of CPV, it took about a decade to understand it in the SM. In 1973, Kobayashi and Maskawa extended the formalism (which was originally developed by Cabibbo [2]) to accommodate three generations of quarks, even though only u, d and s quarks were discovered till then. Kobayashi and Maskawa showed that a *CP* violating complex phase arises in the quark mixing matrix, called the CKM matrix [2,3], named after Cabibbo, Kobayashi and Maskawa. At the current stage, there are three quark generations. Each of these generations are made up of an *up* type quark with charge

$+(2/3)e$ and a *down* type quark with charge $-(1/3)e$. The up type quarks are *up*, *charm* and *top* and their corresponding down type quarks are *down*, *strange* and *beauty*. These quarks participate in mixing via the exchange of a $W^{\pm}$ boson and the quark mixing matrix is called the CKM matrix.

$$\begin{bmatrix} d' \\ s' \\ b' \end{bmatrix} = \begin{bmatrix} V_{ud} & V_{us} & V_{ub} \\ V_{cd} & V_{cs} & V_{cb} \\ V_{td} & V_{ts} & V_{tb} \end{bmatrix} \begin{bmatrix} d \\ s \\ b \end{bmatrix} \tag{1.1}$$

The weak eigen states are denoted by prime. The probability of a quark transition is decided by the matrix elements $V_{ij}(i,j = u,d,c,s,t,b)$. Any $n \times n$ unitary matrix can be parameterized by n^2 real parameters, out of which $(2n-1)$ parameters can be eliminated by re-phasing the quarks, while $(n-1)/2$ parameters are left. In addition, the CKM matrix is orthogonal and has $n(n-1)/2$ parameters, that correspond to the independent rotation angles. The $(n-1)(n-2)/2$ parameters are the complex phases. The CKM matrix is an 3×3 unitary matrix. So, it can be parameterized by 9 real parameters, out of which 5 can be eliminated by re-phasing the quarks. Out of the 4 remaining parameters, 3 are the Euler angles and one phase. As per the Chau Keung parametrization [21], the CKM matrix can be written as:

$$V_{CKM} = \begin{bmatrix} 1 & 0 & 0 \\ 0 & c_{23} & s_{23} \\ 0 & -s_{23} & c_{23} \end{bmatrix} \begin{bmatrix} c_{13} & 0 & s_{13}e^{-i\delta} \\ 0 & 1 & 0 \\ -s_{13}e^{-i\delta} & 0 & c_{13} \end{bmatrix} \begin{bmatrix} c_{12} & s_{12} & 0 \\ -s_{12} & c_{12} & 0 \\ 0 & 0 & 1 \end{bmatrix} \tag{1.2}$$

$$V_{CKM} = \begin{bmatrix} c_{12}c_{13} & s_{12}c_{13} & s_{13}e^{-i\delta} \\ -s_{12}c_{23} - c_{12}s_{23}s_{13}e^{i\delta} & c_{12}c_{23} - s_{12}s_{23}s_{13}e^{i\delta} & s_{23}c_{13} \\ s_{12}s_{23} - c_{12}c_{23}s_{13}e^{i\delta} & -c_{12}s_{23} - s_{12}c_{23}s_{13}e^{i\delta} & c_{23}c_{13} \end{bmatrix} \tag{1.3}$$

$s_{ij} \equiv sin\theta_{ij}$ and $c_{ij} \equiv cos\theta_{ij}$, θ_{12} is the Cabibbo angle and δ is the phase, which changes sign when the *CP* operation is performed, indicating *CP* Violation. The value of the diagonal elements of V_{CKM} are close to 1 and the other elements have a considerably smaller value. This implies that quark level transitions within the generation are favoured while inter-generational transitions are not. The observed hierarchy is $s_{13} << s_{23} << s_{12} << 1$. Exploiting this hierarchy, another parametrization if the CKM matrix was developed by Wolfenstien [22], wherein, every matrix element is expressed as a power series in $\lambda \equiv sin\theta_c \approx 0.23$. The four independent real parameters are

$$s_{12} \equiv \lambda, \quad s_{23} \equiv A\lambda^2, \quad s_{13}e^{-i\delta} \equiv A\lambda^3(\rho - i\eta) \tag{1.4}$$

The CKM matrix can thus be written as

$$V_{CKM} = \begin{bmatrix} 1-\frac{\lambda^2}{2} & \lambda & A\lambda^3(\rho - i\eta) \\ -\lambda & 1-\frac{\lambda^2}{2} & A\lambda^2 \\ A\lambda^3(1-\rho-i\eta) & -A\lambda^2 & 1 \end{bmatrix} + \mathcal{O}(\lambda^4) \tag{1.5}$$

The orthogonality relations between the elements of V_{CKM} is given by

$$\sum_{k\epsilon\{u,c,t\}} = V^*_{k\alpha}V_{k\beta} = \delta_{\alpha\beta}, \quad \alpha, \beta\epsilon\{d, s, b\} \tag{1.6}$$

This gives us a total of 9 equations, out of which 6 equations satisfy $\delta_{\alpha\beta} = 0$.

$$\underbrace{V_{ud}V^*_{us}}_{\mathcal{O}(\lambda)} + \underbrace{V_{cd}V^*_{cs}}_{\mathcal{O}(\lambda)} + \underbrace{V_{td}V^*_{ts}}_{\mathcal{O}(\lambda^5)} = 0 \tag{1.7}$$

$$\underbrace{V_{ud}V^*_{cd}}_{\mathcal{O}(\lambda)} + \underbrace{V_{us}V^*_{cs}}_{\mathcal{O}(\lambda)} + \underbrace{V_{ub}V^*_{cb}}_{\mathcal{O}(\lambda^5)} = 0 \tag{1.8}$$

$$\underbrace{V_{us}V^*_{ub}}_{\mathcal{O}(\lambda^4)} + \underbrace{V_{cs}V^*_{cb}}_{\mathcal{O}(\lambda^2)} + \underbrace{V_{ts}V^*_{tb}}_{\mathcal{O}(\lambda^2)} = 0 \tag{1.9}$$

$$\underbrace{V_{cd}V^*_{td}}_{\mathcal{O}(\lambda^4)} + \underbrace{V_{cs}V^*_{ts}}_{\mathcal{O}(\lambda^2)} + \underbrace{V_{cb}V^*_{tb}}_{\mathcal{O}(\lambda^2)} = 0 \tag{1.10}$$

$$\underbrace{V_{ud}V^*_{ub}}_{\mathcal{O}(\lambda^3)} + \underbrace{V_{cd}V^*_{cb}}_{\mathcal{O}(\lambda^3)} + \underbrace{V_{td}V^*_{tb}}_{\mathcal{O}(\lambda^3)} = 0 \tag{1.11}$$

$$\underbrace{V_{ud}V^*_{td}}_{\mathcal{O}(\lambda^3)} + \underbrace{V_{us}V^*_{ts}}_{\mathcal{O}(\lambda^3)} + \underbrace{V_{us}V^*_{tb}}_{\mathcal{O}(\lambda^3)} = 0 \tag{1.12}$$

The six distinct conditions can be represented as six different triangles in the complex plane. Although the shapes are very different (as implied by the order of λ), each of them have the same area, which is proportional to

$$\Delta = Im(V^*_{cs}V_{us}V_{cd}V^*_{ud}), \tag{1.13}$$

when each side is expressed in powers of λ. CP violation is implied by the fact that none of the triangles are reduced to a line. the equations 1.7 to 1.12 are all *unitary triangles*, but traditionally, the term *unitary triangle* is used only for Equation (1.11) only. As shown in Figure 1.1, the apex of the triangle is denoted by $(\bar{\rho}, \bar{\eta})$.

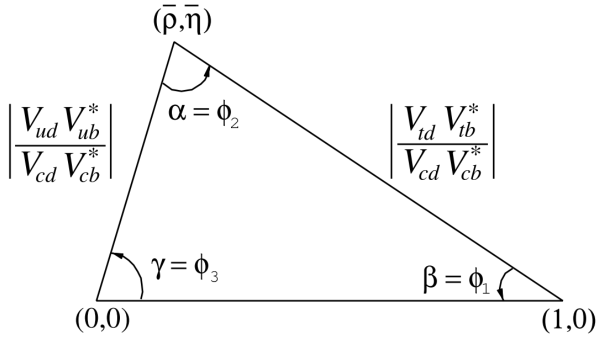

Figure 1.1: Illustration of the unitarity triangle in the $\bar{\rho} - \bar{\eta}$ plane [23].

The angles of the triangle are given by:

$$\phi_1 = \beta \equiv \arg\left(\frac{-V_{cd}V_{cb}}{V_{tb}V_{td}}\right) \tag{1.14}$$

$$\phi_2 = \alpha \equiv \arg\left(\frac{-V_{td}V_{tb}}{V_{ud}V_{ub}}\right) \tag{1.15}$$

$$\phi_3 = \alpha \equiv \arg\left(\frac{-V_{ud}V_{ub}}{V_{cd}V_{cb}}\right) \tag{1.16}$$

1.1.3 CP violation in neutral charm meson decays

After learning how *CP* violation occurs in the SM from the preceding section, we now develop the formalism to understand the phenomenology of *CP* violation in meson decays. We first introduce certain notations that hold good for all pseudoscalar mesons. Our course of care largely resembles the one described in [24].

$c\overline{u} \rightarrow s\overline{s}$ and $c\overline{u} \rightarrow d\overline{d}$, singly Cabibbo suppressed decays have final state particles that are common to both D^0 and $\overline{D}^0$ decays. The final states can be *CP* eigen states or non-*CP* eigen states. To develop the formalism, the following standard notations are used:

$$\tau = \Gamma_D t \qquad \Gamma_D \equiv \frac{\Gamma_{D_H} + \Gamma_{D_L}}{2}$$

$$A_f \equiv A(D^0 \rightarrow f) \qquad \bar{A}_f \equiv A(\overline{D}^0 \rightarrow f)$$

$$A_{\bar{f}} \equiv A(D^0 \rightarrow \bar{f}) \qquad \bar{A}_{\bar{f}} \equiv A(D^0 \rightarrow \bar{f})$$

$$x \equiv \frac{\Delta m_D}{\Gamma_D} \equiv \frac{m_{D_H} - m_{D_L}}{\Gamma_D} \qquad y \equiv \frac{\Delta m_D}{2\Gamma_D} \equiv \frac{\Gamma_{D_H} - \Gamma_{D_L}}{2\Gamma_D}$$

$$\lambda_f \equiv \frac{q}{p}\frac{\bar{A}_f}{A_f} \qquad R_m \equiv |\frac{q}{p}| \qquad r_f \equiv |\frac{\bar{A}_f}{A_f}|,$$

where D_H and D_L denote heavy and light eigen states. The definitions of q and p are defined with the equation $|D_{H,L}\rangle = p|D^0\rangle \mp q|\overline{D}^0\rangle$.

The time dependent decay rate of a $\overline{D}^0$ decaying into final state f is given by Equation (1.17) and Equation (1.18):

$$\Gamma(D^0(t) \to f) = \frac{1}{2}e^{-\tau}|A_f|^2(1+|\lambda_f|^2)\cosh(y\tau) + (1-|\lambda_f|^2)\cos(x\tau) + \\ 2\mathcal{R}e(\lambda_f) \times \sinh(y\tau) - 2\mathcal{I}m(\lambda_f)\sin(x\tau) \quad (1.17)$$

$$\Gamma(\overline{D}^0(t) \to f) = \frac{1}{2}e^{-\tau}|\bar{A}_f|^2(1+|\lambda_f^{-1}|^2)\cosh(y\tau) + (1-|\lambda_f|^{2^{-1}})\cos(x\tau) + \\ 2\mathcal{R}e(\lambda_f^{-1}) \times \sinh(x\tau) - 2\mathcal{I}m(\lambda_f^{-1})\sin(x\tau) \quad (1.18)$$

The time integrated decay rates are given by Equation (1.19) and Equation (1.20)

$$\Gamma(D^0(t) \to f) = \int_0^\infty \Gamma(D^0(t) \to f)dt \\ = \frac{1}{2}|A_f|^2 \left\{(1+|\lambda_f|^2)\frac{1}{1-y^2} + (1-|\lambda_f|^2)\frac{1}{1+x^2} + 2\mathcal{R}e(\lambda_f)\frac{y}{1-y^2} + 2\mathcal{I}m(\lambda_f)\frac{x}{1+x^2}\right\} \quad (1.19)$$

$$\Gamma(\overline{D}^0(t) \to f) = \int_0^\infty \Gamma(\overline{D}^0(t) \to f)dt \\ = \frac{1}{2}|\bar{A}_f|^2 \left\{(1+|\lambda_f^{-1}|^2)\frac{1}{1-y^2} + (1-|\lambda_f^{-1}|^2)\frac{1}{1+x^2} + 2\mathcal{R}e(\lambda_f^{-1})\frac{y}{1-y^2} - 2\mathcal{I}m(\lambda_f^{-1})\frac{x}{1+x^2}\right\} \quad (1.20)$$

Corresponding expressions for $A_{\bar{f}}$ and $\bar{A}_{\bar{f}}$ can be obtained by replacing f to $\bar{f}$. Hence the four decay amplitudes can be written as:

$$A_f = A_f^T e^{+i\phi_f^T}[1 + r_f e^{i(\delta_f + \phi_f)}] \quad (1.21)$$
$$A_{\bar{f}} = A_{\bar{f}}^T e^{i(\Delta f + \phi_{\bar{f}}^T)}[1 + r_f e^{i(\delta_{\bar{f}} + \phi_{\bar{f}})}] \quad (1.22)$$
$$\bar{A}_{\bar{f}} = A_f^T e^{i\phi_f^T}[1 + r_f e^{i(\delta_f - \phi_f)}] \quad (1.23)$$
$$\bar{A}_f = A_f^T e^{i(\Delta f - \phi_{\bar{f}}^T)}[1 + r_{\bar{f}} e^{i(\delta_{\bar{f}} - \phi_{\bar{f}})}] \quad (1.24)$$

Here$A_f^T e^{\pm i\phi_f^T}$ is the SM-tree level contribution. The weak *CP* violating phases are ϕ_f^T, $\phi_{\bar{f}}^T$, ϕ_f and $\phi_{\bar{f}}$. The *CP* conserving phases are Δ_f and δ_f. On neglecting terms of order $|(V_{ub}V_{cb})/V_{us}V_{cs}| \approx 10^{-3}$, we get $\phi_f^T = \phi_{\bar{f}}^T$ to be the same for all states. For *CP* odd states, $\Delta_f\pi(0)$, the amplitudes can then be written as:

$$A_f = A_f^T e^{+i\phi_f^T}[1 + r_f e^{i(\delta_f+\phi_f)}] \tag{1.25}$$

$$\eta_f^{CP} \bar{A}_f = A_f^T e^{-i\phi_i^T}[1 + r_f e^{i(\delta_f-\phi_f)}]. \tag{1.26}$$

Here, $\eta_f^{CP} = -(+)$ for *CP* odd(even) states. Neglecting r_f, we get

$$\lambda_f \equiv -\eta_f^{CP} R_m e^{i\phi} \tag{1.27}$$

where, ϕ is the weak phase between the mixing amplitude and decay amplitude.

The time integrated *CP* asymmetry for a final *CP* eigen state f is written as

$$a_f \equiv \frac{\Gamma(D^0 \to f) - \Gamma(\overline{D}^0 \to f)}{\Gamma(D^0 \to f) + \Gamma(\overline{D}^0 \to f)}. \tag{1.28}$$

Expanding to leading order in these parameters and considering experimental constraints: $x, y, r_f << 1$, Equation (1.28) can be written as

$$a_f = a_f^d + a_f^m + a_f^i. \tag{1.29}$$

The meaning of each term in Equation (1.29) is explained below.

- $\boldsymbol{a_f^d}$ denotes *CP* violation in decay or direct *CP* violation. In the decays of charged mesons, this is the only possible source of *CP* asymmetries as mixing effects are absent.
$$a_f^d = 2r_f \sin\phi_f \sin\delta_f. \tag{1.30}$$

- $\boldsymbol{a_f^m}$ signifies *CP* violation in mixing. Considering our approximations, a_f^m is universal.
$$a_f^m = -\eta_f^{CP} \frac{y}{2}(R_m - R_m^{-1})\cos\phi \tag{1.31}$$

- $\boldsymbol{a_f^i}$ stands for *CP* violation in the interference of decays with and without mixing. This term is also universal within our approximations.
$$a_f^i = -\eta_f^{CP} \frac{x}{2}(R_m + R_m^{-1})\sin\phi. \tag{1.32}$$

Another observable can be constructed using a_f^m and a_f^i which is:

$$\Delta Y_f = \frac{\hat{\Gamma}_{\overline{D}^0 \to f} - \hat{\Gamma}_{D^0 \to f}}{2\Gamma_D} = a^m + a^i. \tag{1.33}$$

It is to be noted that a^m and a^i contribute to both Equation (1.28) and to Equation (1.33). a_f^d contributes only to Equation (1.33). Thus, *CP* violation in meson decays can be classified into three types. The necessary conditions corresponding to each type of *CP* violation are mentioned below.

- ***CP* violation in decay:** This type of *CP* violation is also known as **direct *CP* violation**. The *CP* violating observable is:

$$a^d \equiv \frac{\Gamma(D^0 \to f) - \Gamma(\overline{D}^0 \to f)}{\Gamma(D^0 \to f) + \Gamma(\overline{D}^0 \to f)} = \frac{1 - \left|\frac{\bar{A}_f}{A_{\bar{f}}}\right|}{1 + \left|\frac{\bar{A}_f}{A_f}\right|} \tag{1.34}$$

  The necessary condition for this type of *CP* violation is $\left|\frac{\bar{A}_{\bar{f}}}{A_f}\right| \neq 1$.

- ***CP* violation in mixing:** The *CP* violating observable in this case is

$$a^m = \frac{1 - \left|\frac{q}{p}\right|^4}{1 + \left|\frac{q}{p}\right|^4} \tag{1.35}$$

  and the necessary condition for it is $\left|\frac{q}{p}\right| \neq 1$.

- ***CP* violation in mixing:** The necessary condition for this type of *CP* violation is $\mathcal{I}m(\lambda) \neq 0$.

Charge-parity (*CP*) violation in the charm sector has recently been observed by LHCb as a difference between the *CP* asymmetries of $D^0 \to K^+K^-$ and $D^0 \to \pi^+\pi^-$ decays [4].[1] A more recent measurement has determined that *CP* violation occurs primarily in the $D^0 \to \pi^+\pi^-$ mode [25]. However, the origin of the observed *CP*-violation signal is not fully understood and there is a debate on whether it can be due to physics beyond the standard model [26]. This motivates additional measurements of *CP* asymmetries in two-pseudoscalar modes to evaluate predictions based on the pattern of $SU(3)_F$ breaking in charm decays [27, 28].

The Belle and Belle II experiments at KEK, Japan provides an ideal environment for the measurement of *CP* violation observables. These experimental facilities are described in Chapter 2. The complete analysis of the data collected by Belle and Belle II for the measurement of *CP* asymmetry in $D^0 \to K^0_S K^0_S$ decays is described in detail in Chapter 3. The evaluation of systematic uncertainties and final results from the analysis are documented in Chapter 4. Contributions to the `Belle II systematic framework` are highlighted in Chapter 5, in which as study of particle identification of low momentum pions are performed. A study of the cluster properties for the Belle II Silicon Vertex Detector (SVD) is presented in Chapter 6, followed by a conclusion in Chapter 7.

[1] Throughout this thesis, charge-conjugate modes are implied unless stated otherwise.

Chapter 2

Experimental facility

The data samples gathered by the Belle and Belle II experiments are used to analyse the D^{*+}- tagged decays $D^0 \to K_S^0 K_S^0$ (signal mode) $D^0 \to K^+K^-$ (control mode). Located at the SuperKEKB accelerator's interaction point, the Belle II detector is a significant upgrade of the Belle detector. The High Energy Accelerator Research Organisation (KEK) in Tsukuba, Japan is home to both of these accelerators. The KEK accelerator corresponds to the Belle detector, while SuperKEKB and Belle II are their respective successors. An overview of these two accelerators and the matching detectors is included in this chapter.

2.1 The Belle Experiment

2.1.1 KEKB accelerator

The KEKB [29]is an asymmetric electron (e^-) - positron (e^+) collider with respective energies 8 GeV and 3.5 GeV. It is located at KEK (K$\bar{o}$Enerugi Kasokuki Kenky$\bar{u}$Kik$\bar{o}$), Tsukuba, Japan and is 11 meters underground. It was built side by side in the TRISTAN tunnel (built in the period 1981-1986 to search for $t\bar{t}$ pairs). Two storage rings of the KEKB accelerator are namely: High Energy Ring (HER) for electrons and Low Energy Ring (LER) for positrons. Each of these rings are about 3 km in circumference. The electrons are produced by an electron gun using the process of thermionic emission and accelerated in to the Linear Accelerator (LINAC). For the production of positrons, a tungsten mono crystal target is hitted with the electrons. The process radiates photons and e^- e^+ pairs are created and separated using magnetic field. Figure 2.1 shows a schematic of the accelerator complex.

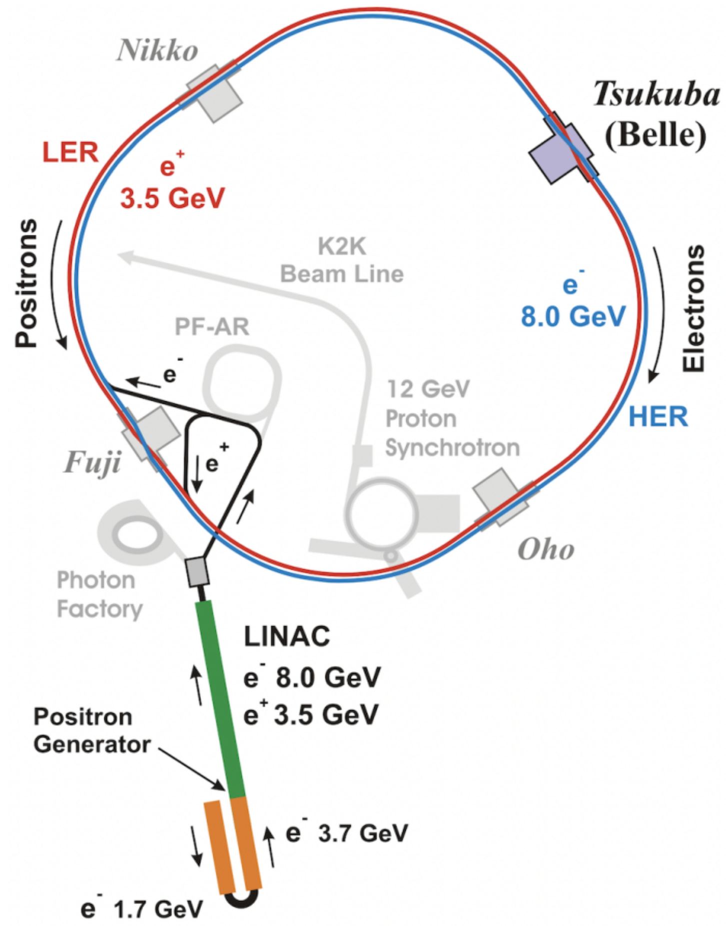

Figure 2.1: A Schematic of the KEKB accelerator complex [29].

Then, the e^- and e^+ beams are fed to the HER and LER ,respectively and injected into the KEKB in the Fuji area. The HER and LER can store maximum currents of 2.6 A and 1.1 A ,respectively. The beams are accelerated using an radio frequency (RF) of 508.9 MHz and circulated in the ring using, sextupole, quadrupole and dipole magnets. The beams collide at the interaction point (IP) in the Tsukuba region around which the Belle detector is located. The beams intersect each other at a crossing angle of 22 mrad. This provides effective beam separation at the IP, minimizes background and eliminates the need of separation magnets in the detector volume. To attain maximum luminosity, two super conducting crab cavities are employed, which kick the bunches into the horizontal plane. The transverse RF in crab cavities enables the bunches to spin and collide with maximum overlap at the IP as illustrated in Figure 2.2. The highest instantaneous luminosity attained was 2.11×10^{34} cm^{-2}s^{-1}, a world record till 2020. Total integrated luminosity collected is 1 ab^{-1}. The Lorentz boost provided by the set up is 0.425 and the production cross-section of $c\bar{c}$ is 1.3 nb.

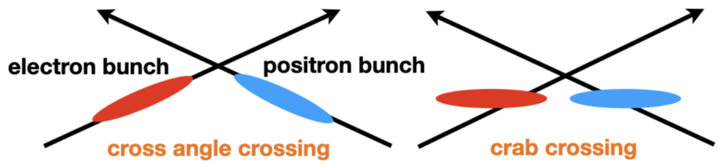

Figure 2.2: Illustration of crossing angle and crab crossings.

2.1.2 The Belle Detector

The Belle detector [30] is located around the IP of the KEKB ring. It is made up of several sub-detectors (sub-systems) which are discussed in the following sections. Figure 2.3 shows a diagram of the Belle detector.

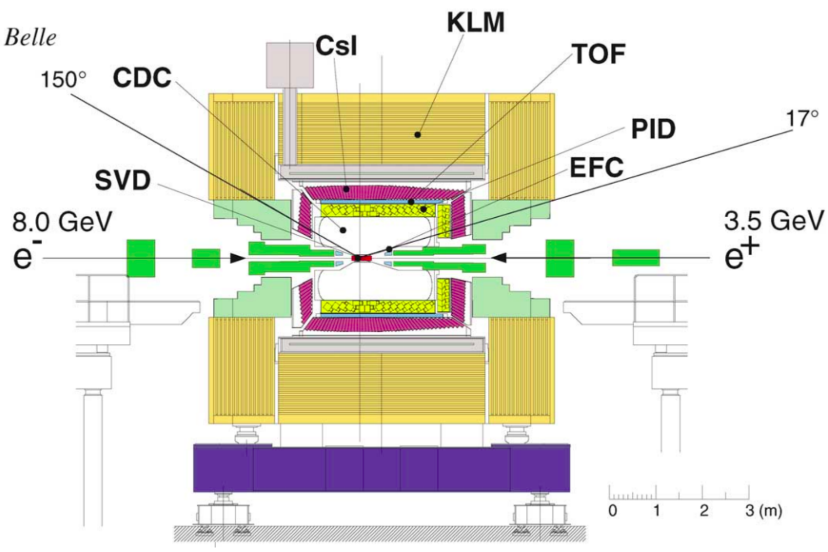

Figure 2.3: The Belle detector (side-view). [30]

The co-ordinate system followed by Belle is right handed, in which x direction is horizontally, outward from the KEKB accelerator. The y direction is vertically upward and the z direction is in the electron beam direction. As per the spherical co-ordinate system, the polar angle θ is measured relative to the positive z-axis, while the azimuthal angle ϕ is measured relative to x-axis. Due to the Lorentz boost, all sub-detectors are asymmetric along the z direction.

Extreme Forward Calorimeter

The Extreme Forward Calorimeter (EFC) enhances the sensitivity to decays like B$\rightarrow \tau\nu$. In the forward direction, the angular coverage is $6.4° < \theta < 11.5°$, while in the backward direction it is $163.3° < \theta < 171.2°$. The EFC is positioned on the front end of the cryostats from the accelerator compensation solenoid magnets, which surround the beam pipe. It reduces the background for the Central Drift Chamber (CDC) in addition to monitoring the luminosity and beam condition of the Belle detector and KEKB, respectively.

This region in which the EFC is placed has a severe radiation environment and has to be made of material that are highly radiation hard. It is made up of $Bi_4Ge_3O_{12}$ (BGO) crystals, which have a radiation hardness of the order of megarad and an energy resolution of (0.3-1)%/$\sqrt{E}$ GeV [31]. The cross-sectional area of these crystals is 2×2 cm^2, providing a 12 radiation lengths in the forward and 10 radiation lengths in the backward directions.

Silicon Vertex Detector

The Silicon Vertex Detector (SVD) is designed to precisely measure the decay vertices of the B and D mesons along the z axis. In addition, The SVD provides the tracking information for charged particles with low momentum like the pions from the $D^{*+} \to D^0$ π^+ decays. The SVD is crucial for K_S^0 reconstruction as it has a short flight length [23] and decays within the SVD. During the operational years of Belle, two types of SVD were used. SVD1, which had three layers was used till summer 2003 and collected about 20% of the total data-set. Due to the damage caused by synchrotron radiation, SVD1 was succeeded by SVD2, which was used till the end of data taking in 2010 and collected 80% of the data.

As shown in Figure 2.4, SVD1 is made up of three layers. These layers are made up ladders that are made up of Double Sided Silicon Strip Detectors (DSSDs). Each ladder resembles a narrow wooden plank, on which the sensors are mounted. The radii from the IP is 30 mm (inner), 45.5 mm (middle) and 60.5 mm(outer). The corresponding number of ladders are 8, 10 and 14. The DSSDs are mounted on ladders and supported by Boron-Nitride (BN) ribs. Each DSSD is 300 µm thick with a size of 57.5×33.5 mm^2. They have 640 readout pads with 1280 sense strips. The angular coverage of SVD is $129° < \theta < 139°$. The signals are received through readout using VA1 chips [32].

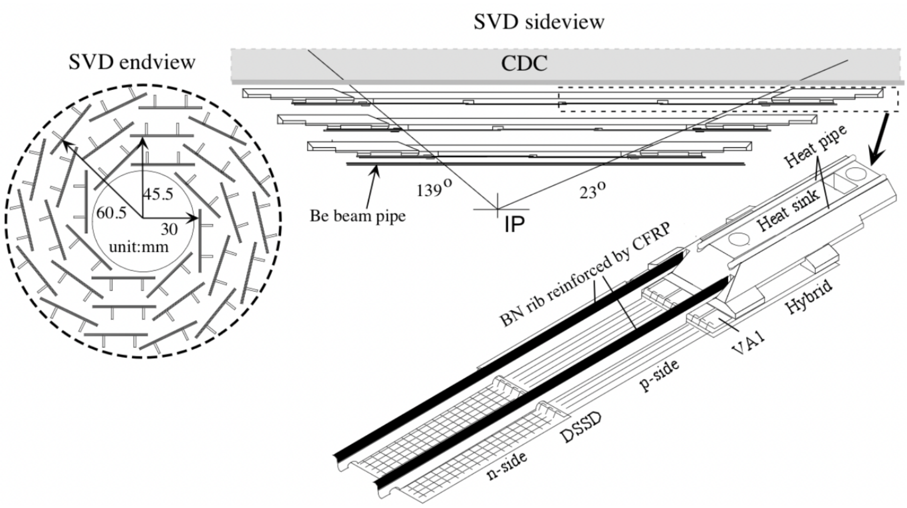

Figure 2.4: Schematic of the SVD1 sub-detector [30].

SVD2 Figure 2.5 is an upgraded version of SVD1. It has 4 layers and hence, a larger angular acceptance. The radii of the layers is 20 mm (layer 1), 43.5 mm (layer 2),70 mm (layer 3) 88 mm (layer 4). The number of ladders are 6,12, 18 and 18, respectively. In the $r - z$ and $r - \phi$ planes the DSSDs for have 512 readout channels. The VA1 readout chips from SVD1 are replaced by the VA1TA chips.

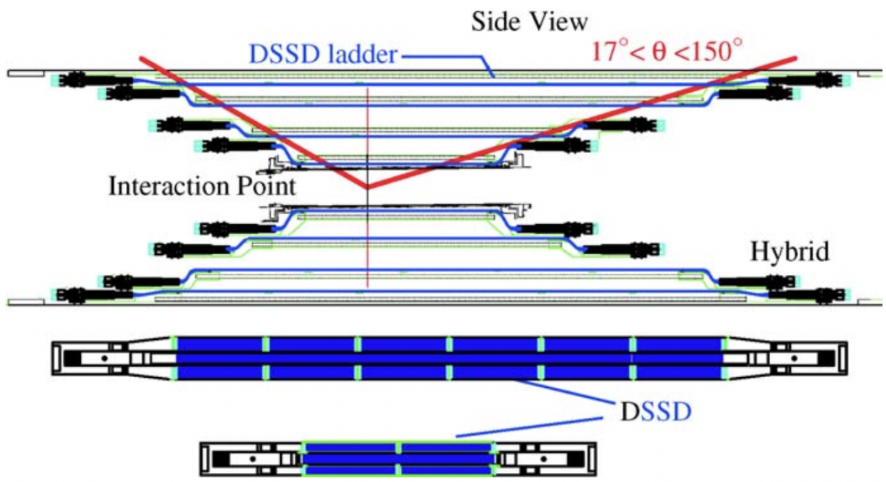

Figure 2.5: Schematic of the SVD2 sub-detector [30].

The xy impact parameter is given by $\sigma_{xy} = 19 \oplus 50(p\beta sin^{3/2}\theta)^{-1}$ µm and the z impact parameter is given by $\sigma_z = 36 \oplus 42(p\beta sin^{5/2}\theta)^{-1}$ µm . Here, $\oplus$ is the quadratic sum, p is momentum in GeV/c and β is the velocity of the particle divided by the speed of light. For a 1 GeV track, the impact parameter resolution is about 55 µm .

Central Drift Chamber

The purpose of the Central Drift Chamber (CDC) is the measurement of momenta of charged particles. The SVD and the CDC together form the tracking system of Belle. In addition, the CDC also provides particle identification (PID) for particles that do not reach beyond the CDC. For PID, CDC uses the information of mean energy loss per distance travelled (dE/dx) information as per the Bethe-Bloch formula. The magnetic field of superconducting solenoid is 1.5 T and it bends the trajectories of the charged particles according to their momenta.

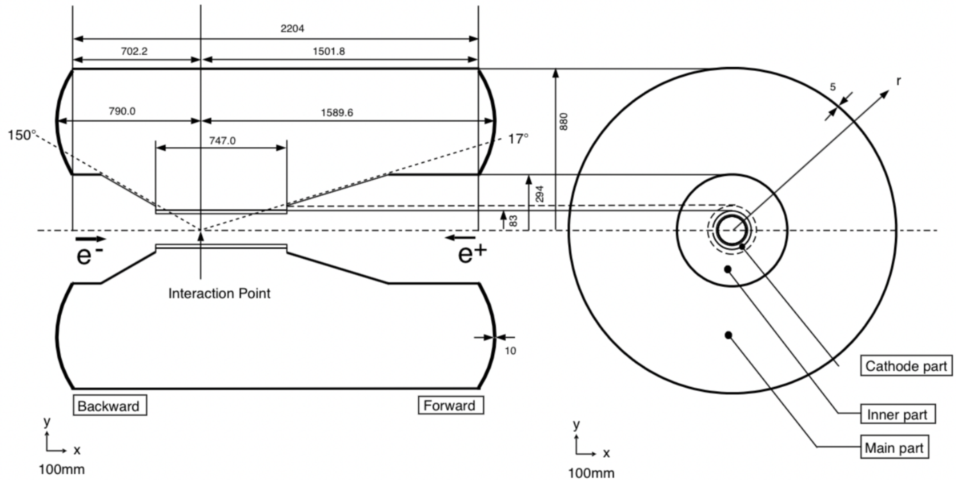

Figure 2.6: Schematic of the Belle CDC [30].

The CDC Figure 2.6 is a cylindrical, wire drift chamber is 2,400 mm in length, with respective inner and outer radii of 83 mm and 874 mm. It has a total of 50 layers (18 small angle stereo layers and 32 axial) of anode sensing wire (8,400 readout channels) and cathode strips (1792 readout channels). The axial wires are arranged parallel to z-axis, while the stereo wires are slanted at an angle of ± 50 mrad. These wires are made up of tungsten and plated with gold. The cathode strips improve the z measurement as well as produce an efficient fast z-trigger. The anode wires provide the dE/dx information for PID as shown in Figure 2.7. To mitigate the effect of multiple Coulomb scattering, the drift chamber is filled with a 50:50 mixture of Helium (He) and C_2H_6 (ethane) [33].

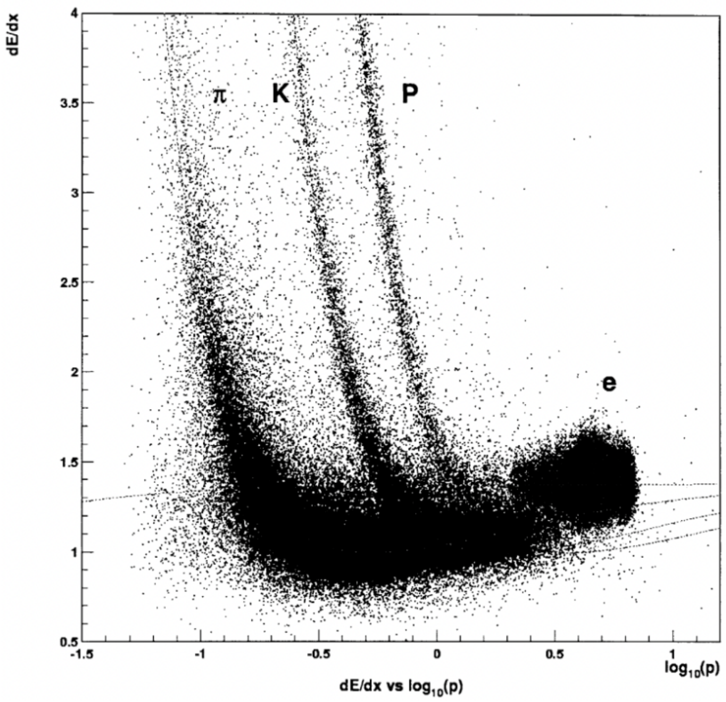

Figure 2.7: Plot for the dE/dx vs logarithm of momentum for various charged particles [30].

Aerogel Cherenkov Counter

The Aerogen Cherenkov Counter (ACC) is designed for the separation of kaon and pion tracks with the momentum ranging from 0.5 GeV/c to 4 GeV/c. The functioning of ACC depends on the detection of Cherenkov light, which is generated when a particle moves faster than the speed of light in a medium. The condition for emission for Cherenkov light is given by $\beta = p\sqrt{(p^2 + m^2)} > 1/n$. Here, m, p are ,respectively the mass and momenta of the particle, while n denotes the refractive index of the medium. Thus, for the same range of velocities for kaons that produce Cherenkov light, pions do not. This phenomena is exploited to identify the kaons and pions. Figure 2.8 shows a schematic diagram of the ACC. The ACC is made up of 960 silica aerogel counter modules divided into 60 cells in the barrel region (ϕ direction). In the forward end-cap region, 228 modules are arranged in 5 concentric circles. Blocks of aerogel with refractive index 1.010, 1.013, 1.015, 1020 and 1028 are arranged in polar region Cherenkov photons produced when particle travels through the aerogel blocks is fed to Fine Mesh Photo Multiplier Tube (FMPMT), attached to the modules. The number of readout channels is 228 in the endcap and 1560 in the barrel region.

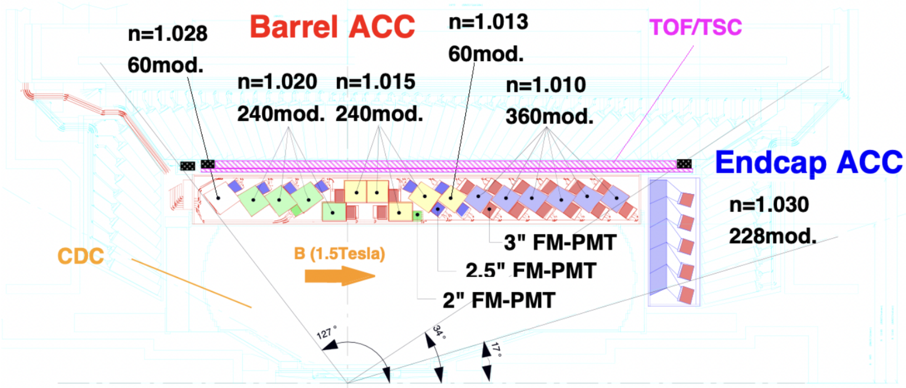

Figure 2.8: Schematic view of the ACC [30].

Time of Flight Counter

The Time of Flight (TOF) counter identifies charged particles with momenta not exceeding 1.2 GeV/c. For this momentum range, the kaon-pion identification of ACC and CDC is not as effective. The TOF also provides trigger signals with a resolution of 100 ps. The time taken by a particle to reach TOF (T) from the IP is measured. This information is combined with the momentum (p) of the particle, gives the mass (m) of the particle as per the formula

$$T = \frac{L}{c}\sqrt{1 + \left(\frac{mc}{p}\right)^2} \tag{2.1}$$

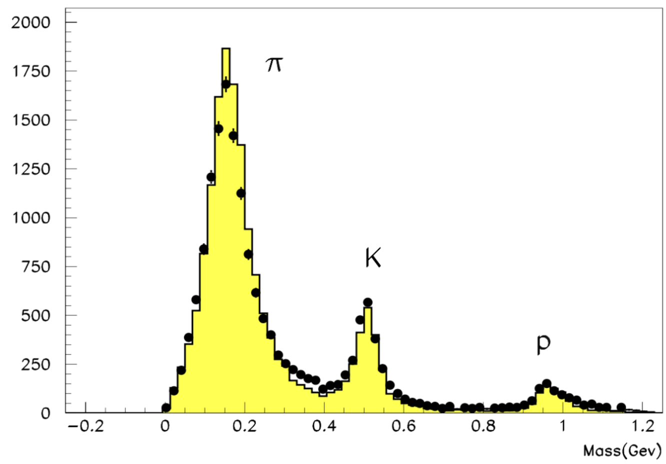

Figure 2.9: Mass distributions for various hadrons. The yellow region denotes the mass distributions obtained from simulation and the black dots represent real data points [30].

The mass distributions of various hadrons as measured by TOF measurements are shown in Figure 2.9. The TOF is made up of 128 TOF counters and 64 Trigger Scintillation Counters (TSC)s. One TOF module comprises of two trapezoidal TOF counters (read out by two FMPMTs) and one TSC counter (read out by one FMPMT) with a 1.5 cm radial separation as shown in Figure 2.10. A total of 64 modules are placed in the barrel region and polar angle coverage $33° < \theta < 121°$.

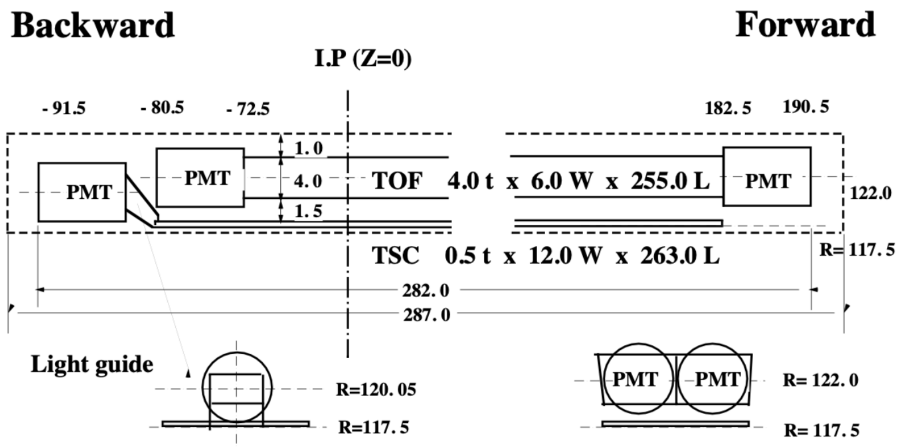

Figure 2.10: Schematic of the TOF sub-detector [30].

Electromagnetic Calorimeter

The purpose of the electromagnetic calorimeter (ECL) is to measure the energy and position of the photons coming from the decay of π^0 as well as other radiative decays. In addition, the ECL serves for electron and positron identification. The ECL is made up of an array of thallium doped Cesium Iodide (CsI(Tl))crystals. These crystals are tower shaped and placed such that they are pointed towards the IP.

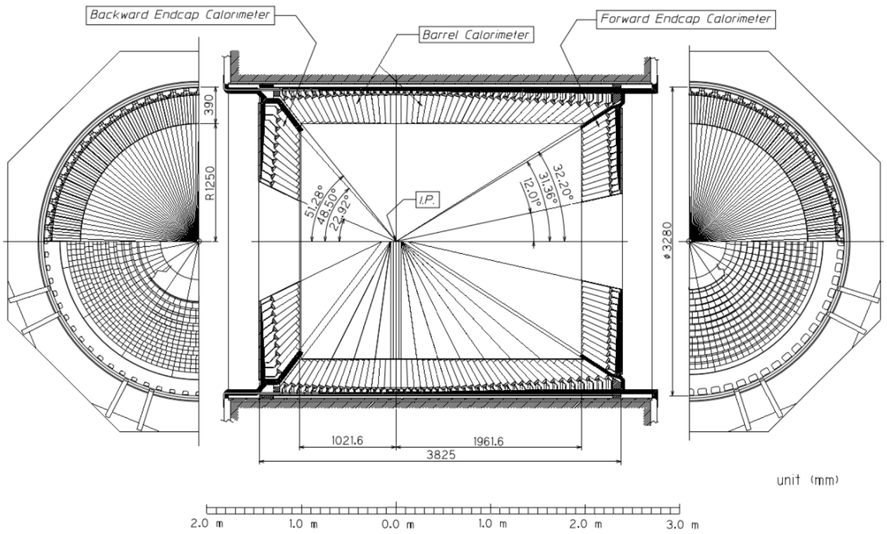

Figure 2.11: Schematic view of the Belle ECL [30].

The crystals are slanted at a small angle to prevent the photons from passing through the gaps without interaction. A schematic of the ECl is shown in Figure 2.11. The crystals are about 30 cm in length, which provide for 16.2 radiation lengths for photons and electrons. The forward end cap region covers polar angle of $12.4° < \theta < 31.4°$, with 1152 crystals. The barrel region covers $32.2° < \theta < 128.7°$ with 6624 crystals and the backward end-cap covers $130.7° < \theta < 155°$ with 960 crystals. The distances from the IP are 196 cm for the forward and the end-cap regions and 125 cm for the barrel region. The signals are read out by PIN (positive intrinsic negative) photo diodes .

K^0_L and muon detector

The K^0_L and muon (KLM) detector detects K^0_L and also to identify muons with momenta exceeding 600 MeV. This sub-detector is positioned outside the solenoid and its polar angle coverage is $20° < \theta < 155°$. It is made up of 15 layers of two glass-electrode Resistive Plate Chambers (RPC) and 14 layers of iron plates of thickness 4.7 cm sandwiched between the RPCs. At the end-cap, the KLM has 14 RPC layers. Each RPC super layer is made up of two RPC planes that give the θ and ϕ information. The internal spacer arrangement of the barrel and end-cap RPCs is shown in Figure 2.12. There also exists an active gaseous region between the two parallel plate glass electrodes. The passage of charged particles through this gas results in a local discharge and a signal in the readout strips. The signals thus produced are read out by cathode strips. The end-cap region have 16126 readout channels, while the barrel region have 1856 channels.

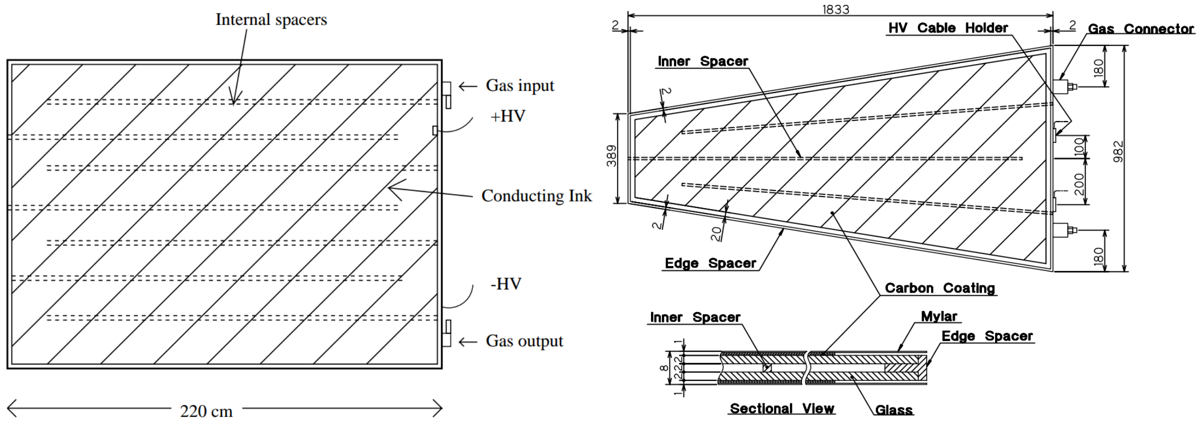

Figure 2.12: Internal spacer arrangement of the barrel (left) end-cap (right) RPC [30].

The material in the Belle detector till the KLM is equivalent to about one hadronic interaction length of K^0_L. An additional 3.9 interaction length is provided by the iron plates, which increase the detection efficiency of the K^0_L. A hadron shower pattern is produced when a K^0_L interacts with matter via the strong force. This produces a cluster of hits in the KLM, unrelated to the charged tracks. The muons interact through electromagnetic interaction and energy loss is through ionization instead of a hadronic shower. The KLM tracks that can be matched to the CDC are labelled as muons.

2.1.3 Trigger System

The trigger plays a crucial role in selecting the events of interest, whilst neglecting enormous beam backgrounds that arise due to the interaction among beam particles, interaction of beam particles with residual gas, etc. An overview of the complete trigger system for Belle is shown in Figure 2.13. The trigger starts with the level 1 (L1) trigger, followed by the level 3 (L3) software trigger, which is based on an online computer farm. At the final stage is a level 4 (L4) trigger operating on the offline computing system of Belle.

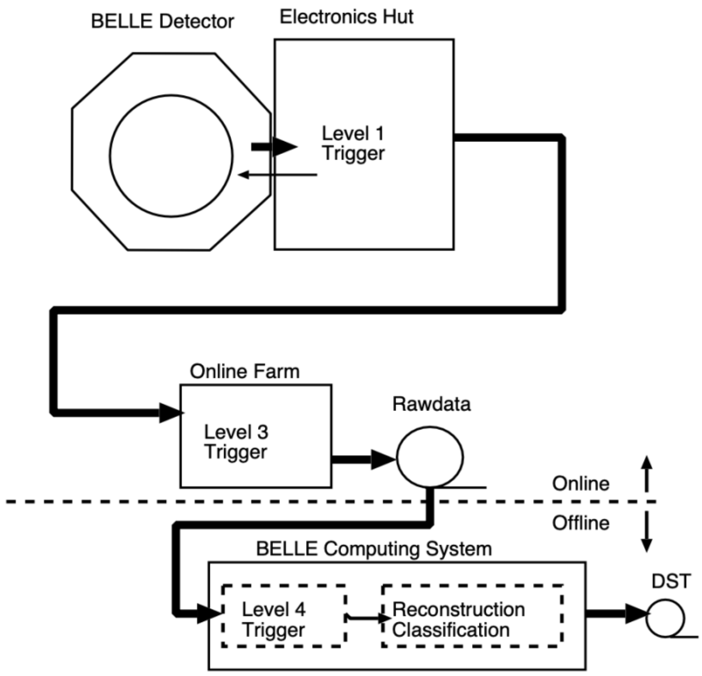

Figure 2.13: Overview of the Belle trigger system [34].

The L1 trigger comprises of the sub-trigger system and the central trigger system, which is called the Global Decision Logic (GDL). The track information is provided to L1 by the CDC, ACC and TOF, while the energy trigger is provided by the ECL. The information received is processed in parallel and sent to the GDL within 1.8 μs and the L1 trigger decision is issued after 2.2 μs. Usually, the TOF determines the timing of the final trigger but in its absence, it is determined by the ECL. A flowchart of the L1 trigger is shown in Figure 2.14. The timing is synchronized with the RF signal of KEKB.

The L3 trigger carries out a quick reconstruction and selects events with at least one track with longitudinal (z) impact parameter not exceeding 5 cm and energy deposit of 3 GeV in the ECL. The events are thus reduced by about 60%, whilst retaining 99% of relevant physics events. At the final stage, the L4 trigger removes events that originate away from the IP and filters out 78% of previously triggered events. However, these events are still stored as raw data. Thus, L1 and L3 together reduce the data size and L4 reduces the CPU time for the production of Data Summary Tapes (DST)s.

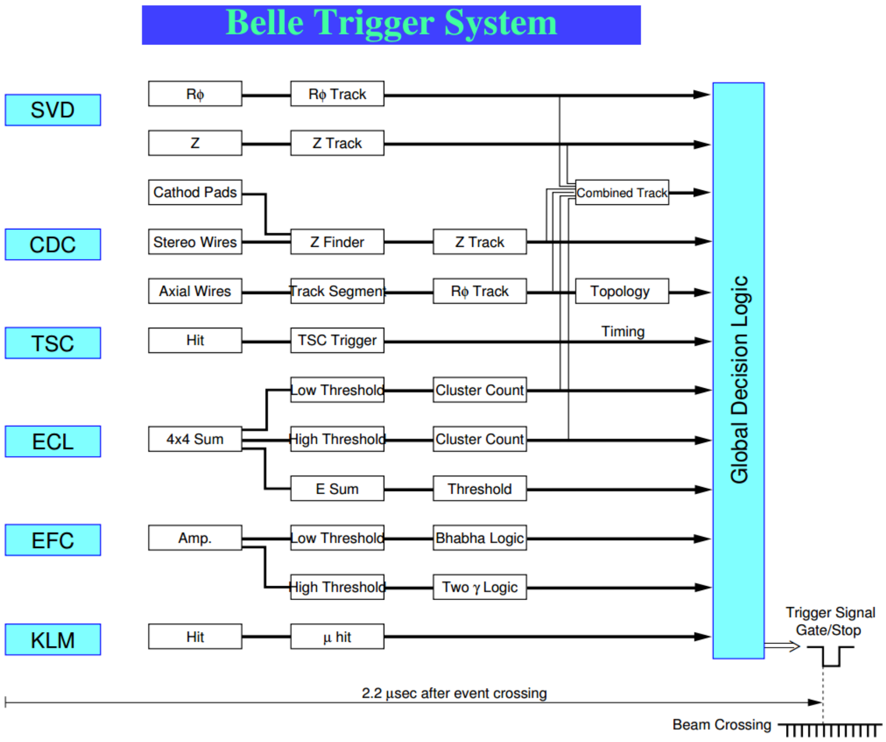

Figure 2.14: Level 1 trigger system of Belle [30].

2.1.4 Data Acquisition System

The Data Acquisition (DAQ) system is designed to record events selected by the trigger up to 500 Hz, whilst the dead time fraction of less than 10% is maintained. Figure 2.15 shows an overview of the Belle DAQ system.

The DAQ system is divided into seven sub-systems corresponding sub-detectors of Belle. The signals received from the sub-detectors pass through a charge-to-time (Q-to-T) converter. These signals are then processed by the time-to-digital (TDC). The SVD employs Flash Analouge to Digital Converters (FADC)s instead of TDCs. A common stop signal is sent by the Sequence (SEQ) controller to the TDCs to begin the readout. The data thus collected is transferred to the event builder through Versa Module Eurocard (VME) crates. The SVD readout system comprises of four VME crates. The data is then sent to the online computer farms via the L3 trigger. At this stage, Data Quality Monitoring (DQM) is done in real time and finally sent to the KEK Computing Center. At 500 Hz trigger rate, maximum rate of data transfer is 15 MB/s.

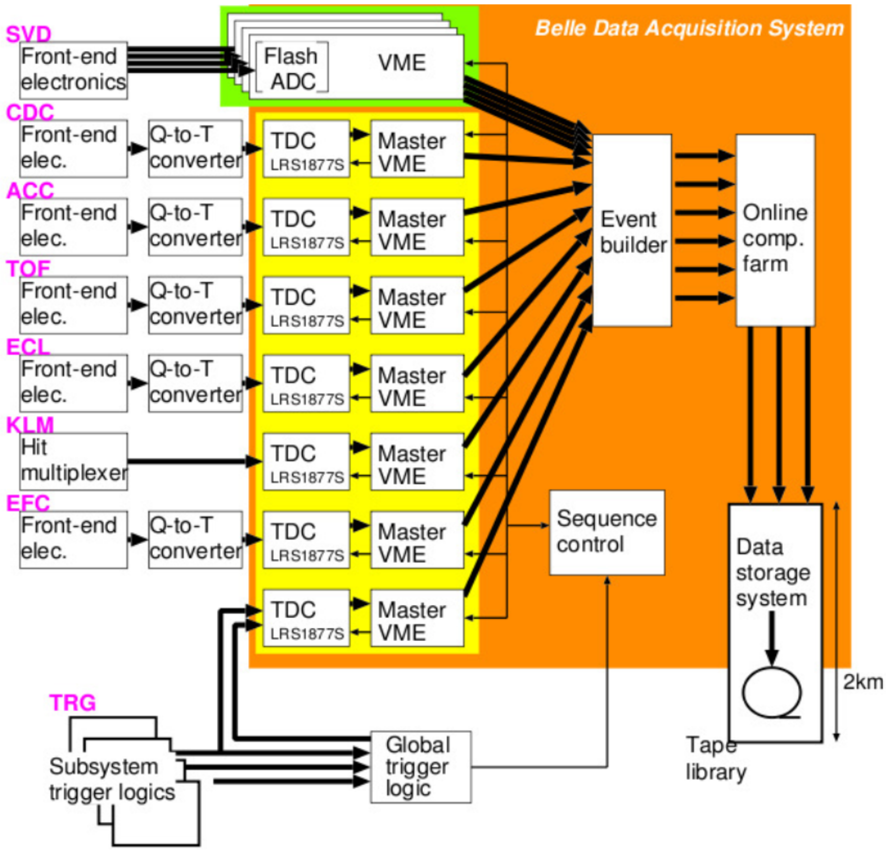

Figure 2.15: Overview if the Belle DAQ system [30].

2.2 The Belle II Experiment

2.2.1 SuperKEKB Accelerator

The SuperKEKB [35] is the successor of the KEKB collider. It is also an asymmetric e^+-e^- collider. The e^- beam has an energy of 7 GeV and e^+ beam has an energy of 4 GeV. These beams collide at center of mass energy ($\sqrt{s}$) equivalent to the mass of $\Upsilon(4S)$ resonance (10.58 GeV) producing large samples of b, c and τ pairs. SuperKEKB aims to achieve an instantaneous luminosity of 6.5×10^{35} cm^{-2}s^{-1}, which is 30 times higher than that of Belle. It has already achieved an instantaneous luminosity of 4.7×10^{34} cm^{-2}s^{-1} and holds the current world record [36].

The production mechanism of the collision is the same as that of KEKB. The instantaneous luminosity (L) of a detector is given by

$$L = \frac{\gamma_\pm}{2er_e}\left(1+\frac{\sigma_y^*}{\sigma_x^*}\right)\left(\frac{I_\pm\xi_{y\pm}}{\beta_{y\pm}}\right)\left(\frac{R_L}{R_{\xi_y}}\right) \tag{2.2}$$

The positron is denoted by the suffix + and the electron is denoted by −. The parameter γ denotes the Lorentz factor, while e and r_e denote the electric charge of the electron and the classical radius of the electron, respectively. σ_x^* and σ_y^* denote the widths of the

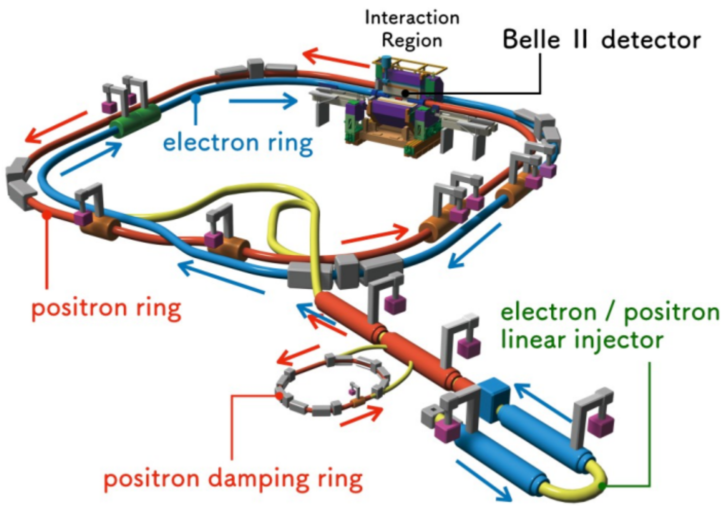

Figure 2.16: Configuration of the SuperKEB accelerator system [35].

bunch (beam size) at IP on the transverse plane, I is the beam current and β_y^* denotes the vertical beta function at the IP. The vertical beam-beam parameter is given by ξ_y. R_L denotes the reduction factors of luminosity and R_{ξ_y} denotes the vertical beam-beam parameter.

To achieve the design luminosity, the machine parameters of SuperKEKB are chosen, so as to realize the "nano-beam scheme" [37]. The beam overlap at IP is minimized, thereby limiting the vertical β function at IP. An illustration of the nano beam scheme is shown in Figure 2.17, where d is the effective bunch length, determined by half of the crossing angle ϕ and (σ_x^*) as:

$$d \approx \frac{\sigma_x^*}{\phi} \tag{2.3}$$

To shorten d a large crossing angle is needed as compared to small horizontal emittance and horizontal β function at IP. Beam crossing angle at Belle II is 83 mrad, about four

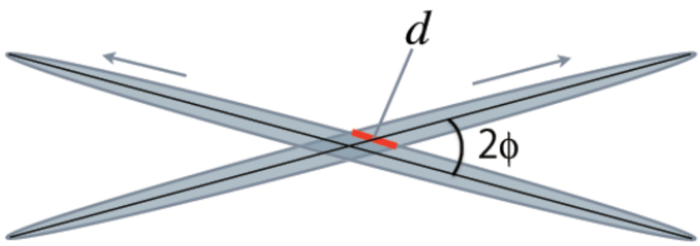

Figure 2.17: Illustration of beam collision in nano beam scheme. Here, d is the effective overlap and 2ϕ is the beam crossing angle.

times that of the KEKB. In addition σ_x^* is reduced to have a beam size of 50 nm. To obtain the required instantaneous luminosity, the beta function is reduced by a factor of 20 and the beam current is increased by two times, as compared to KEKB.

2.2.2 Belle II Detector

The Belle II detector is the upgraded version of the Belle detector. It is located around the interaction point of SuperKEKB. A sketch of the Belle II detector is shown in Figure 2.18. A brief overview of all the sub-detectors of Belle II and its trigger system are discussed in the following sub-sections.

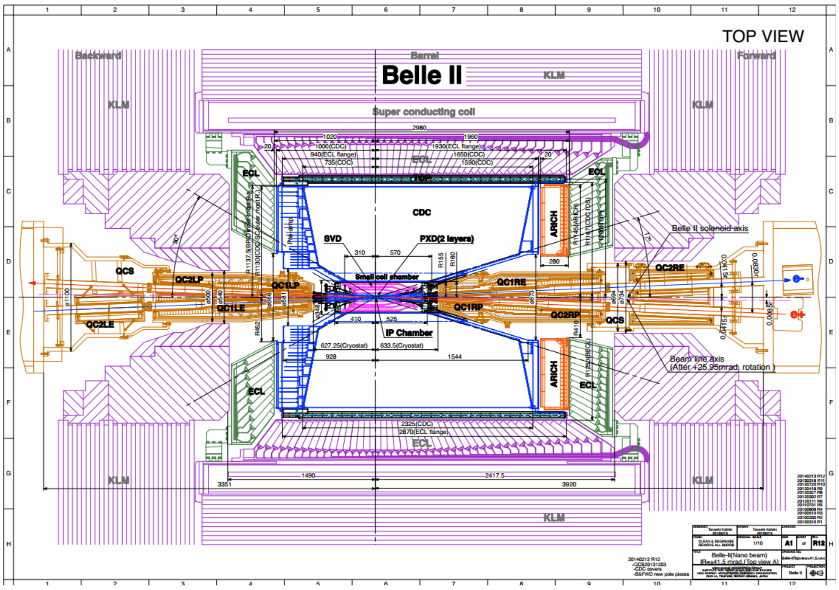

Figure 2.18: The Belle II detector (top view) [38].

Vertex Detector (VXD)

The innermost sub-detector of Belle II is the VXD. It is made up of two layers of pixel detector (PXD) and four layers of Silicon Vertex Detector (PXD). The structure of VXD can be seen in Figure 2.19 .

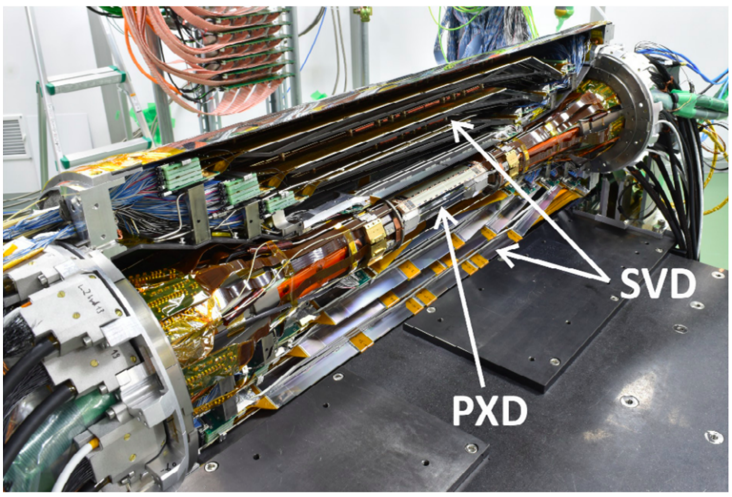

Figure 2.19: Belle II VXD showing one half of the SVD, attached to the beam pipe. The PXD is at the center [39].

Pixel Detector

SuperKEKB operates at extremely high luminosities due to, which the VXD faces very high occupancy. To cope up with such extreme conditions and to simultaneously provide precise vertexing, pixel sensors, with depleted field effect transistor technology (DEPFET) are used. Pixel sensors are advantageous because they have a large number of channels and DEPFET technology allows them to be ultra thin (50 microns) [40]. Readout electronics are placed beyond the acceptance region. The PXD has two layers with respective radii 14 mm and 22 mm from the IP. The pixel size for the inner and outer layers are ($50 \times 50\ \mu\text{m}^2$) and ($50 \times 75\ \mu\text{m}^2$) ,respectively. It covers the complete polar acceptance of the PXD ($17^\circ < \theta < 150^\circ$). The inner layer has 8 planer sensors (ladders), each 15 mm wide, with sensitive length of 90 mm. The outer layer has 12 ladders, 15 mm in width, with 123 mm of sensitive length. The read out time is 20 μs.

Silicon Vertex Detector

The SVD is made up of 4 layers of DSSDs, with radii from the IP 39 mm (layer 3), 80 mm (layer 4), 104 mm (layer 5) and 135 mm (layer 6). The n and p strips of the DSSDs are, respectively positioned perpendicular and parallel to the beam direction. Such an arrangement gives both, the x and y co-ordinates of the hits, respectively. The innermost layer of the SVD (layer 3) is made up of seven ladders. Each ladder has two small rectangular sensors of thickness 320 µm. Layer 4 has ten ladders, each of which is made up of three sensors in total. Two of these sensors are large rectangular (thickness of 320 µm) and the one in the forward region is trapezoidal (slanted, thickness of 300 µm). Layer 5 comprises of twelve ladders, each of which is made up of 4 sensors (two large rectangular sensors and the one slanted sensor in the forward region). The outer most layer has three large rectangular sensors and one trapezoidal sensor. The slanted sensors improve the acceptance and precision of boosted particles. For the readout electronics of SVD APV25 chips [41] are used. The novel origami chip-on-sensor concept was introduced in Belle II for the inner sensors [42]. It helps to minimize the distance between the DSSD and the readout electronics. This feature reduces the capacitive noise, thereby optimizing the Signal-to-Noise ratio (SNR). The origami is a flexible three-layer fanout circuit (FlexPA) made up of polyamide. SVD provides standalone tracking (and PID) for particles with low momentum and assures the finding of the correct pixels to attach to the corresponding track, facilitating PXD data reduction.

Central Drift Chamber

The central drift chamber (CDC) is the primary tracker for the Belle II detector. It has three main tasks, the first task is the reconstruction of charged tracks and precise measurement of their corresponding momenta. Secondly, it provides particle identification for particles that do not reach beyond the CDC, using the information of energy loss within the gas volume. In addition, it also provides 3D trigger information, which is crucial to suppress background, whilst retaining relevant physics events. The CDC is a cylindrical gas drift chamber, that has a large volume. It is filled with a 50:50 mixture of Helium (He) and Ethane (C_2H_6). It has 56 layers, grouped into 9 super-layers, each with 6 layers. The radii of the inner and outer cylinder is 160 mm and 1130 mm. To accommodate the new VXD, it is made larger than the Belle CDC. The radial cell size for the innermost super-layer is 10 mm and that for the others, it is 18.6 mm. A total of 14336 (160-380 wires per layer) sensing wires of 15 µm radius are inserted into the gas volume. These wires are made up of tungsten and plated with gold. In addition, 42240 aluminium wires of thickness 126 µm , are also included to provide the field gradient. The measured spatial resolution is 100 µm .

Particle Identification

The particle identification (PID) system of the Belle II detector comprises of the Time of Propagation (TOP) counter in the barrel region and the Aerogel Ring Imaging Cerenkov (ARICH) counter in the end cap.

Time of Propagation counter

The TOP measures the Time of Propagation of the Cerenkov photons that are internally reflected inside a quartz radiator as shown in Figure 2.20. The Cerenkov image is then reconstructed using the x and y coordinates and precise timing information, which is provided by the micro-channel plates (MCP) and photo multiplier tubes (PMT) at the end surfaces of the quartz bar. This information allows the measurement of the Cerenkov angle θ_c, from which one can estimate the particle velocity and mass hypothesis. The

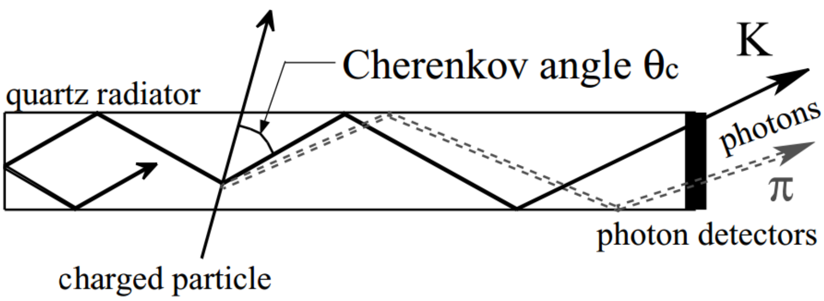

Figure 2.20: Conceptual overview of TOP counter. [38].

TOP encircles the exterior wall of the CDC. It has 16 modules, that are made of quartz radiators each about two metres in length. A mirror is placed at the front end to reflect photons. The reflected photons (moving backwards) are then captured by the PMT channels. Chromaticity of Cherenkov photons limits the PID performance due to broadening of the time resolution. To mitigate this effect, a focusing mirror is positioned at the end of the quartz radiator. The Cherenkov photons with different θ_c are focused on different PMT channels, thereby reconstructing a partial ring image, using the$x$, y and t co-ordinates. The angular acceptance of the TOP counter is $31° < \theta < 128°$.

Aerogel Ring Imaging Cerenkov counter

The working principle of ARICH is highlighted in Figure 2.21. The ARICH is made up of

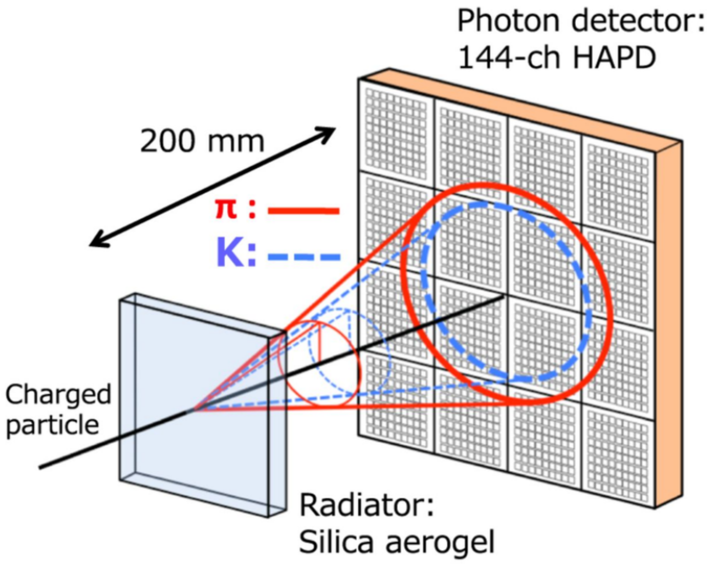

Figure 2.21: Pion and kaon identification for the ARICH counter. [43].

silica aerogel radiators. When a charged particle passes through the radiator, Cherenkov photons are produced. These photons then pass through the 20 cm expansion space to the hybrid avalanche photon detector (HAPD) surface, allowing the photons to expand into rings. Arrays of position sensitive photon detectors are used, which can efficiently detect single photons in a high magnetic field (1.5 T). The performance metrics of ARICH are the number of photons detected (N_γ) and single photon resolution of the Cerenkov angle (σ_{θ_c}). Longer radiators give larger N_γ, but the photon resolution degrades due to emission point uncertainty. To suppress this effect, a non homogeneous radiator is used. Two radiator layers with refractive indices (n =1.065,1.055) and 2 cm thickness are used. The indices are chosen to make the rings overlap on the detecting surface. the optimal value of σ_{θ_c} is about 3 mrad for charged tracks with velocity exceeding 3.5 GeV/c. The polar angular coverage is $14° < \theta < 30°$.

Electromagnetic Calorimeter

The electromagnetic calorimeter (ECL) detects photons over the range of 20 MeV to 4 GeV. It also provides electron identification and helps with K_L^0 detection along with the KLM. In addition, it measures the online and offline luminosity of SuperKEKB. the scintillating material is thallium doped Caesium Iodide CsI(Tl) crystals, that are inherited from Belle ECL. It has 6624 crystals each shaped like a truncated pyramid of size of length

30 cm and cross section 6×6 cm^2 . The end-caps have of 2112 CsI crystals of 69 shapes. Due to much larger backgrounds at Belle II, the readout electronics has been completely upgraded to reduce pile-up background [44]. The calorimeter provides polar angular coverage of $12.4° < \theta < 155.1°$.

$K^0_{\rm L}$ and muon detector

The $K^0_{\rm L}$ and muon detector (KLM) is made up of an alternating sandwich of 4.7 cm thick iron plates. These iron plates provide 3.9 interaction length of material in addition to 0.8 interaction length of the calorimeter in which the $K^0_{\rm L}$ showers hadronically. Hadron showers produced due to the interaction of $K^0_{\rm L}$ with the ECL or iron plates are detected in the ECL, KLM or in both. The Belle KLM used glass electrode based RPCs. The RPCs have a longer dead-time and now, due to higher hit rate, the probability of muon misidentification increases. Therefore in Belle II KLM, scintillator strips with Silicon Photo Multipliers (SiPM) are used.

2.2.3 Trigger and Data Acquisition system

The trigger system of Belle II trigger consists of two levels: low level trigger (L1), which is hardware based and High level trigger (HLT), which is software based. All components of the Belle trigger sub-system are replaced. A flow chart of the Belle II trigger is shown in Figure 2.22. The trigger collects the information from multiple sub-triggers and provides it to the final decision logic. The CDC sub-trigger provides the charged track information. The ECL sub-trigger provides the information of energy deposit, energy cluster, Bhabha and also, cosmic-rays. The Barrel PID (BPID) sub-trigger provides hit topology information, while the Endcap PID (EPID) sub-trigger is gives precise timing information. Muon track information is provided by the KLM sub-trigger. The information thus collected is funneled to the GDL, which finally gives the Level 1 trigger decision. The event rate of L1 is 30 kHz. The HLT reduces the event rate to 10kHz, the maximum store-able rate of 10 kHz for offline storage and it is a crucial component of the Data Acquisition (DAQ) system.

The goal of the DAQ system is to readout signals after the L1 trigger decision and transfer them to the storage systems. The complete DAQ system is comprised of the sub-triggers for trigger and timing distributions, Belle2Link, which is a unified data link, COmmon Pipeline Platform for Electronics Readout (COPPER) system, the event Builder system and the HLT. The overview of the DAQ system is shown in Figure 2.23. The first step is the front-end boards, that are placed inside the sub-systems for CDC, BPID and EPID, while for the other sub detectors, they are placed just outside. The digitized signals obtained from them are transferred to the COPPERs using Belle2Link. Data reduction and event building is performed on the receiver modules or the on-board CPUs for COPPERs and also on the readout PCs. The data is then processed on the

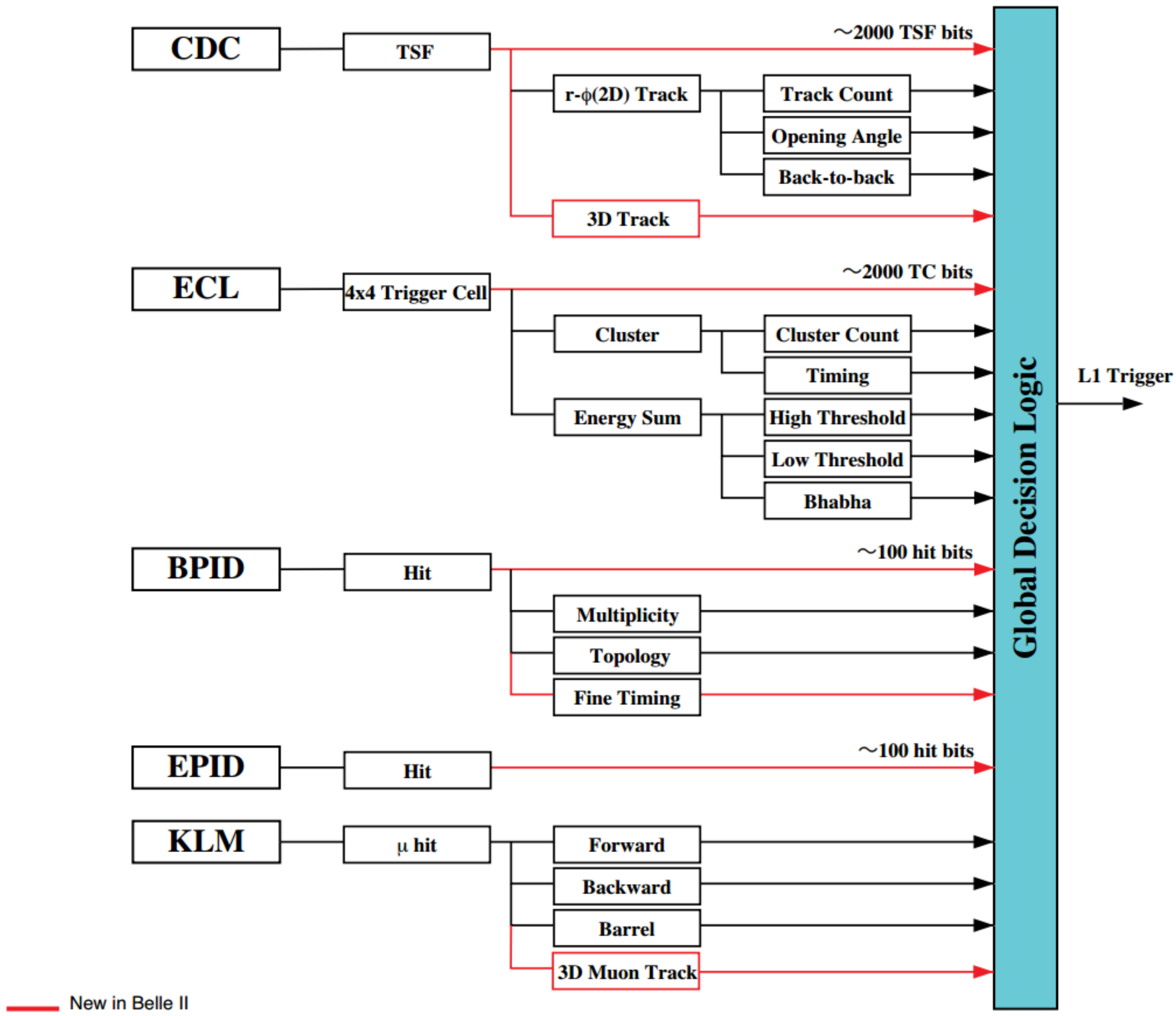

Figure 2.22: Flowchart of the Belle II trigger system. The red lines are newly added information paths [38].

HLT farms for software event selection.

It is to be noted that the PXD is not unified with the trigger system, although it produces 10 times larger event fragment than the other sub-detectors. As the readout time of the PXD about, 20 µs, it is quite probable that the next trigger is received before the completion of a single readout cycle.

The performance metrics of Belle and Belle II are compared in Table 2.1

SuperKEKB and Belle II has been non-operational since July 2022. This period referred to as Long-Shutdown 1 (LS1). The experiment is all set to resume operation s in full swing from early 2024.

The following chapter gives a synopsis of the analysis procedure that is followed to analyse the data collected by these two detectors.

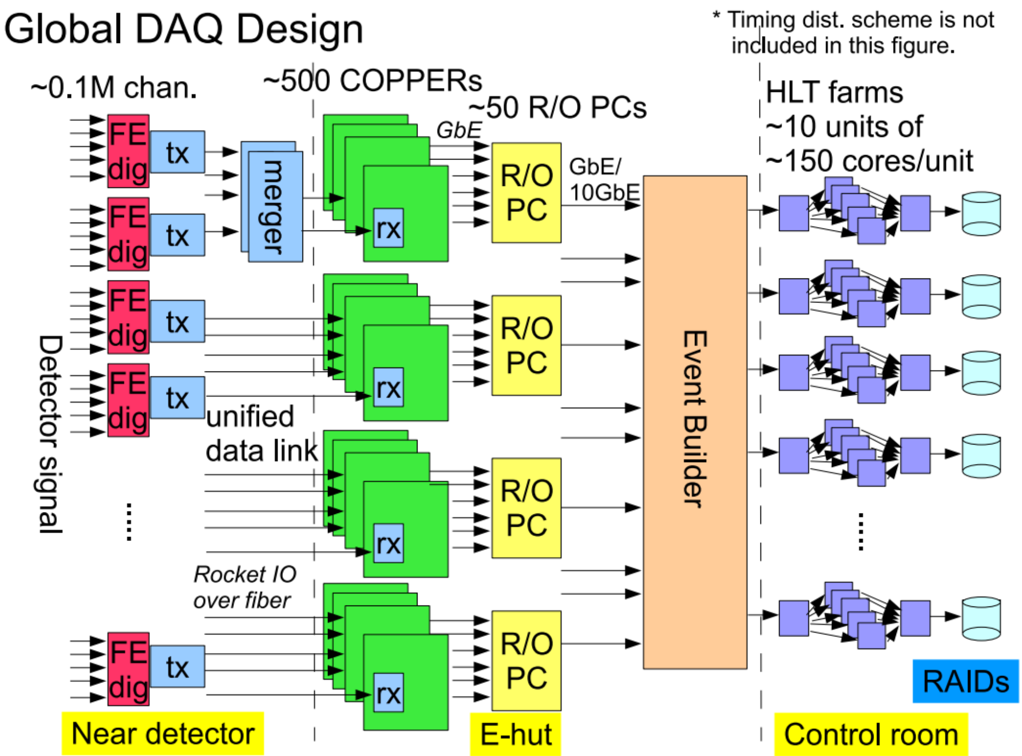

Figure 2.23: Conceptual overview of Belle II DAQ system [38].

Measurement	Belle	Belle II
Reconstruction of B Vertex	$\sigma_z = 61$ µm	$\sigma_z = 26$ µm
Tracking	$\sigma_{p_t}/p_t = 0.0019\ p_t$ [GeV/c]$\oplus$ 0.0030/β	$\sigma_{p_t}/p_t = 0.0011\ p_t$ [GeV/c]$\oplus$ 0.0025/β
Kπ ID	Kaon efficiency (ϵ_K) $\approx$ 0.85 with pion fake rate (ϵ_π) $\approx$ 0.010 for p= 2 GeV/c	$\epsilon_K \approx$ 0.90 with $\epsilon_\pi \approx$ 0.040 for p=2 GeV/c
Muon ID	Muon efficiency (ϵ_μ) $\approx$ 0.90 with fake rate of muon (ϵ) $\approx$ 0.020 for p= 0.8 GeV/c tracks	$\epsilon_\mu \approx$ 0.92-0.98 with, ϵ = 0.02-0.06 for p $>$ 1 GeV/c
L1 trigger	500 Hz typical average Efficiency for hadronic events $\epsilon_{hadron}\approx$1	30 kHz max. average rate $\epsilon_{hadron}\approx$1
DAQ	$\approx$ 5% dead time at 500 Hz L1 rate	$<$ 3% dead time at 30 kHz L1 rate

Table 2.1: Comparison of the performance metrics of Belle with Belle II [45].

Chapter 3

Physics analysis for measurement of $\mathcal{A}_{CP}$ in $D^0 \to K^0_S K^0_S$

The objective of the thesis is to determine the time integrated CP asymmetry in $D^0 \to K^0_S K^0_S$ decays using Belle and Belle II data. In this chapter, the analysis procedure that is followed to fulfill the objective, is described in detail.

3.1 Data samples and software

We use the full data sample collected by Belle, corresponding to $980\,\mathrm{fb}^{-1}$, and the full data sample collected by Belle II before LS1, corresponding to $420\,\mathrm{fb}^{-1}$. The Belle data is converted to the Belle II data format using the `B2BII` framework [46]. In Belle II, the data from experiments 7-18 (collected in 2019-2021) is processed using `proc13`; the data from experiments 20-26 are from the prompt processing of `bucket26-36`.

Monte Carlo (MC) simulated events of e^+e^- collisions at the $\Upsilon(4S)$ resonance are used in the analysis to study sample composition, determine signal and background distributions and validate the analysis procedure. For Belle, six different streams of simulated events, each corresponding to an integrated luminosity of $420\,\mathrm{fb}^{-1}$ are available. The Belle simulation used an outdated version of the decay table in which, in particular, the $D^0 \to K^0_S K^0_S$ branching fraction is set to a much larger value (4×10^{-4}) than currently measured (1.41×10^{-4}). To correct for this effect and obtain more realistic distributions we randomly reject 64.75% of the truth-matched signal decays, while processing the Belle simulation. The Belle II sample corresponds to `MC15ri` and to an integrated luminosity of $1\,\mathrm{ab}^{-1}$. In addition to this, we have also divided the Belle II MC sample in to subsets of integrated luminosity $400\,\mathrm{fb}^{-1}$, which is comparable to the luminosity of Belle II data. These subsets have been used to compare the results between data and MC for Belle II. The Belle II decay table is up-to-date with the current knowledge of the charm hadron decays. Unless specified, data and simulation samples are processed in the same way.

The `basf2` software version used is `light-2303-iriomote` [47, 48].

3.2 Methodology

The decay $D^0 \to K^0_S K^0_S$ is a singly Cabibbo-suppressed transition that involves interference between $c\overline{u} \to s\overline{s}$ and $c\overline{u} \to d\overline{d}$ amplitudes, mediated by the exchange of a W boson at tree level as shown in Figure 3.1. Such interference can generate *CP* asymmetries at

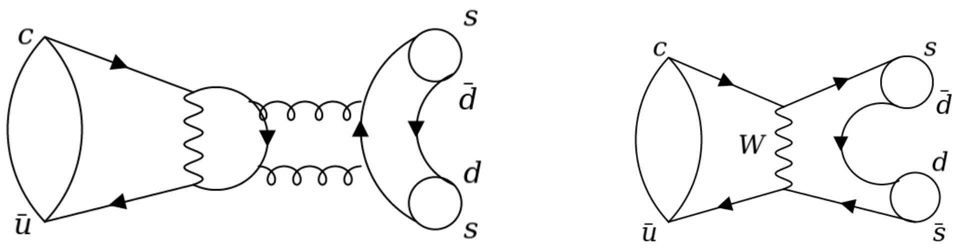

Figure 3.1: Loop level (left) and tree level (right) Feynman diagrams for $D^0 \longrightarrow K^0_S K^0_S$ decay.

the 1% level, even if the Cabibbo-Kobayashi-Maskawa phase is the only source of *CP* violation. Moreover, the *CP* asymmetry is non-vanishing only when $SU(3)_F$ is broken. Both of these features make the $D^0 \to K^0_S K^0_S$ mode quite important to understand the origin of *CP* violation in charm decays [27, 49].

The world-average determination of $\mathcal{A}_{CP}(D^0 \to K^0_S K^0_S)$, $(-1.9 \pm 1.0)\%$, is limited by the statistical precision [50]. The average is dominated by measurements from Belle [51] and LHCb [52]. Using e^+e^- collision data corresponding to an integrated luminosity of $921\,\text{fb}^{-1}$, Belle measured $\mathcal{A}_{CP}(D^0 \to K^0_S K^0_S) = (-0.02 \pm 1.53 \pm 0.02 \pm 0.17)\%$, where the first uncertainty is statistical, the second systematic, and the third is due to the uncertainty in the *CP* asymmetry of the reference $D^0 \to K^0_S \pi^0$ mode. A more precise result is obtained by LHCb measurement using *pp*-collision data collected during Run 2 and corresponding to an integrated luminosity of $6\,\text{fb}^{-1}$: $(-3.1 \pm 1.2 \pm 0.4 \pm 0.2)\%$, where the first uncertainty is statistical, the second is systematic, and the third is due to the uncertainty in the *CP* asymmetry of the reference $D^0 \to K^+K^-$ channel. The measurement of $\mathcal{A}_{CP}(D^0 \to K^+K^-)$ has been recently improved by LHCb [25], bringing the corresponding uncertainty below the 0.1% level.

In this thesis the measurement of $\mathcal{A}_{CP}(D^0 \to K^0_S K^0_S)$ with the combined Belle + Belle II data set is presented. To determine the production flavor of the neutral D meson, we reconstruct $D^0 \to K^0_S K^0_S$ decays coming from $D^{*+} \to D^0\pi^+$ decays in $e^+e^- \to c\overline{c}$ events. The decay-time-integrated *CP* asymmetry, defined as

$$\mathcal{A}_{CP}(D^0 \to K^0_S K^0_S) = \frac{\Gamma(D^0 \to K^0_S K^0_S) - \Gamma(\overline{D}^0 \to K^0_S K^0_S)}{\Gamma(D^0 \to K^0_S K^0_S) + \Gamma(\overline{D}^0 \to K^0_S K^0_S)} \tag{3.1}$$

with Γ being the partial decay width, is measured from the *raw* asymmetry in reconstructured yields,

$$A_{\mathrm{raw}}^{K_S^0 K_S^0} = \frac{N(D^0 \to K_S^0 K_S^0) - N(\overline{D}^0 \to K_S^0 K_S^0)}{N(D^0 \to K_S^0 K_S^0) + N(\overline{D}^0 \to K_S^0 K_S^0)} \tag{3.2}$$

after correcting for nuisance asymmetries (forward-backward asymmetry, detection asymmetry of π_s) induced by production and detection mechanisms. The nuisance asymmetries are determined using the control channel $D^{*+} \to D^0(\to K^+K^-)\pi^+$. In the limit of small *CP* and nuisance asymmetries, the raw asymmetry of a D^{*+}-tagged D^0 decay to a two-body and *CP*-symmetric final state f can be expressed as

$$A_{\mathrm{raw}}^{f} = \mathcal{A}_{CP}(D^0 \to f) + A_{\mathrm{FB}}^{D^{*+}}(D^0 \to f) + A_{\epsilon}^{\pi_s}(D^0 \to f) \tag{3.3}$$

where A_{FB} is the forward-backward asymmetry in the D^{*+} production and $A_{\epsilon}^{\pi_s}$ is the detection asymmetry of the low-momentum tagging pion (*soft*, π_s) from the D^{*+} decay. The forward-backward asymmetry arises from γ^*-Z^0 interference and higher order QED effects in $e^+e^- \to c\bar{c}$ events. Assuming that the nuisance asymmetries are identical between $D^0 \to K_S^0 K_S^0$ and $D^0 \to K^+K^-$ decays, or that they can be made so by weighting the control sample, the *CP* asymmetry in $D^0 \to K_S^0 K_S^0$ decays can be determined as

$$\mathcal{A}_{CP}(D^0 \to K_S^0 K_S^0) = A_{\mathrm{raw}}^{K_S^0 K_S^0} - A_{\mathrm{raw}}^{K^+K^-} + \mathcal{A}_{CP}(D^0 \to K^+K^-)\,, \tag{3.4}$$

where $\mathcal{A}_{CP}(D^0 \to K^+K^-)$ is an external input. In particular, we use $\mathcal{A}_{CP}(D^0 \to K^+K^-)$ computed from the results reported in Refs. [25, 53] and [54]

$$\mathcal{A}_{CP}(D^0 \to K^+K^-) = \mathcal{A}_{CP}^{\mathrm{dir}}(D^0 \to K^+K^-) + \Delta Y = (6.7 \pm 5.4) \times 10^{-4}\,, \tag{3.5}$$

where $\mathcal{A}_{CP}^{\mathrm{dir}}$ is the direct *CP* asymmetry and ΔY ($\approx -A_\Gamma$) is the asymmetry arising from *CP* violation in mixing and in the interference between mixing and decay [25]. The value of ΔY is here assumed to be independent of the D^0 decay. The measurements of $\mathcal{A}_{CP}^{\mathrm{dir}}(D^0 \to K^+K^-)$ from Ref. [25], $(7.7 \pm 5.7) \times 10^{-4}$, and ΔY from Ref. [53], $(-1.0 \pm 1.1) \times 10^{-4}$, have a total correlation of 35%.

The chapter is further organized as follows: the analysis of the signal mode $D^0 \to K_S^0 K_S^0$ decays is presented in Section 3.3, and that of the control mode $D^0 \to K^+K^-$ is described in Section 3.4.

3.3 Determination of $A_{\rm raw}$ in $D^0 \to K_S^0 K_S^0$ decays

3.3.1 Event selection

In Belle, events with signal decays are first filtered by the `HadronB(J)` skim [55,56]. The selection of the `HadronB` skim is detailed in Ref. [55] and aims at enriching the sample in $B\,\overline{B}$ (and $c\bar{c}$) events. In addition to satisfying the `HadronB` selection, the event is retained also if at least one J/ψ candidate is found. A J/ψ candidate consists of two oppositely charged tracks with momentum above $0.8\,\mathrm{GeV}/c$ with invariant mass (assuming the pion-mass hypothesis) in the range of $[2.5, 4.0]\,\mathrm{GeV}/c^2$. In Belle II, we use `hlt_hadron` skim, which requests the presence of at least three good tracks with transverse momentum $p_{\rm T} > 0.2\,\mathrm{GeV}/c$, impact parameters $|d_0| < 2\,\mathrm{cm}$, $|z_0| < 4\,\mathrm{cm}$ and vetoes events consistent with Bhabha scattering.

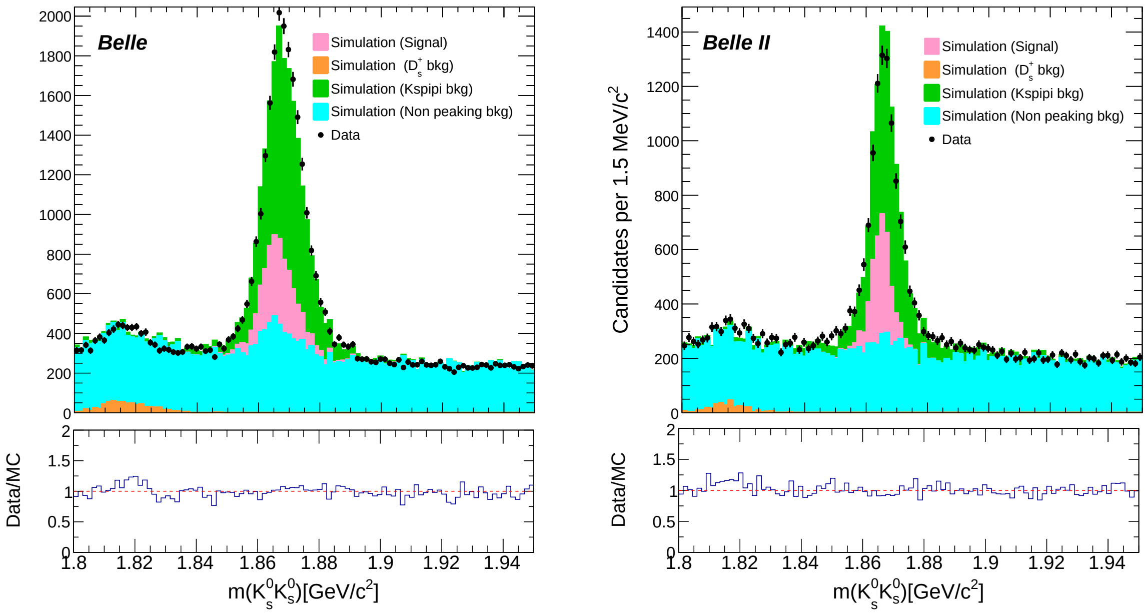

Figure 3.2: Distributions of $m(K_S^0 K_S^0)$ for $D^0 \to K_S^0 K_S^0$ candidates in (left) Belle and (right) Belle II simulation, with data overlaid. The simulation is normalized to the same luminosity as the data and is split into different sample components, which are stacked. The bottom panels show the data-to-simulation ratios. All selection requirements are applied except for the $m(K_S^0 K_S^0)$ requirement.

Candidate $K_S^0 \to \pi^+\pi^-$ decays are reconstructed using the `K_S0:mdst` list in Belle, and the `K_S0:merged` list in Belle II. In Belle II, the merged candidates reconstructed by the V0 tracking are given priority with respect to those reconstructed from combining oppositely charged pions. The K_S^0 candidates are fit with `TreeFitter` [57]. Only candidates with converged fits and satisfying the criteria $0.45 < m(\pi^+\pi^-) < 0.55\,\mathrm{GeV}/c^2$ are retained.

Pairs of K_S^0 candidates are combined to form candidate $D^0 \to K_S^0 K_S^0$ decays. The mass of the D^0 candidate, $m(K_S^0 K_S^0)$, is required to be in the range $[1.85, 1.89]\,\mathrm{GeV}/c^2$ for

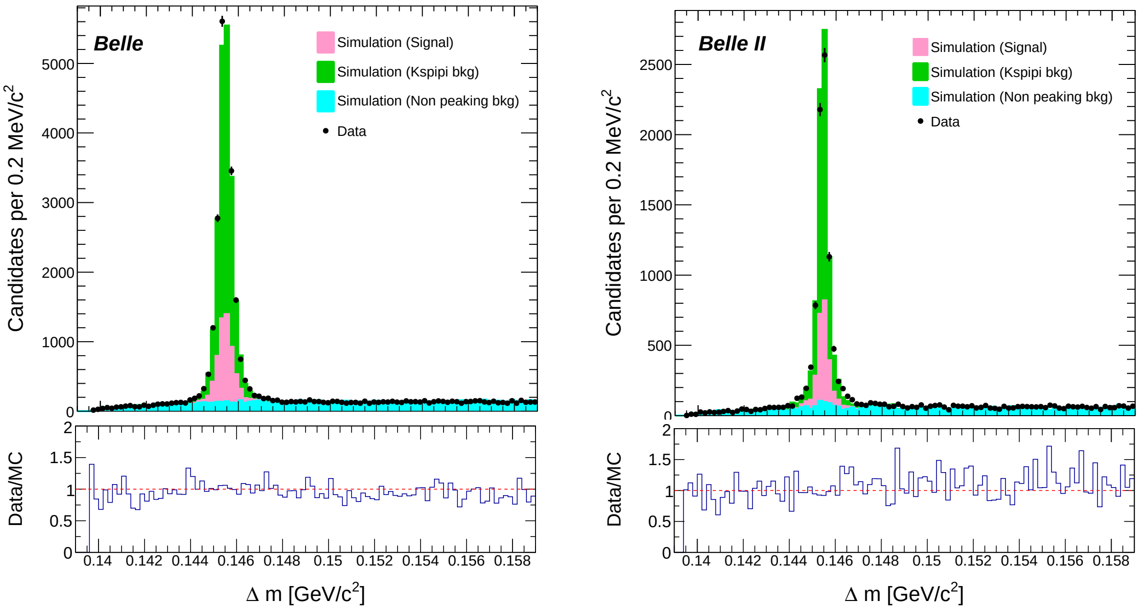

Figure 3.3: Distributions of Δm for $D^0 \to K^0_S K^0_S$ candidates in (left) Belle and (right) Belle II simulation, with data overlaid. The simulation is normalized to the same luminosity as the data and is split into different sample components, which are stacked. The small peaking contribution in the non-peaking background component of the Belle II plot is due to truth-matching failures of either signal or $D^0 \to K^0_S \pi^+\pi^-$ candidates. The bottom panels show the data-to-simulation ratios.

Belle and in the range $[1.85, 1.88]\,\mathrm{GeV}/c^2$ for Belle II. The different range is justified by an observed small offset in the signal-peak position and by the different mass resolution, as shown in Figure 3.2. Figure 3.2 shows an enhancement in the low-mass sideband, at around $1.81\,\mathrm{GeV}/c^2$. This is due to partially reconstructed $D_s^+ \to K^0_S K^0_S \pi^+$ decays, which have a branching fraction of 7.7×10^{-3} and do not appear to be present in the `EvtGen` decay file used in simulation.

The D^0 candidates are then combined with π_s pions to form a $D^{*+} \to D^0 \pi_s$ decay. The soft pion candidates are selected from the list of tracks that are in the CDC acceptance ($17^\circ < \theta < 150^\circ$) and are consistent with originating from the interaction point ($|d_r| < 0.5\,\mathrm{cm}$ and $|d_z| < 2\,\mathrm{cm}$). The difference between the reconstructed D^{*+} and D^0 masses, Δm, must not exceed $0.16\,\mathrm{GeV}/c^2$. The D^{*+} candidates are fit using `TreeFitter` by constraining the D^{*+} vertex to be consistent with the measured position of the beam interaction point (IP constraint) and by constraining the masses of the two K^0_S candidates to the nominal mass [23]. Only candidates with successful fits and having vertex-fit χ^2 probabilities larger than 10^{-3} are retained for subsequent analysis. The momenta of all final-state particles are updated with the results of the vertex fit. To suppress events where the D^{*+} candidate comes from the decay of a B meson, the momentum of the D^{*+} in the e^+e^- center-of-mass system (p_{cms}) is required to exceed $2.5\,\mathrm{GeV}/c$. Simulation shows that the surviving candidates from B meson decays are less than one per $1\,\mathrm{ab}^{-1}$.

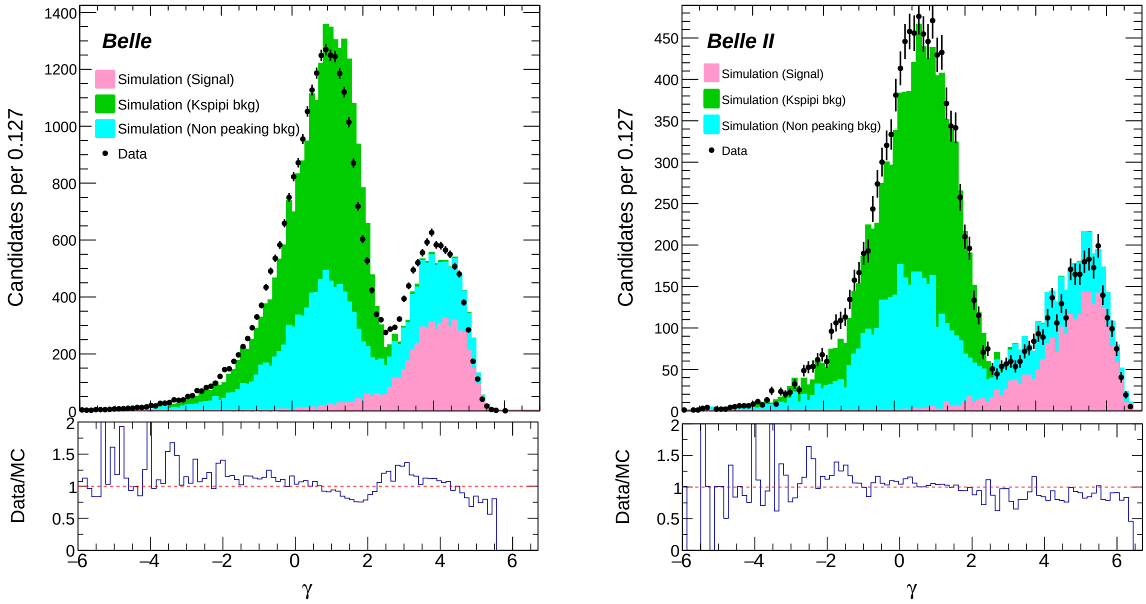

Figure 3.4: Distributions of γ for $D^0 \to K^0_S K^0_S$ candidates in (left) Belle and (right) Belle II simulation, with data overlaid. The simulation is normalized to the same luminosity as the data and is split into different sample components, which are stacked. The bottom panels show the data-to-simulation ratios.

Multiple D^{*+} candidates per event occur for about 3% of the events in Belle data. While in the case of Belle II data, they occur in about 2% of the events. In such cases, only the candidate with largest vertex-fit χ^2 probability is retained. The final list of selection criteria is summarized in Table 3.1.

Variable	Criteria
$\lvert d_r(\pi_s)\rvert$	$< 0.5\,\text{cm}$
$\lvert d_z(\pi_s)\rvert$	$< 2\,\text{cm}$
$\theta(\pi_s)$	$[17, 150]^\circ$
$m(\pi^+\pi^-)$	$[0.45, 0.55]\,\text{GeV}/c^2$
$m(K^0_S K^0_S)$	$[1.85, 1.89]\,\text{GeV}/c^2$ (Belle) or $[1.85, 1.88]\,\text{GeV}/c^2$ (Belle II)
Δm	$< 0.16\,\text{GeV}/c^2$
$p_{\text{cms}}(D^{*+})$	$> 2.5\,\text{GeV}/c$
`TreeFitter` probability	> 0.001
Best-candidate selection	D^{*+} candidate with largest `TreeFitter` probability

Table 3.1: Selection criteria for $D^{*+} \to D^0(\to K^0_S K^0_S)\pi^+$ candidates. `TreeFitter` is used with an IP constraint and with a K^0_S-mass constraint.

The Δm distributions of the selected candidates in data and simulation are shown in Figure 3.3. A clear peak at the expected value of the mass difference is observed over a smoothly distributed background. Candidates contributing to the peak include signal $D^{*+} \to D^0(\to K^0_S K^0_S)\pi^+$ decays and background $D^{*+} \to D^0(\to K^0_S \pi^+\pi^-)\pi^+$ decays. The latter have the same final state particles as the signal mode and therefore peak in both $m(K_S^0 K_S^0)$ and Δm distributions, with essentially the same distribution as the signal. Due to the K_S^0 mass constraint, it is difficult to separate such peaking background using the reconstructed masses of the two K_S^0 candidates. Therefore, we exploit the significance of the K_S^0 flight distance with respect to the D^0 decay vertex, L/σ_L. As shown in Figure 3.4, the logarithm of the smallest K_S^0 flight-distance significance, $\gamma = \log \min_{i=1,2} L^i/\sigma_L^i$, provides excellent separation power.[1] The non-peaking background is due to real $D^0 \to K_S^0 K_S^0$ or $D^0 \to K_S^0 \pi^+\pi^-$ candidates associated with an unrelated random π_s candidate and by unrelated combinations of final state particles (pure combinatorial background). The γ distribution of the non-peaking background component is also shown in Figure 3.4.

3.3.2 Asymmetry fit

The raw asymmetry of the signal decays is determined using an unbinned (and extended) fit to the two-dimensional $(\Delta m, \gamma)$ distribution of D^0 and $\overline{D}^0$ candidates. The fit considers three components: signal $D^0 \to K_S^0 K_S^0$ decays, peaking background from $D^0 \to K_S^0 \pi^+\pi^-$ decays, and non-peaking background (bkg). Simulation shows that, with a good approximation, the 2D probability distribution function (PDF) of each component factorizes into the product of the two 1D PDFs,

$$\text{pdf}^i(\Delta m, \gamma) = \text{pdf}^i(\Delta m)\text{pdf}^i(\gamma) \qquad (i = K_S^0 K_S^0, K_S^0\pi\pi, \text{bkg}), \tag{3.6}$$

and that no substantial differences are observed between PDFs of D^0 and $\overline{D}^0$ decays, which are then assumed to be identical (Appendix B). Possible asymmetries in the PDFs shapes are tested in the systematic studies, as discussed in Section 4.1.1.

The PDFs for the signal and peaking background component are derived using simulation. For signal, each of the Δm and γ distributions is modeled using a Johnson's S_U function [58]

$$J(x|\mu_J, \lambda_J, \delta_J, \gamma_J) \propto \frac{e^{-\frac{1}{2}\left[\gamma_J \,+\, \delta_J \,\sinh^{-1}\left(\frac{x-\mu_J}{\lambda_J}\right)\right]^2}}{\sqrt{1+\left(\frac{x-\mu_J}{\lambda_J}\right)^2}}\,, \tag{3.7}$$

as shown in Figure 3.5.

[1]Notice that L cannot be negative because there is no physical constraint on the D^0 decay vertex, which is just the point of intersection between the directions of the two K_S^0 candidates' momenta. It also never happens to be exactly zero, so the logarithm is always defined.

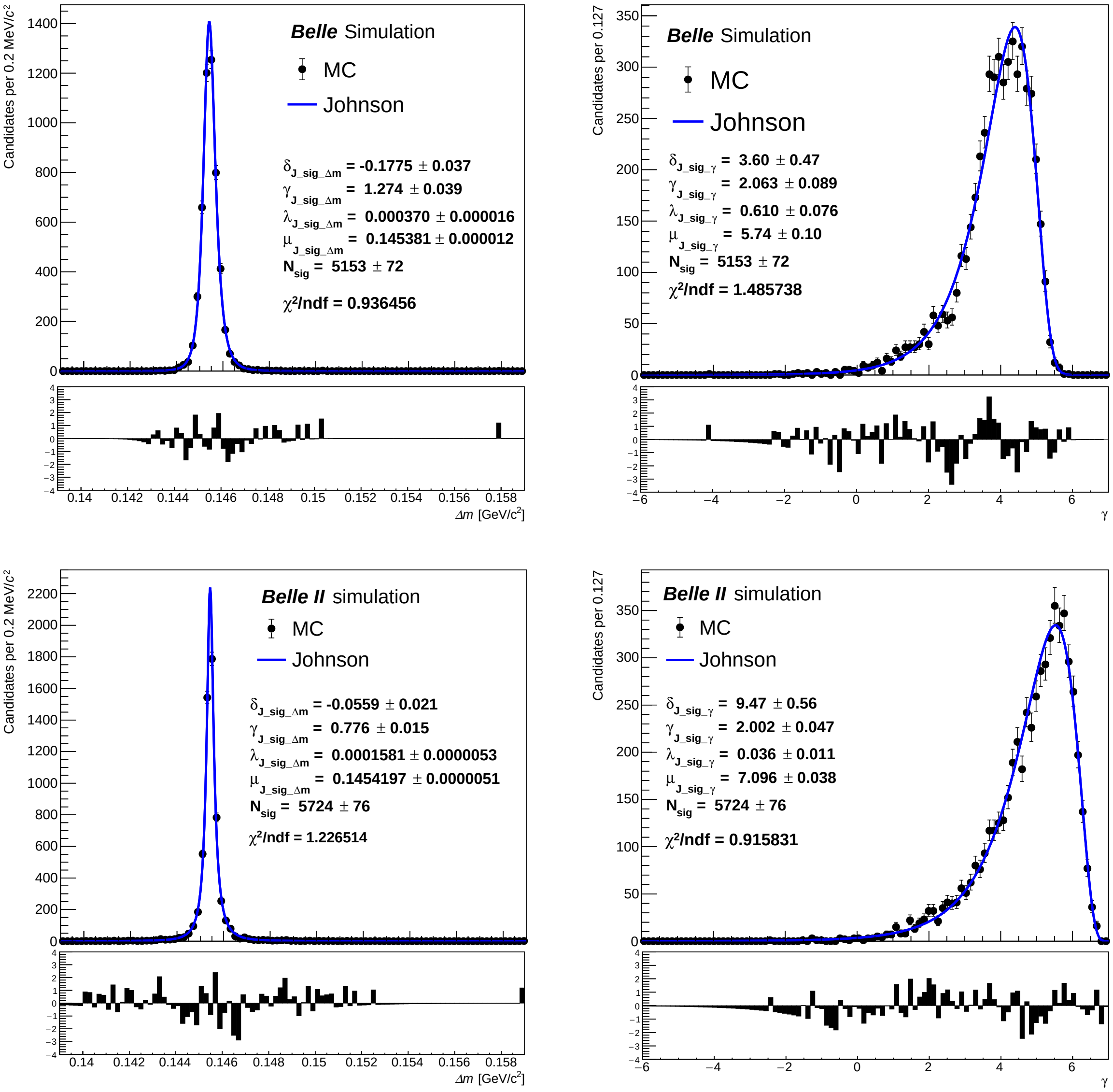

Figure 3.5: Distributions of (left) Δm and (right) γ for truth-matched signal candidates in (top) Belle and (bottom) Belle II simulation, with fit projections overlaid. The normalized residuals (pulls) are shown in the bottom panel of each plot.

The Δm PDF of the $D^0 \to K_S^0\pi^+\pi^-$ background is modelled using the sum of a Johnson's S_U and a Gaussian function with a common mean parameter for the Belle II analysis, while for the Belle analysis, it is modelled only with a Johnson 's S_U function,

$$\mathrm{pdf}^{K_S^0\pi^+\pi^-}(\Delta m) = f_J\, J(\Delta m|\mu_J, \lambda_J, \delta_J, \gamma_J) + (1 - f_J)G(\Delta m|\mu_J, \sigma_G)\,. \qquad (3.8)$$

The γ is modelled using a Johnson's S_U function. The distributions resulting from the fits to truth-matched $D^0 \to K_S^0\pi^+\pi^-$ background in simulation are shown in Figure 3.6.

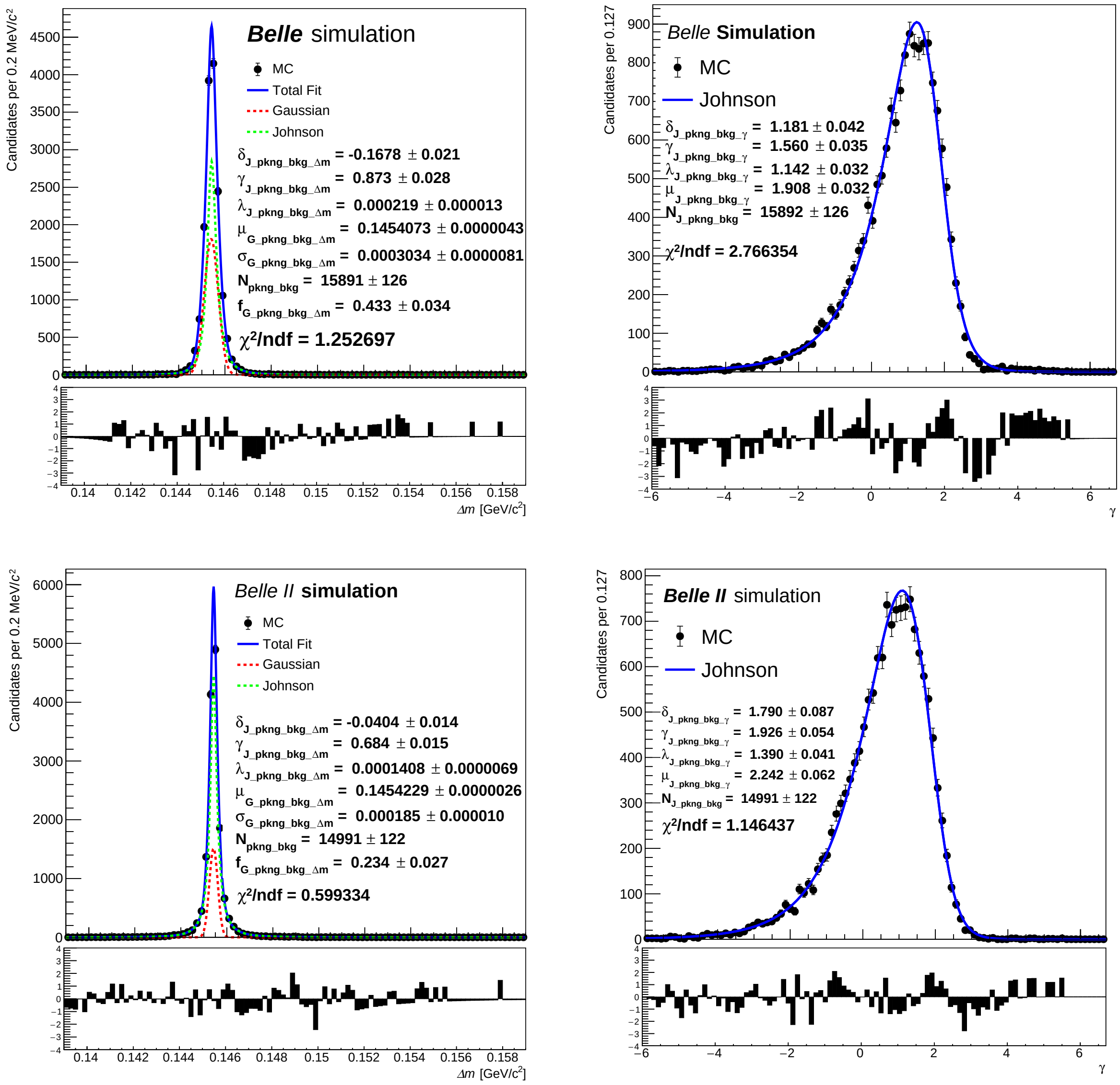

Figure 3.6: Distributions of (left) Δm and (right) γ for truth-matched $D^0 \to K^0_S\pi^+\pi^-$ background candidates in (top) Belle and (bottom) Belle II simulation, with fit projections overlaid. The normalized residuals (pulls) are shown in the bottom panel of each plot.

The Δm PDF of the non-peaking background is modeled empirically as a threshold-like distribution,

$$\mathrm{pdf}^{\mathrm{bkg}}(\Delta m) \propto (\Delta m - \Delta m_0)^{1/2} + \alpha(\Delta m - \Delta m_0)^{3/2} + \beta(\Delta m - \Delta m_0)^{5/2} \tag{3.9}$$

with threshold parameter Δm_0 fixed to the known value of the charged pion mass [23]. The value of the parameters α and β are determined directly from the fit to the data. The γ distribution is modeled as the sum of two Johnson S_U functions using data candidates populating the Δm sideband region $[0.14, 0.143] \cup [0.148, 0.158]$ GeV/c^2 (Figure 3.7).

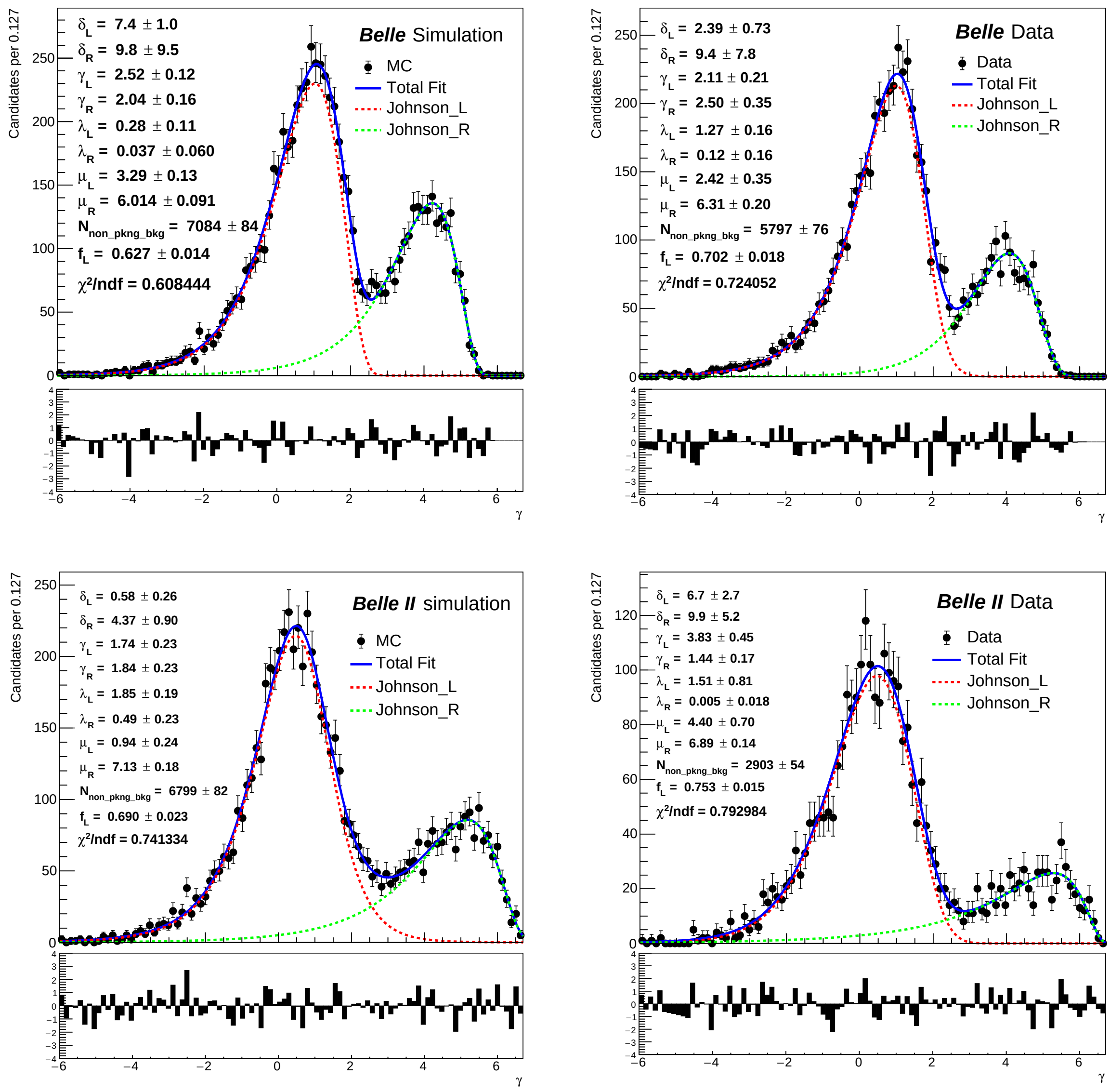

Figure 3.7: Distribution of γ in (left) simulation and (right) data for candidates populating the Δm side-band region for (top) Belle and (bottom) Belle II, with fit projections overlaid. The normalized residuals (pulls) are shown in the bottom panel of each plot.

Omitting the arguments to simplify the notation, the total fit function is

$$f^q(\Delta m, \gamma) = N^{K^0_S K^0_S}(1 + qA^{K^0_S K^0_S}_{\rm raw})\,{\rm pdf}^{K^0_S K^0_S} \\ + N^{K^0_S \pi\pi}(1 + qA^{K^0_S \pi\pi}_{\rm raw})\,{\rm pdf}^{K^0_S \pi\pi} \\ + N^{\rm bkg}(1 + qA^{\rm bkg}_{\rm raw})\,{\rm pdf}^{\rm bkg}, \quad (3.10)$$

where $q = 1$ (-1) for D^0 $(\overline{D}^0)$ candidates and N^i and $A^i_{\rm raw}$ are, respectively, the total yield and the raw asymmetry of the component i. The parameter α of the background is only shape parameter left free in the fit, together with the yields and asymmetries. All other parameters are fixed to their values as determined on simulation or data side-band.

Validation with pseudo experiments

To validate the fit procedure, 1000 pseudo experiments are generated by sampling from the PDFs and fit. The pseudo experiments reproduce the yields as observed in data and are generated assuming vanishing asymmetries. The results, shown in Figure 3.8, confirm that the fit estimates the signal yield and asymmetry, and their uncertainties, with no bias.

Additional sets of pseudo experiments are generated with varying values of the input signal asymmetry. Figure 3.9 shows the mean of the resulting pull distributions as a function of the generated asymmetry. In all cases the mean of the pull is consistent with zero, indicating that the fit determines the asymmetry correctly independently from its true value.

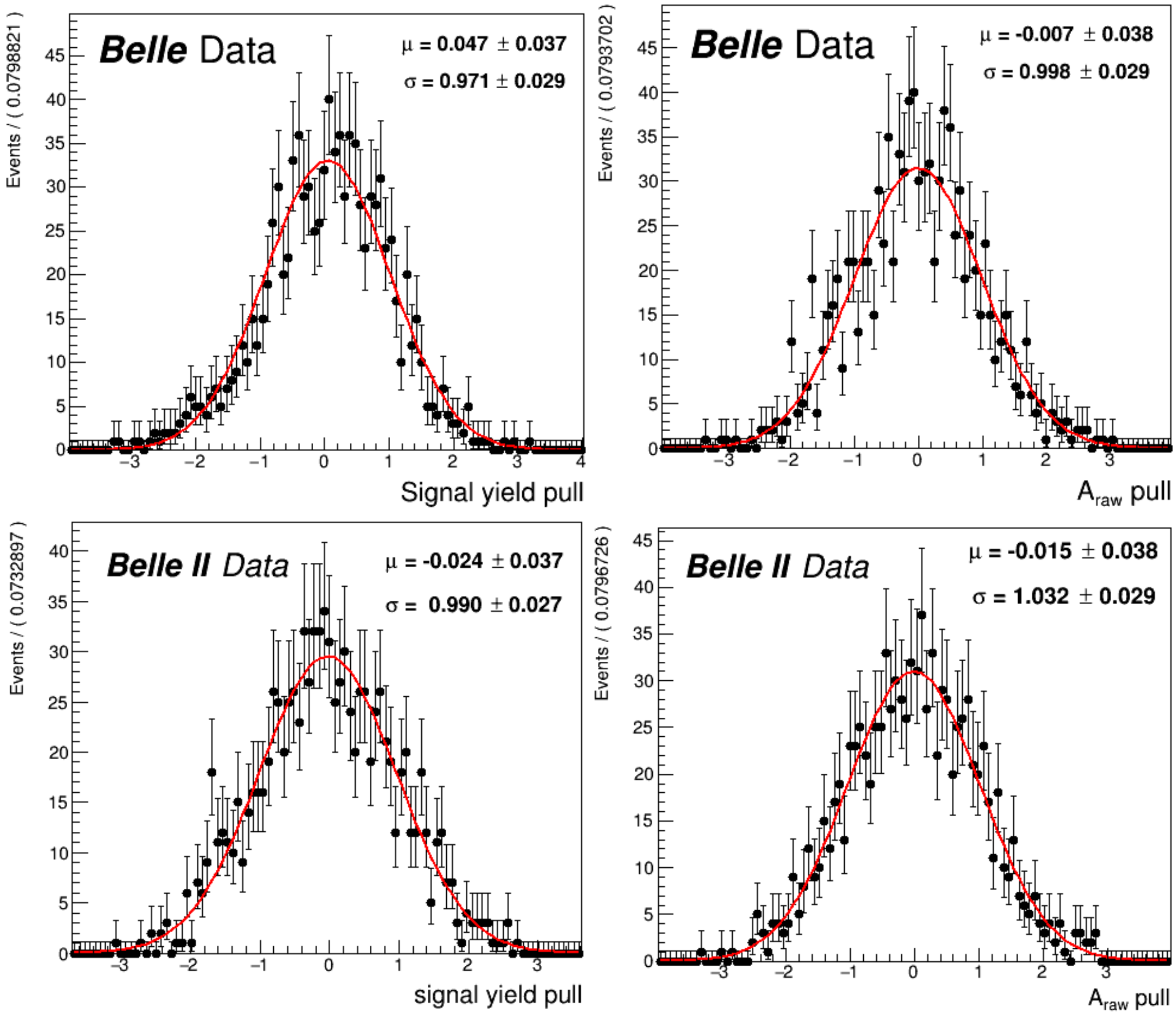

Figure 3.8: Pull distributions of the (left) signal yield and (right) signal raw asymmetry as determined by fitting to 1000 pseudo experiments sampled from the PDF mimicking the (top) Belle and (bottom) Belle II $D^0 \to K^0_S K^0_S$ sample. Gaussian fits are overlaid, showing that the distributions are consistent with having a null mean and a unit variance.

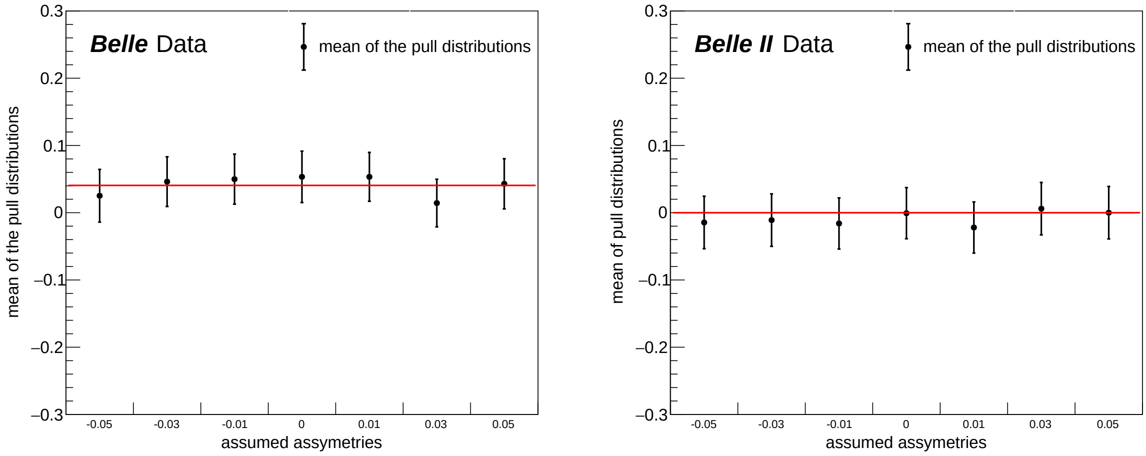

Figure 3.9: Mean of the pull distributions as a function of the generated signal asymmetry, as determined by fitting to 1000 pseudo experiments sampled from the PDF mimicking the (left) Belle and (right) Belle II $D^0 \to K^0_S K^0_S$ sample. Polynomial fits are overlaid, showing that the mean values of the pull distributions for different values of assumed asymmetries in the signal component consistent with zero.

3.3.3 Results on simulation

The results of the fit to the simulation are shown in Figures 3.10 and 3.11. For Belle, we show the results on streams 0+10. The signal yield is measured to be 5120 ± 81 in Belle and 5852 ± 83 in Belle II, in agreement with its truth-matching values of 5153 and 5724, respectively. The signal asymmetry is measured to be $(-0.9 \pm 1.6)\%$ in Belle and

Fit parameter	Measured value	Raw asymmetry (%)
$N^{K^0_S K^0_S}$	5120 ± 81	-0.9 ± 1.6
$N^{K^0_S \pi\pi}$	16247 ± 136	-1.53 ± 0.84
N^{bkg}	12419 ± 121	1.24 ± 0.96
α	-24.92 ± 0.94	–
β	0 (fixed)	–
$N^{K^0_S K^0_S}$	5852 ± 83	0.7 ± 1.4
$N^{K^0_S \pi\pi}$	15757 ± 135	1.51 ± 0.85
N^{bkg}	12122 ± 122	0.29 ± 0.99
α	-28.56 ± 0.85	-
β	0 (fixed)	–

Table 3.2: Measured values of the parameters obtained from the fit to $D^0 \to K^0_S K^0_S$ sample in (top) Belle and (bottom) Belle II simulation. The Belle sample corresponds to streams 0+10. The uncertainties are statistical only. The parameter β is found to be consistent with zero and therefore its value is fixed to zero.

$(0.7 \pm 1.4)\%$ in Belle II, consistent with the truth-matching values of -0.7% and 0.1%, respectively. The complete set of measured fit parameters are tabulated in Table 3.2.

Correlations coefficients are reported in Appendix A.

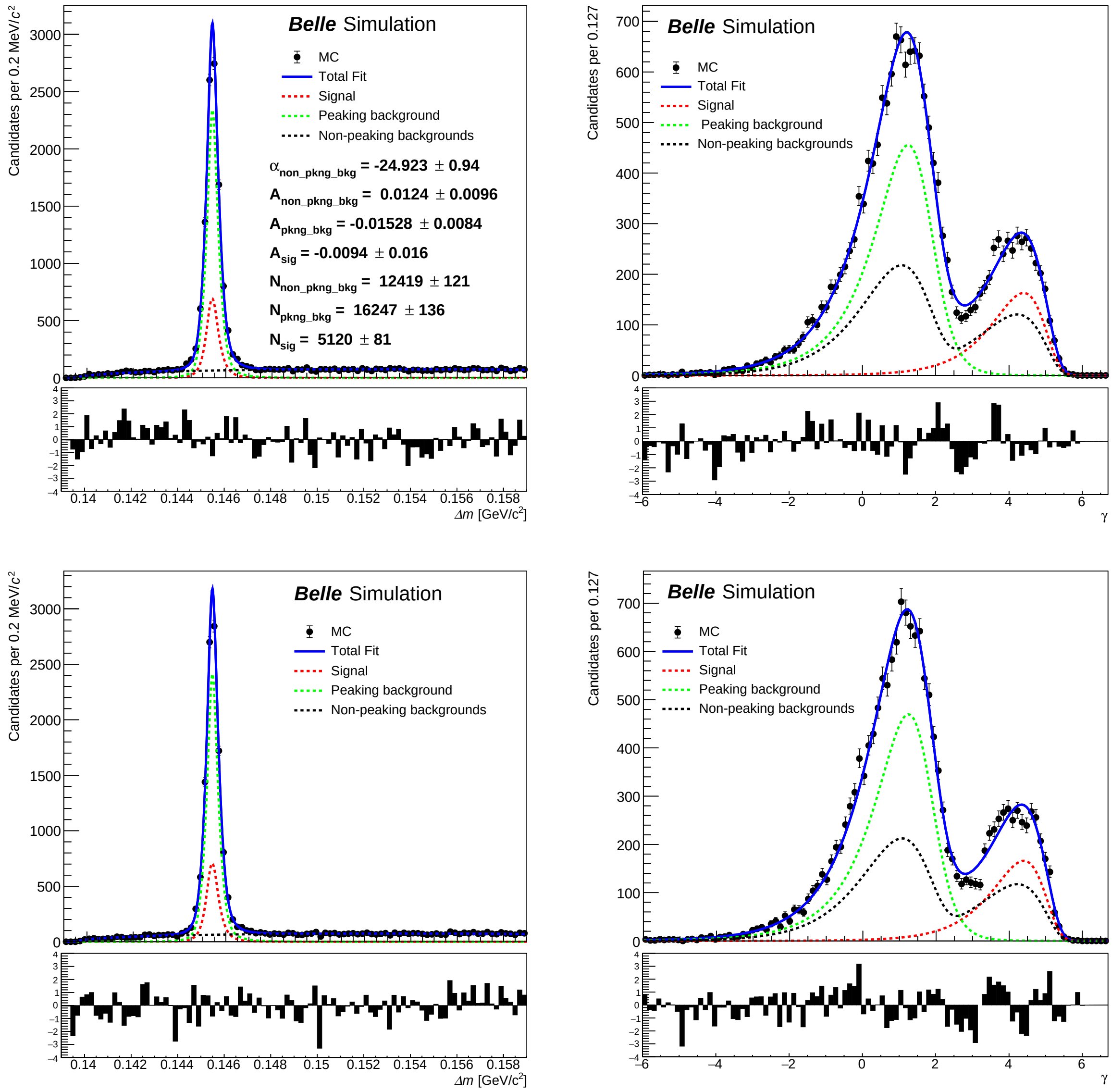

Figure 3.10: Distributions of (left) Δm and (right) γ for (top) $D^0 \to K^0_S K^0_S$ and (bottom) $\overline{D}^0 \to K^0_S K^0_S$ candidates in Belle simulation (streams 0+10), with fit projections overlaid. The normalized residuals (pulls) are shown in the bottom panel of each plot.

Streams	$A_{\mathrm{raw}}^{K^0_S K^0_S}$ (%)
0+10	-0.9 ± 1.6
1+11	0.3 ± 1.6
2+12	-1.5 ± 1.6
3+13	0.7 ± 1.6
4+14	1.7 ± 1.6
5+15	1.8 ± 1.6

Table 3.3: Measured values of $A_{\mathrm{raw}}^{K^0_S K^0_S}$ from fits to samples corresponding to different $980\,\mathrm{fb}^{-1}$ streams of the Belle simulation. The uncertainties are statistical only.

To complete the validation we perform the fit using all the available streams of Belle MC, each corresponding to an integrated luminosity of 980 fb^{-1}. The measured values of A_{raw}, shown in Table 3.3, are all in agreement with each other and with the truth-matching asymmetry.

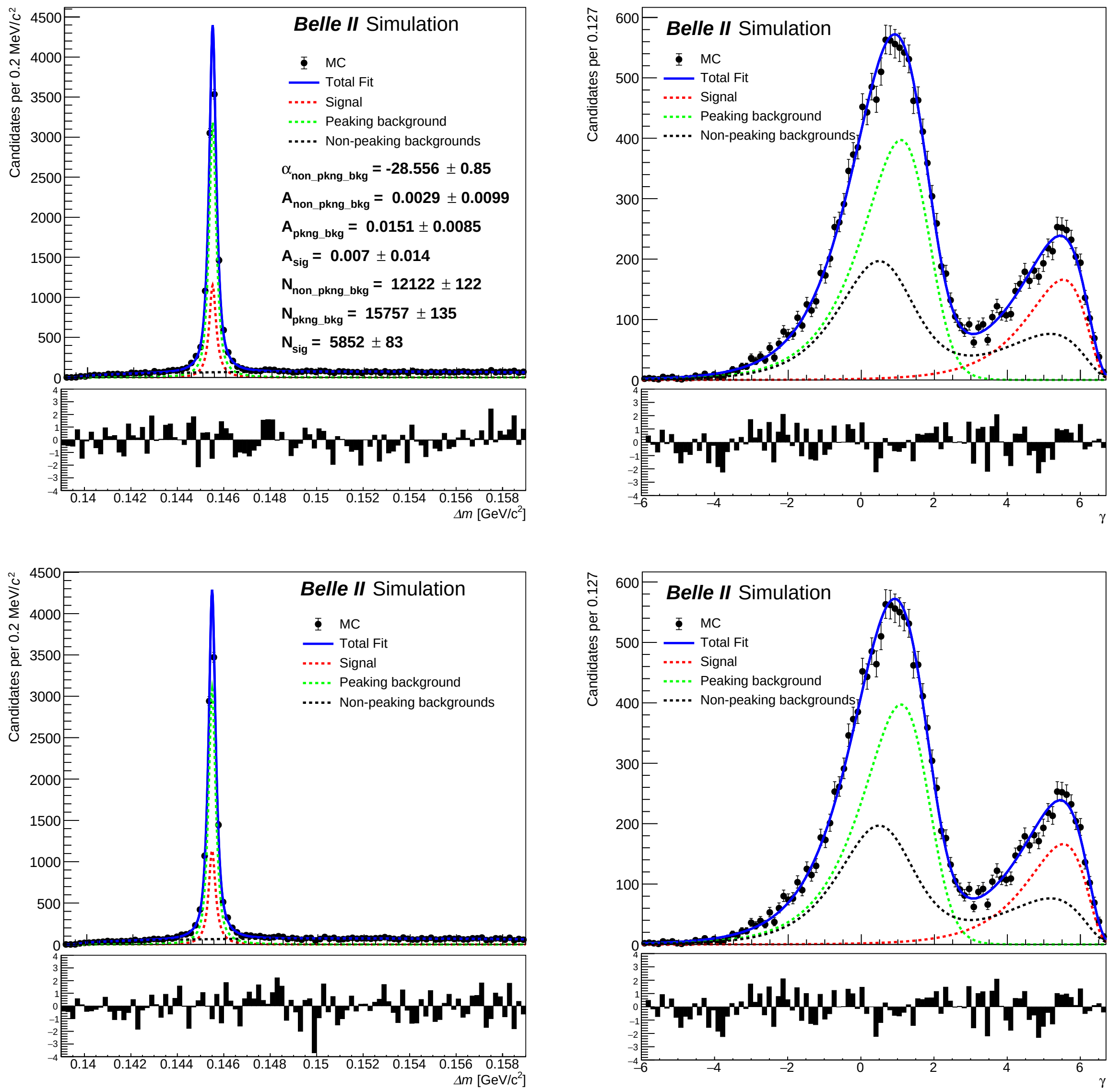

Figure 3.11: Distributions of (left) Δm and (right) γ for (top) $D^0 \to K_S^0 K_S^0$ and (bottom) $\overline{D}^0 \to K_S^0 K_S^0$ candidates in Belle II simulation, with fit projection overlaid. The normalized residuals (pulls) are shown in the bottom panel of each plot.

Similarly, we perform fits to three subsets of the Belle II simulation, each corresponding to an integrated luminosity of 400 fb^{-1}. The measured A_{raw} values are in agreement and are shown in Table 3.4.

Streams	$A_{\rm raw}^{K_S^0 K_S^0}$ (%)
1	0.0 ± 2.2
2	2.6 ± 2.2
3	0.7 ± 2.2

Table 3.4: Measured values of $A_{\rm raw}^{K_S^0 K_S^0}$ from fits to samples corresponding to $400\,\text{fb}^{-1}$ subsets of the Belle II simulation.

3.3.4 Results on data

When fitting the data, the value of the signal asymmetry is blinded to prevent any potential bias. The blinding is implemented using a random offset sampled uniformly in the range $[-0.1, 0.1]$ and is the same in Belle and Belle II data. The results of the fit to the data are shown in Figures 3.12 and 3.13.

Fit parameter	Measured value	Raw asymmetry (%)
$N^{K_S^0 K_S^0}$	4864 ± 78	1.2 ± 1.6
$N^{K_S^0 \pi\pi}$	15047 ± 131	-1.09 ± 0.87
$N^{\rm bkg}$	10377 ± 111	-0.3 ± 1.1
α	-25.9 ± 1.0	-
$N^{K_S^0 K_S^0}$	2214 ± 51	1.6 ± 2.3
$N^{K_S^0 \pi\pi}$	5789 ± 83	-1.3 ± 1.4
$N^{\rm bkg}$	5269 ± 80	0.8 ± 1.5
α	-25.9 ± 1.4	-

Table 3.5: .
Measured values of the parameters obtained from the fit to $D^0 \to K_S^0 K_S^0$ sample in (top) Belle and (bottom) Belle II data. The uncertainties are statistical only.

The measured signal yields are 4864 ± 78 in Belle and 2214 ± 51 in Belle II. The yields per $1\,\text{fb}^{-1}$ of unit luminosity are 4.96 ± 0.08 for Belle and 5.26 ± 0.12 for Belle II, in agreement between them and with the previous Belle result of Ref. [51] when the same $p_{\rm cms}(D^{*+})$ requirement is applied (4755 ± 75). The raw asymmetry is measured to be (1.2 ± 1.6)% in Belle and (1.6 ± 2.3)% in Belle II, in agreement between the two samples. The complete set of measured fit parameters are tabulated in Table 3.5. Correlations coefficients are reported in Appendix A.

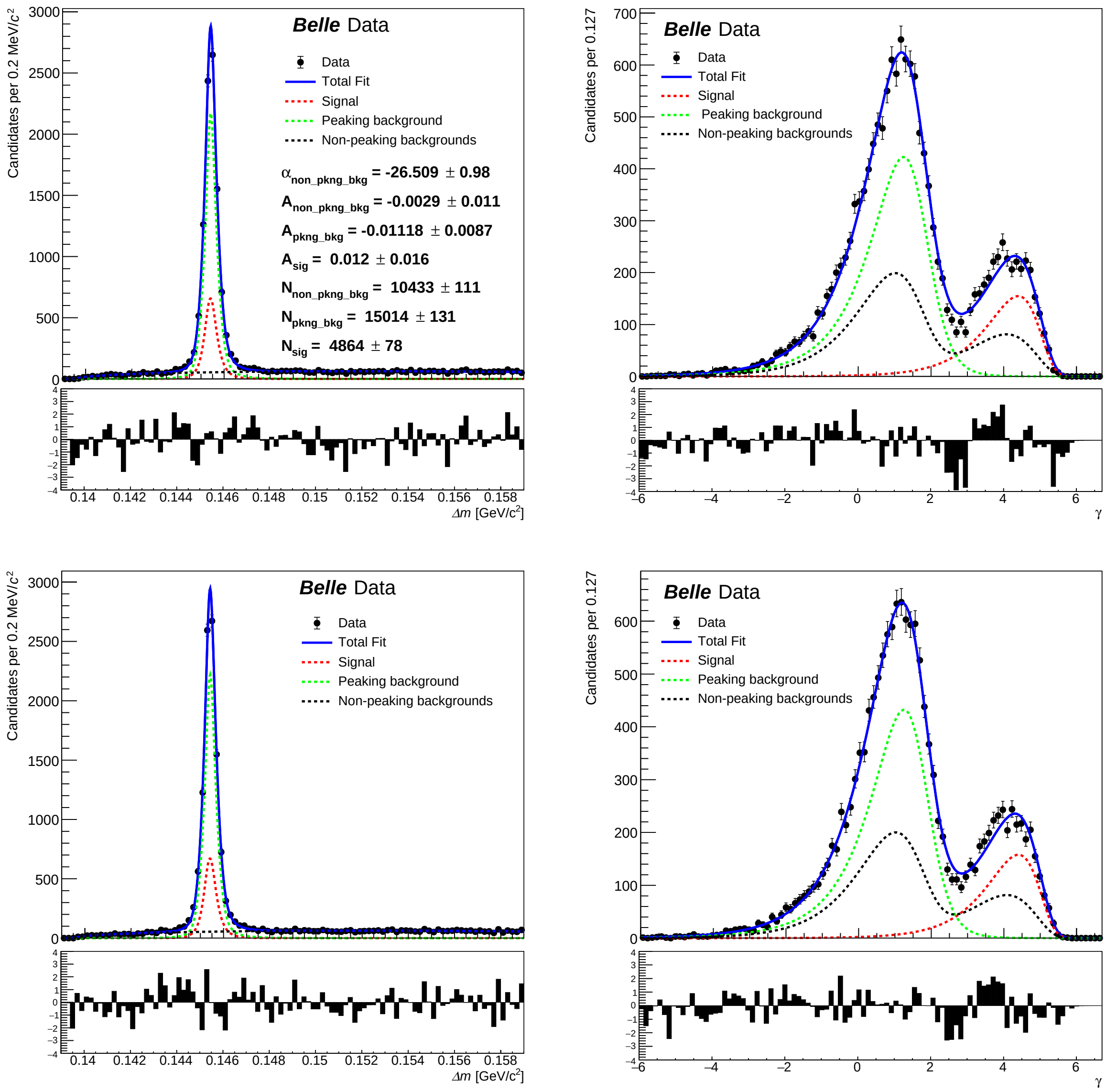

Figure 3.12: Distributions of (left) Δm and (right) γ for (top) $D^0 \to K^0_S K^0_S$ and (bottom) $\overline{D}^0 \to K^0_S K^0_S$ candidates in Belle data, with fit projection overlaid. The normalized residuals (pulls) are shown in the bottom panel of each plot.

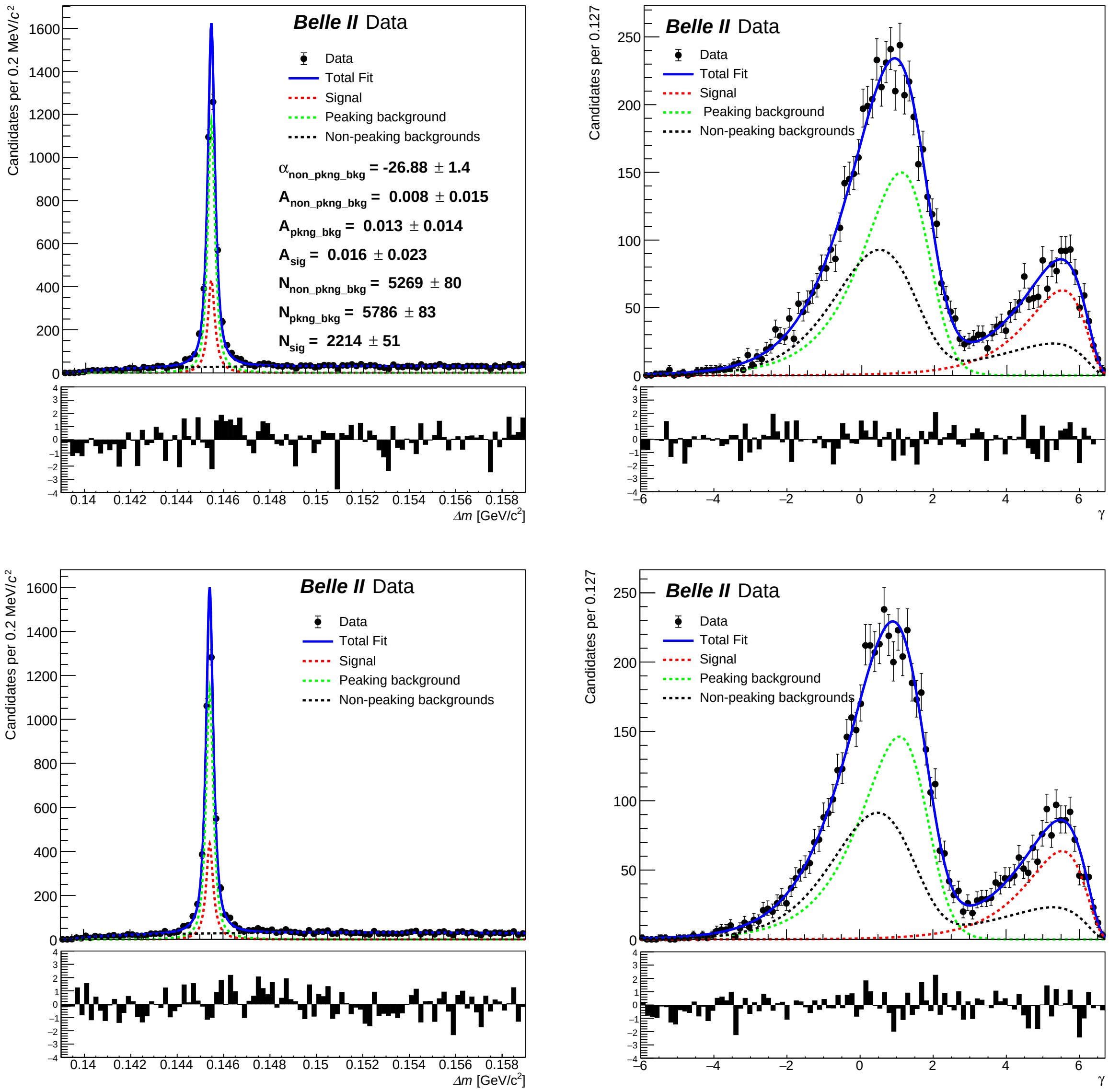

Figure 3.13: Distributions of (left) Δm and (right) γ for (top) $D^0 \to K^0_S K^0_S$ and (bottom) $\overline{D}^0 \to K^0_S K^0_S$ candidates in Belle II data, with fit projection overlaid. The normalized residuals (pulls) are shown in the bottom panel of each plot.

3.4 Determination of A_{raw} in $D^0 \to K^+K^-$ decays

3.4.1 Event selection

The control sample of $D^{*+} \to D^0(\to K^+K^-)\pi^+$ decays is reconstructed starting from the `HadronB(J)` skim in Belle and from the `hlt_hadron` skims in Belle II. Candidate kaons are reconstructed from tracks in the CDC acceptance with $|d_r| < 0.5\,\mathrm{cm}$, $|d_z| < 2\,\mathrm{cm}$, at least 21 CDC hits and at least 1 SVD hit. To suppress backgrounds arising from misidentification of the charged kaons with pions or electrons, they are required to satisfy $\mathcal{L}_K/(\mathcal{L}_K + \mathcal{L}_\pi) > 0.6$ and $\mathcal{L}_K/(\mathcal{L}_K + \mathcal{L}_e) > 0.1$, where $\mathcal{L}_x$ is the PID likelihood for the hypothesis x.

Variable	Criteria
$\lvert d_r\rvert(\pi_s, K^\pm)$	$< 0.5\,\mathrm{cm}$
$\lvert d_z\rvert(\pi_s, K^\pm)$	$< 2\,\mathrm{cm}$
$\theta(\pi_s, K^\pm)$	$[17, 150]^\circ$
# CDC hits ($K^\pm$)	> 20
# SVD hits ($K^\pm$)	> 0
$\mathcal{L}_K/(\mathcal{L}_K + \mathcal{L}_{\pi/e})(K^\pm)$	0.6/0.1
$m(K^+K^-)$	$[1.75, 2.05]\,\mathrm{GeV}/c^2$
Δm	$< 0.16\,\mathrm{GeV}/c^2$
$p_{\mathrm{cms}}(D^{*+})$	$> 2.5\,\mathrm{GeV}/c$
`TreeFitter` probability	> 0.001
Best-candidate selection	D^{*+} candidate with largest `TreeFitter` probability

Table 3.6: Selection criteria for $D^{*+} \to D^0(\to K^+K^-)\pi^+$ candidates. `TreeFitter` is used with an IP constraint.

Candidate D^0 mesons are formed by combining pairs of oppositely charged kaons with mass, $m(K^+K^-)$, in the range $[1.75, 2.05]\,\mathrm{GeV}/c^2$. The D^0 mesons thus reconstructed are then combined with soft-pion candidates to form a $D^{*+} \to D^0\pi_s$ decay. The soft pions are tracks in the CDC acceptance with $|d_r| < 0.5\,\mathrm{cm}$ and $|d_z| < 2\,\mathrm{cm}$. The D^{*+} candidates are required to have $\Delta m < 0.16\,\mathrm{GeV}/c^2$ and are fit using `TreeFitter` using an IP constraint. Only candidates with successful fits and having vertex-fit χ^2 probabilities larger than 10^{-3} are retained for subsequent analysis. The momenta of all final-state particles are updated with the results of the vertex fit. To suppress events where the D^{*+} candidate comes from the decay of a B meson, the momentum of the D^{*+} in the e^+e^- center-of-mass system is required to exceed $2.5\,\mathrm{GeV}/c$. Simulation shows that about five candidates from B meson decays, per $1\,\mathrm{ab}^{-1}$ of integrated luminosity at the $\Upsilon(4S)$, survive this requirement.

Multiple D^{*+} candidates occur in about 2% events in both Belle and Belle II data. In such cases, only the candidate with largest vertex-fit χ^2 probability is retained. The final list of selection criteria is summarized in Table 3.6.

The $m(K^+K^-)$ and $m(D^0\pi_s)$ distributions of the selected candidates in data and simulation are shown in Figure 3.14. The two-body $D^0\pi_s$ mass, $m(D^0\pi_s)$, is computed using the D^0 momentum and the nominal D^0 mass [23] to compute the D^0 energy. Using $m(D^0\pi_s)$ simplifies the treatment of the background decays in which a D^0 final-state particle is mis-identified because, unlike the conventional Δm, its computation does not assume any mass hypotheses for the D^0 final-state particles resulting in all $D^{*+} \to D^0 \to (h^+h'^-)\pi^+$ $(h, h' = K, \pi)$ decays having identical $m(D^0\pi_s)$ distributions [59].

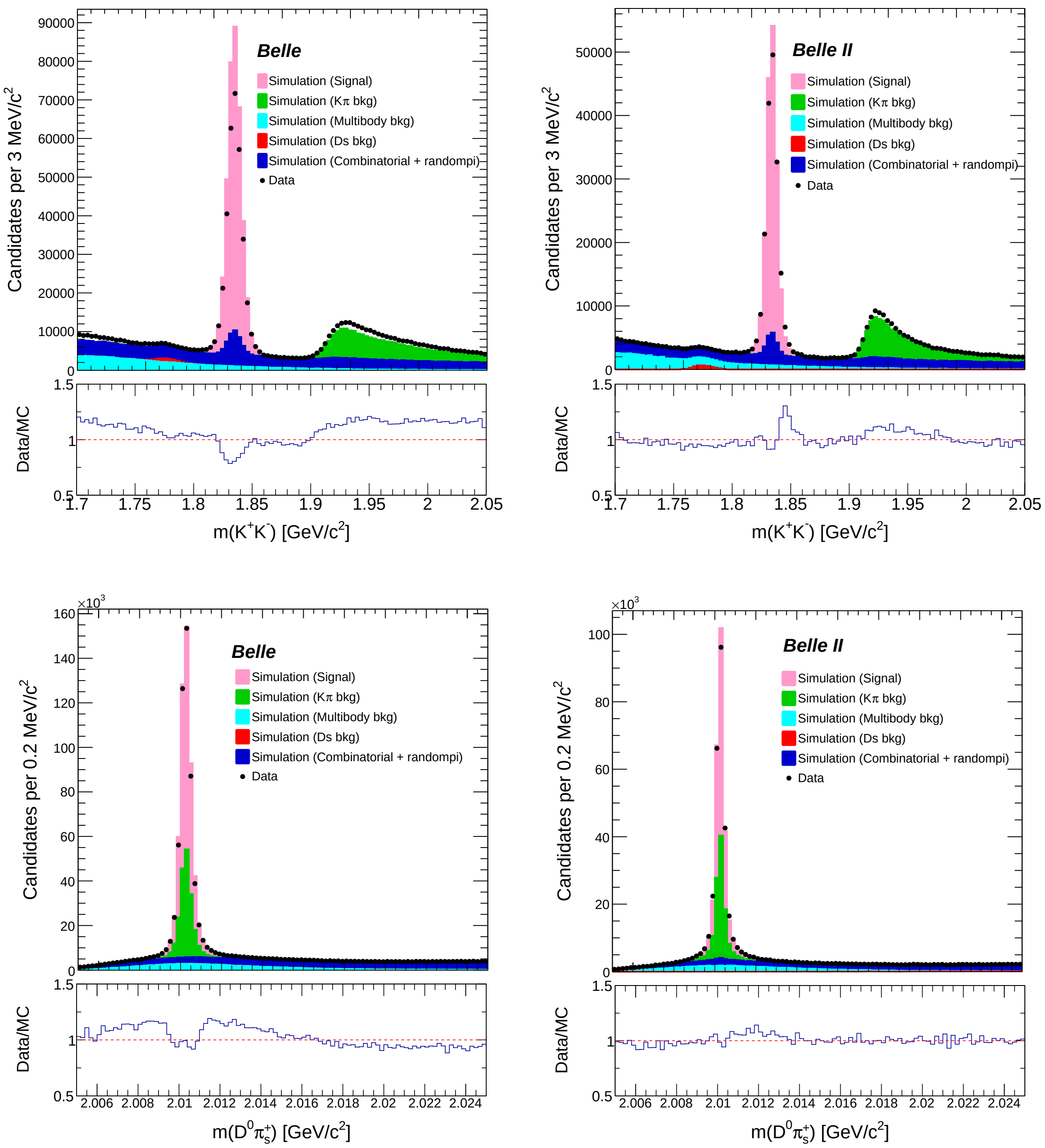

Figure 3.14: Distributions of (top) $m(K^+K^-)$ and (bottom) $m(D^0\pi_s)$ for $D^0 \to K^+K^-$ candidates in (left) Belle and (right) Belle II simulation, with data overlaid. The simulation is normalized to the same luminosity as the data and is split into different sample components, which are stacked. The bottom panels show the data-to-simulation ratios.

Clear peaks from correctly reconstructed $D^{*+} \to D^0(\to K^+K^-)\pi^+$ decays at the expected values of the nominal D^0 and D^{*+} masses are observed over the background. The background is composed by $D^0 \to K^-\pi^+$ decays in which the pion is mis-identified as a kaon, peaking at $m(K^+K^-)$ values around $1.94\,\text{GeV}/c^2$; by partially reconstructed $D^0 \to$ multibody decays where multibody indicates decays, such as $D^0 \to K^-\pi^+\pi^0$, where the charged pion is mis-identified as a kaon and the neutral pion is not reconstructed, or semileptonic D^0 decays where the neutrino is not reconstructed, populate mostly the low-$m(K^+K^-)$ region; by $D_s^+ \to K^+K^-\pi^+$ decays in which π^+ is reconstructed as a π_s candidate, peaking at $m(K^+K^-)$ values around $1.82\,\text{GeV}/c^2$; and by combinatorial background populating the entire $m(K^+K^-)$ nearly uniformly. Each D^0 background component can either be associated with a real π_s candidate, hence peaking in $m(D^0\pi_s)$ mass, or with an unrelated π_s candidate, hence contributing to the random-pion background. The D_s^+ background has a smooth distribution, which rises almost linearly in $m(D^0\pi_s)$.

3.4.2 Kinematic equalization

The D^{*+} forward-backward asymmetry is expected to vary as a function the D^{*+} polar angle.[2] The π_s detection asymmetry is expected to vary both as a function of momentum and of polar angle. To ensure a precise cancellation of these nuisance asymmetries in Equation (3.4), the D^{*+} and π_s kinematic distributions of the control sample must coincide with those of the signal sample. Simulation shows that, because of the different selection criteria, small differences are present (Figures 3.15 and 3.16). A weighting procedure is therefore implemented to reduce the observed differences. We fit a six-order polynomial to the ratio between the $\cos\theta(D^{*+})$ distributions of truth-matched $D^0 \to K_S^0 K_S^0$ and $D^0 \to K^+K^-$ decays in simulation. The projections of the fit are shown in Figures 3.15 and 3.16. The resulting functions,

$$f(\cos\theta) = 0.984751 - 0.13327\cos\theta + 0.276899\cos^2\theta + 0.453082\cos^3\theta - 0.08738\cos^4\theta - 1.00713\cos^5\theta \quad (3.11)$$

for Belle and

$$f(\cos\theta) = 0.889752 - 0.110344\cos\theta + 0.961291\cos^2\theta - 0.220356\cos^3\theta - 0.0826763\cos^4\theta - 3.09148\cos^5\theta + 2.45831\cos^6\theta \quad (3.12)$$

for Belle II, are used to compute a per-candidate weight for the $D^0 \to K^+K^-$ control sample. The effect of the weighting on simulated and truth-matched control sample decays is shown in Figures 3.17 and 3.18. Weighting as a function of $\cos\theta(D^{*+})$ reduces the differences also in the other kinematic distribution.

[2] Neglecting possible efficiency effects, because of the *CP* symmetric initial state, the forward-backward asymmetry is expected to be an odd function of the cosine of the polar angle in the c.m.s.

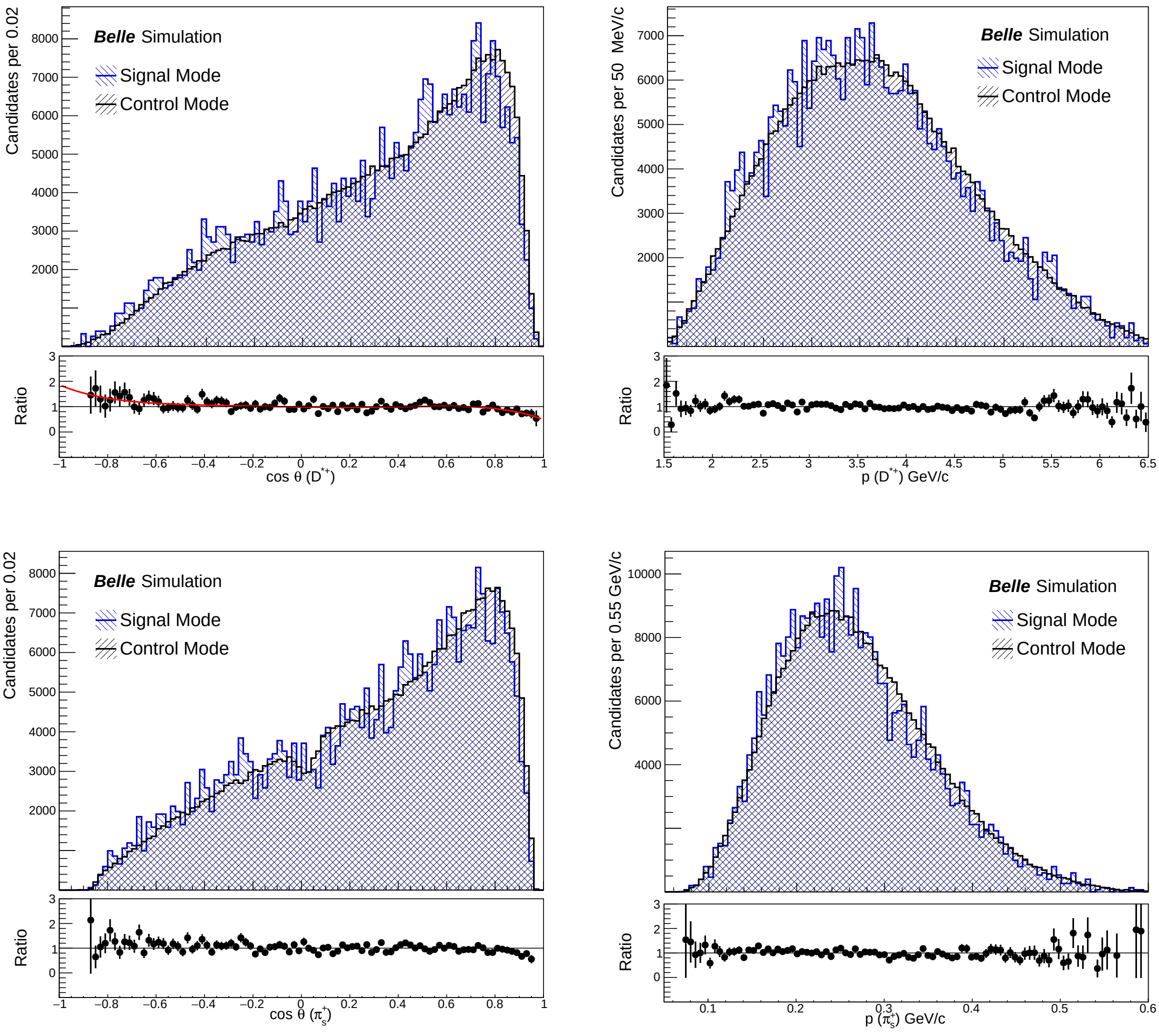

Figure 3.15: Normalized distributions of (top-left) $\cos\theta(D^{*+})$, (top-right) $p(D^{*+})$, (bottom-left) $\cos\theta(\pi_s)$ and (bottom-right) $p(\pi_s)$ of truth-matched signal and control decays in Belle simulation. The ratio between the two samples are shown in the bottom panel of each plot.

To check that the weighting functions determined on simulation work also on data (Figures 3.19 and 3.20), we evaluate the effect of the weighting procedure on background-subtracted signal and control decays in data. The background subtraction is performed using the sPlot method [60] with weights derived from the fits discussed in Section 3.4.3. Figures 3.21 and 3.22 show the results, confirm that the weighting functions from simulation are effective also in data.

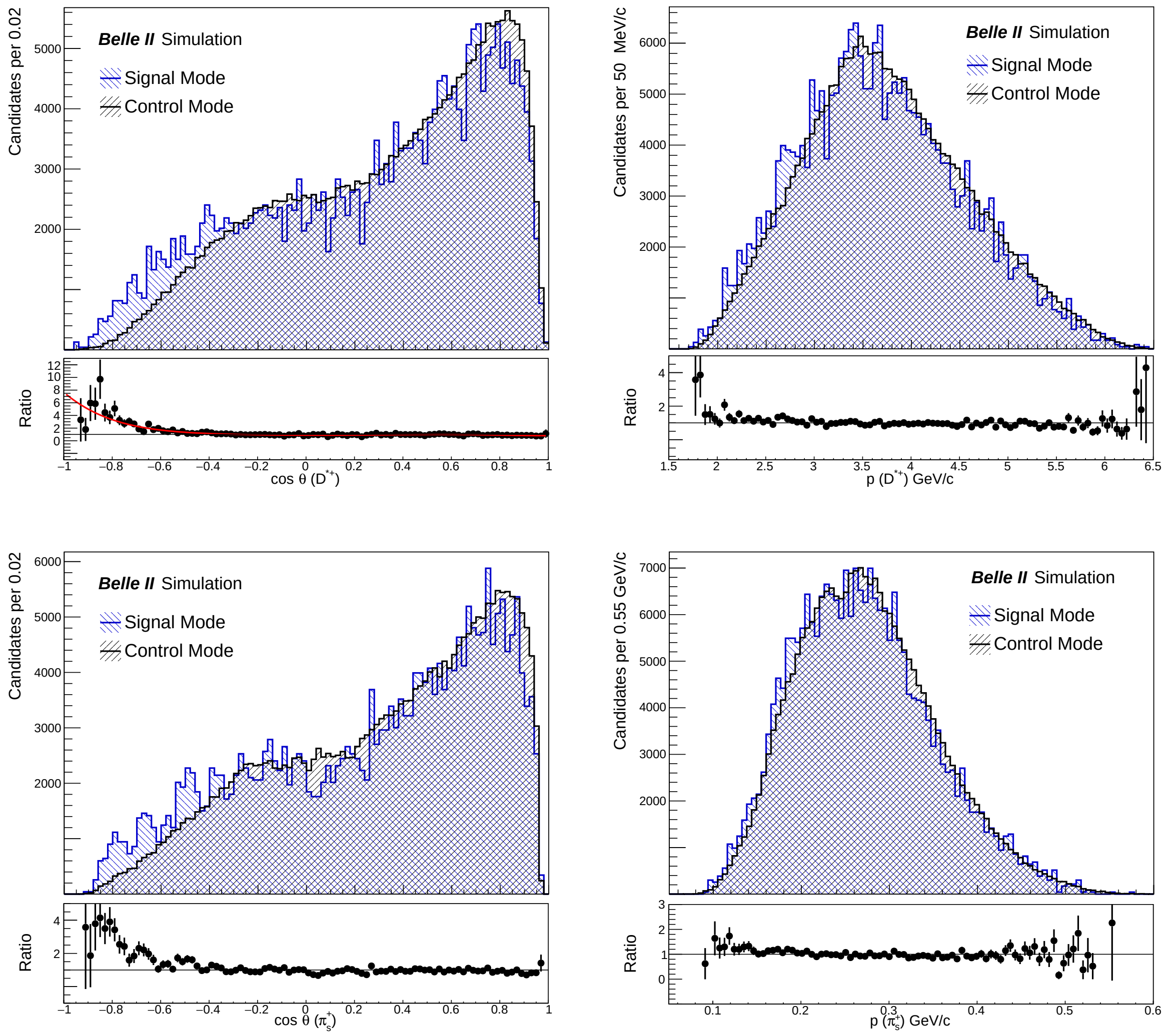

Figure 3.16: Normalized distributions of (top-left) $\cos\theta(D^{*+})$, (top-right) $p(D^{*+})$, (bottom-left) $\cos\theta(\pi_s)$ and (bottom-right) $p(\pi_s)$ of truth-matched signal and control decays in Belle II simulation. The ratio between the two samples are shown in the bottom panel of each plot.

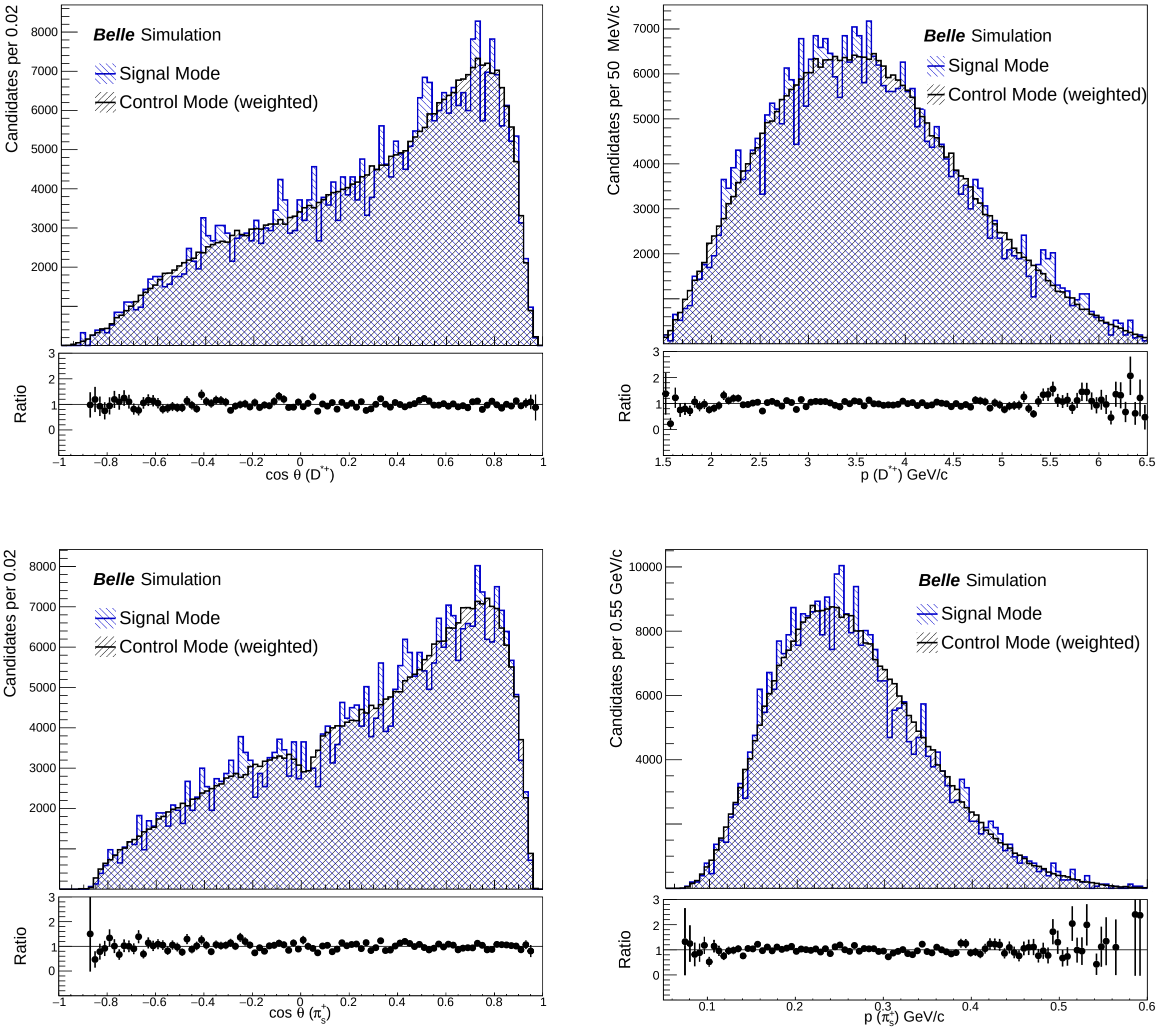

Figure 3.17: Normalized distributions of (top-left) $\cos\theta(D^{*+})$, (top-right) $p(D^{*+})$, (bottom-left) $\cos\theta(\pi_s)$ and (bottom-right) $p(\pi_s)$ of truth-matched signal and control decays in Belle simulation. The control decays are weighted in $\cos\theta(D^{*+})$. The ratio between the two samples are shown in the bottom panel of each plot.

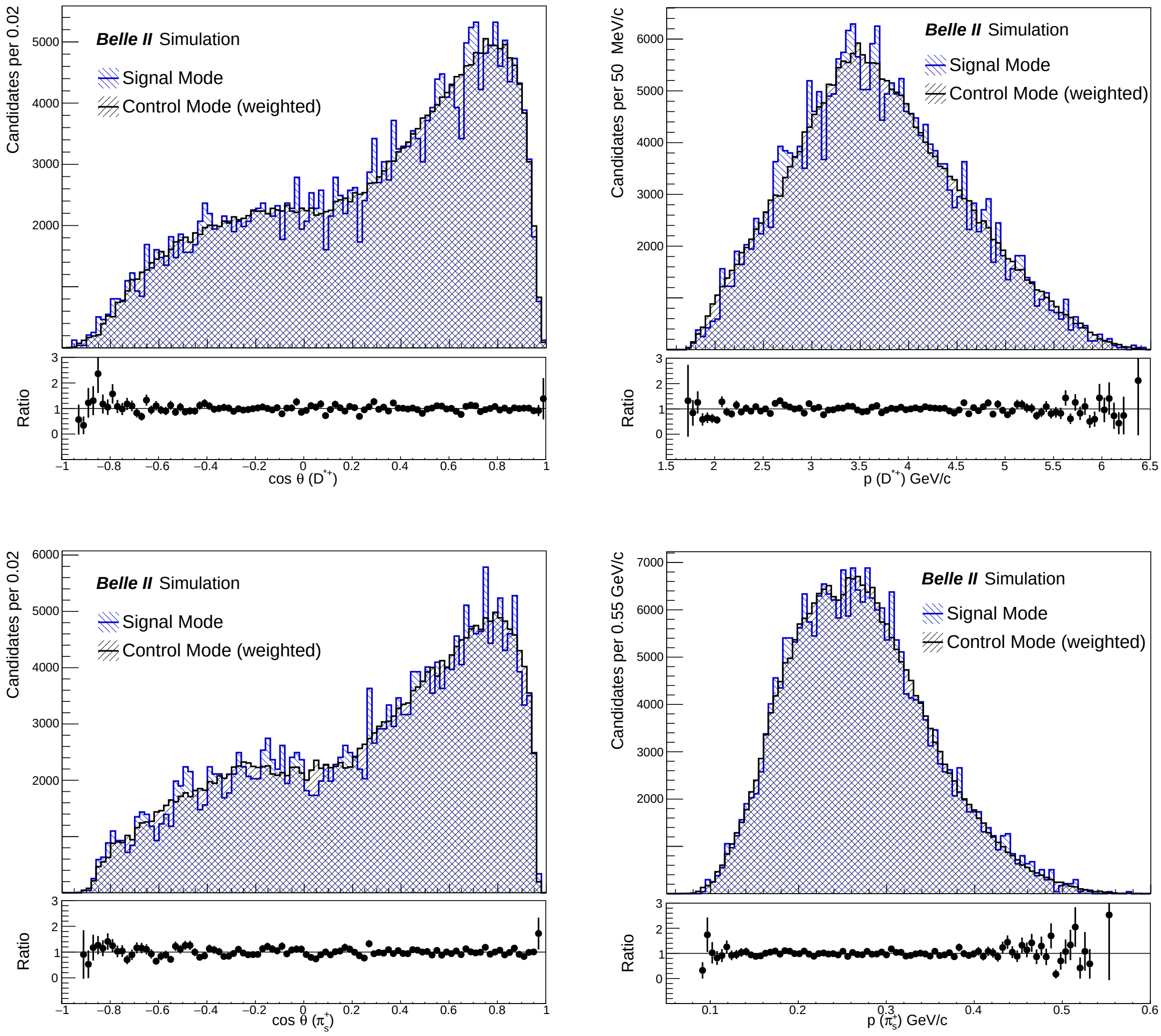

Figure 3.18: Normalized distributions of (top-left) $\cos\theta(D^{*+})$, (top-right) $p(D^{*+})$, (bottom-left) $\cos\theta(\pi_s)$ and (bottom-right) $p(\pi_s)$ of truth-matched signal and control decays in Belle II simulation. The control decays are weighted in $\cos\theta(D^{*+})$. The ratio between the two samples are shown in the bottom panel of each plot.

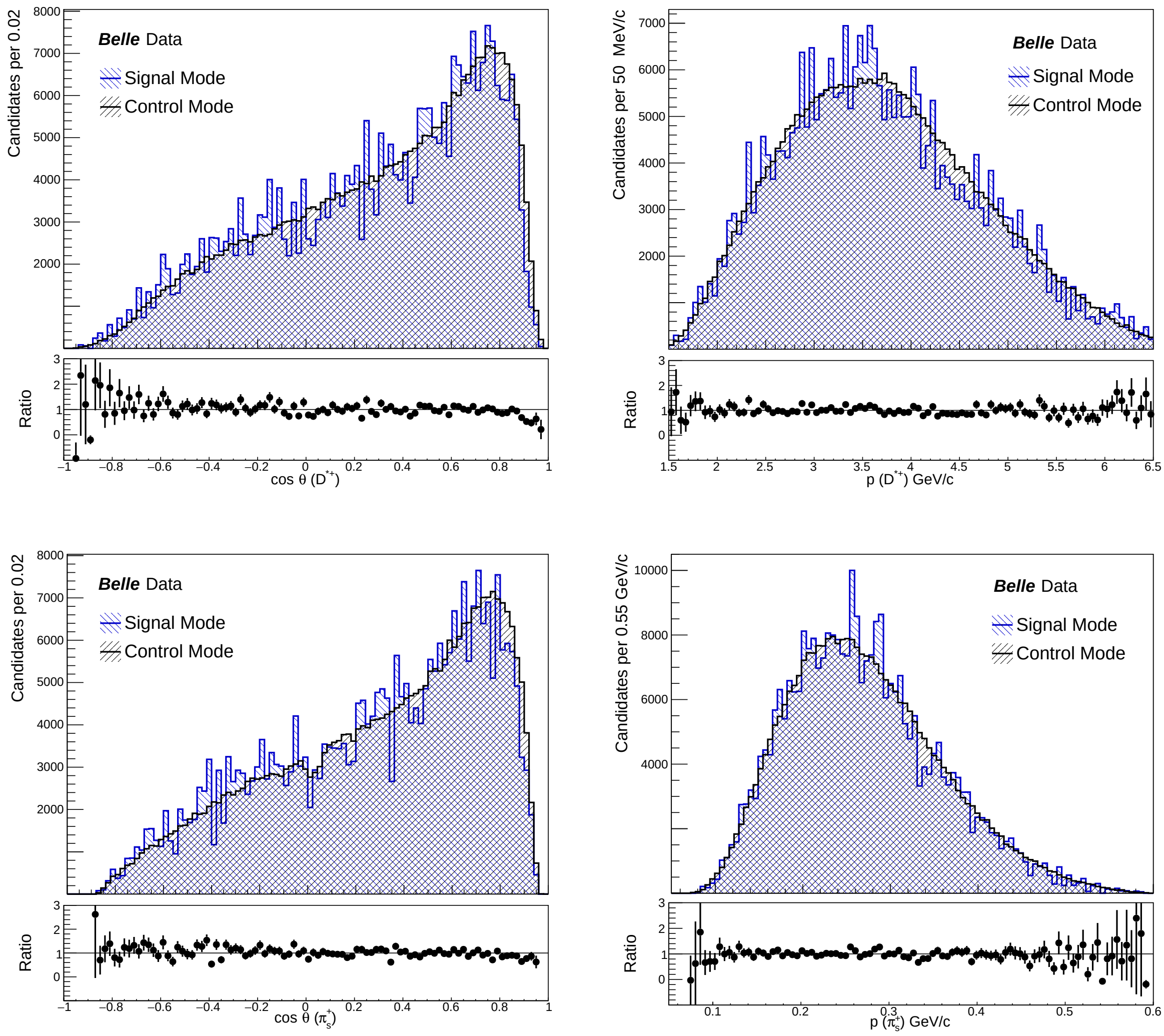

Figure 3.19: Normalized distributions of (top-left) $\cos\theta(D^{*+})$, (top-right) $p(D^{*+})$, (bottom-left) $\cos\theta(\pi_s)$ and (bottom-right) $p(\pi_s)$ of background-subtracted signal and control decays in Belle data. The ratio between the two samples are shown in the bottom panel of each plot.

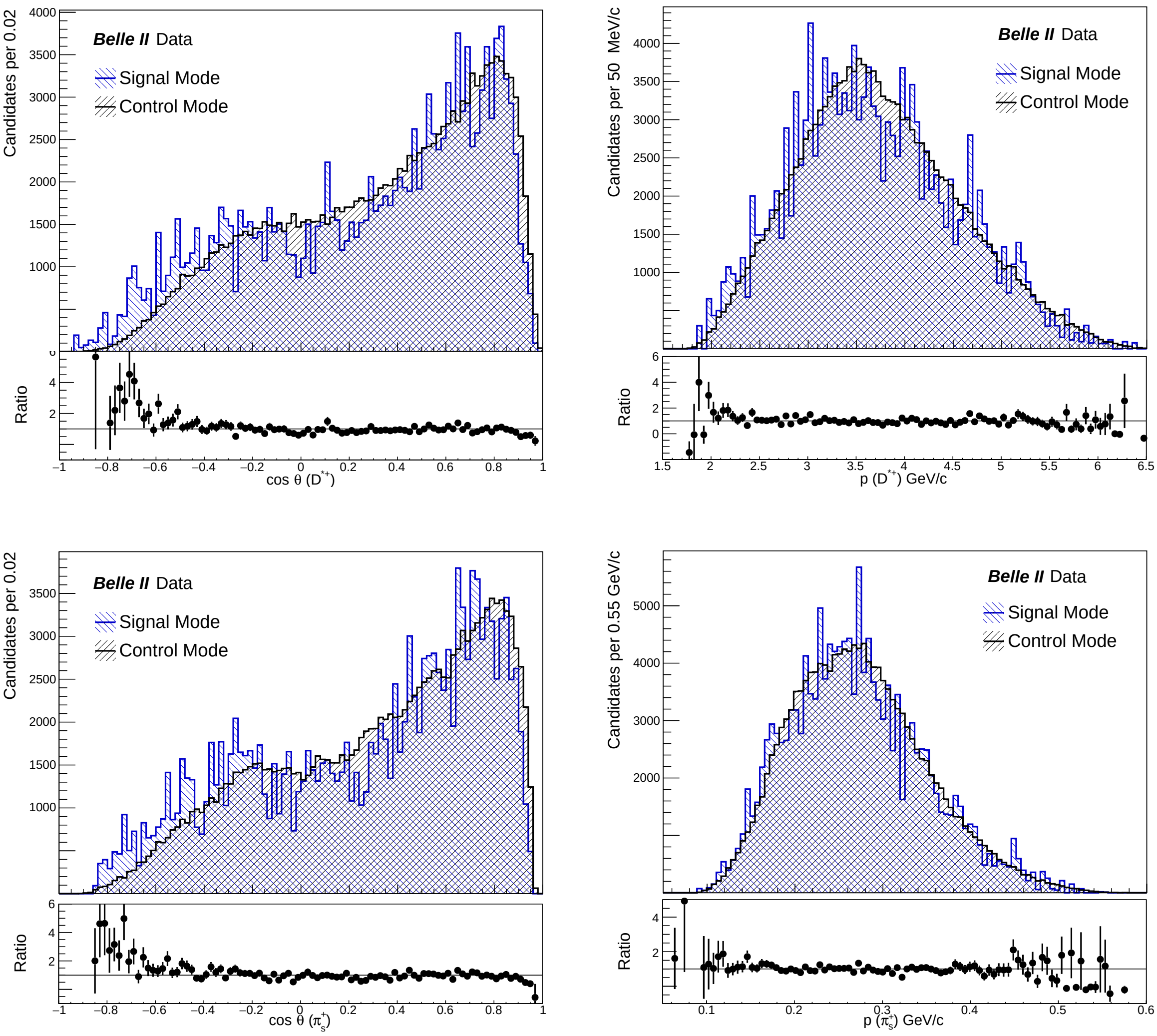

Figure 3.20: Normalized distributions of (top-left) $\cos\theta(D^{*+})$, (top-right) $p(D^{*+})$, (bottom-left) $\cos\theta(\pi_s)$ and (bottom-right) $p(\pi_s)$ of background-subtracted signal and control decays in Belle II data. The ratio between the two samples are shown in the bottom panel of each plot.

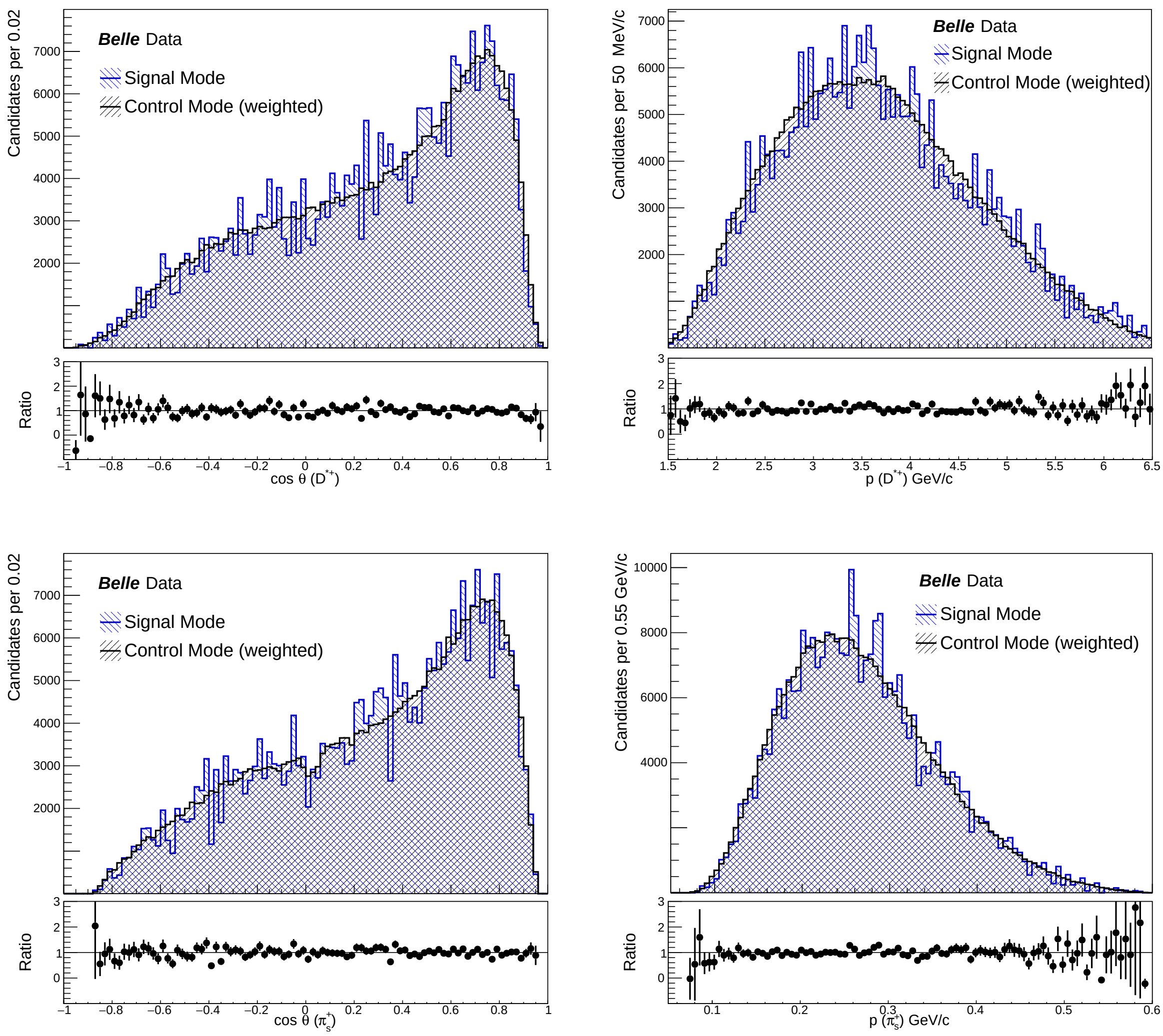

Figure 3.21: Normalized distributions of (top-left) $\cos\theta(D^{*+})$, (top-right) $p(D^{*+})$, (bottom-left) $\cos\theta(\pi_s)$ and (bottom-right) $p(\pi_s)$ of background-subtracted signal and control decays in Belle data. The control decays are weighted in $\cos\theta(D^{*+})$. The ratio between the two samples are shown in the bottom panel of each plot.

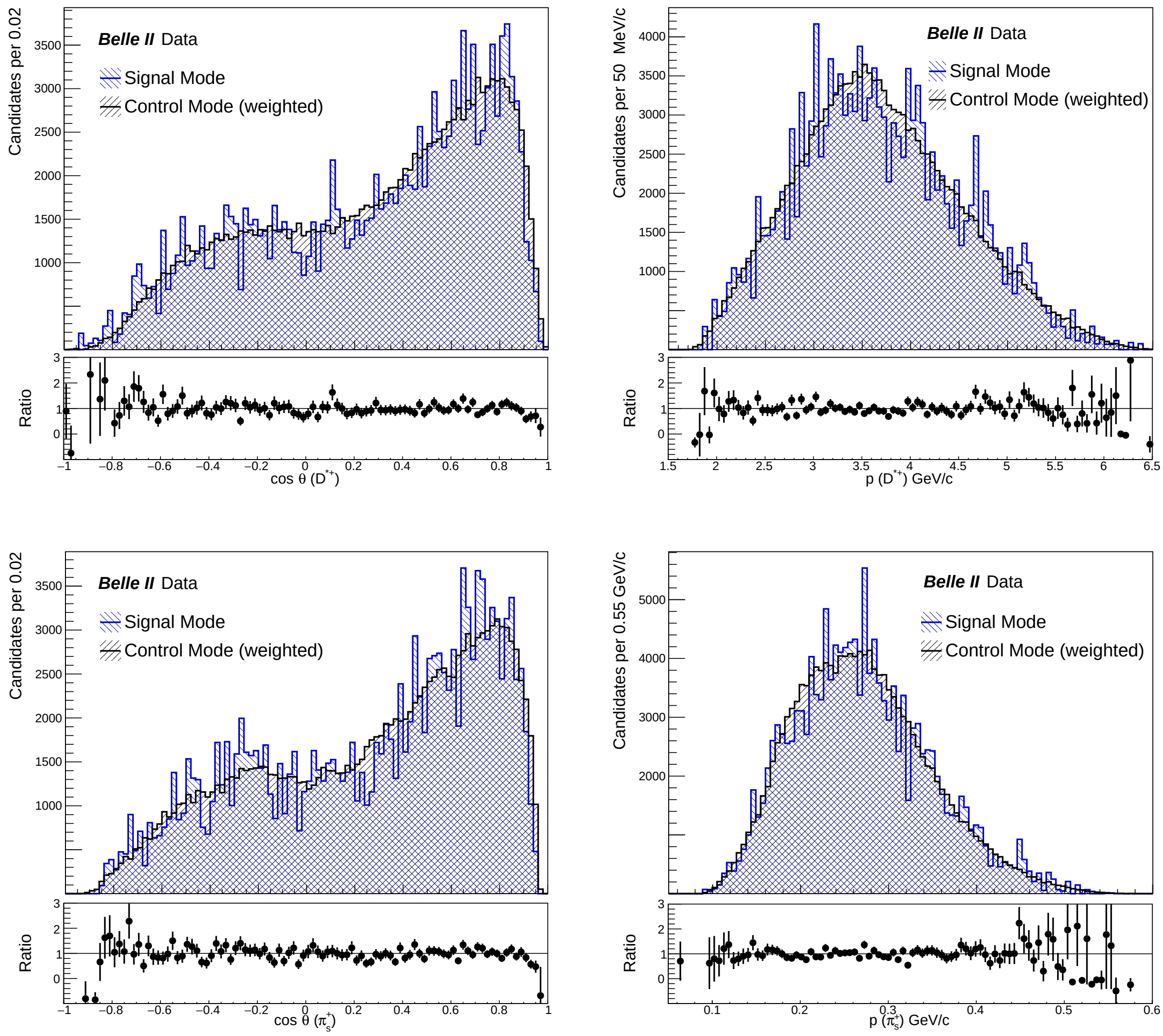

Figure 3.22: Normalized distributions of (top-left) $\cos\theta(D^{*+})$, (top-right) $p(D^{*+})$, (bottom-left) $\cos\theta(\pi_s)$ and (bottom-right) $p(\pi_s)$ of background-subtracted signal and control decays in Belle II data. The control decays are weighted in $\cos\theta(D^{*+})$. The ratio between the two samples are shown in the bottom panel of each plot.

3.4.3 Asymmetry fit

The raw asymmetry of the control decays is determined using an unbinned (and extended) fit to the two-dimensional $(m(K^+K^-), m(D^0\pi_s))$ distribution of D^0 and $\overline{D}^0$ candidates. The fit considers the $D^{*+} \to D^0(\to K^+K^-)\pi^+$ and all the background components discussed in the previous section. Simulation shows that 2D PDF of each component, except for the $D_s^+ \to K^+K^-\pi^+$ background, can be approximated into the product of the two 1D PDFs,

$$\mathrm{pdf}^i(m(K^+K^-), m(D^0\pi_s)) = \mathrm{pdf}^i(m(K^+K^-))\mathrm{pdf}^i(m(D^0\pi_s)) \qquad (i = K^+K^-, ...)\,, \tag{3.13}$$

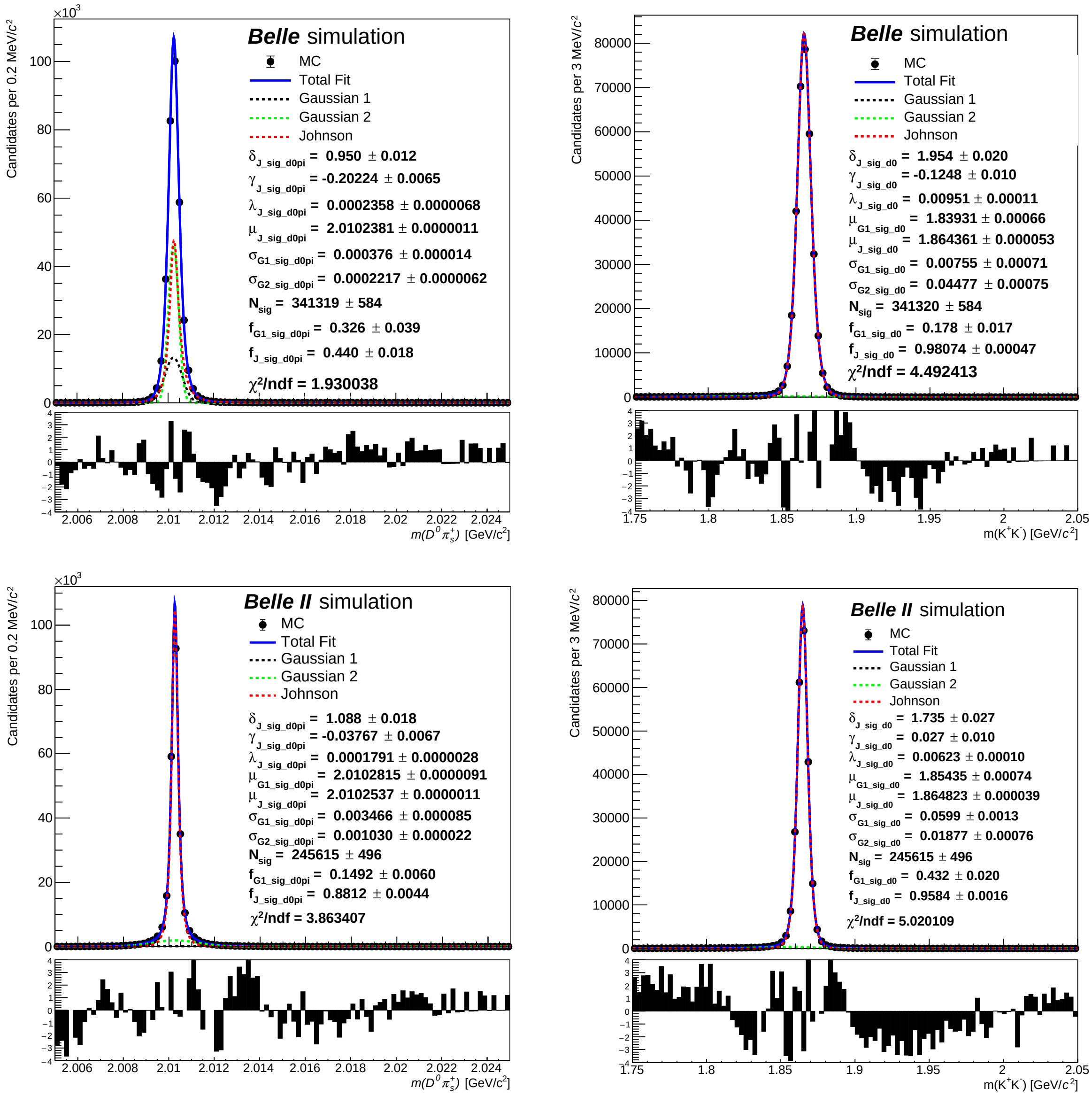

Figure 3.23: Distributions of (left) $m(D^0\pi_s)$ and (right) $m(K^+K^-)$ for truth-matched $D^{*+} \to D^0(\to K^+K^-)\pi^+$ decays in (top) Belle and (bottom) Belle II simulation, with fit projections overlaid. The normalized residuals (pulls) are shown in the bottom panel of each plot.

and that no substantial differences are observed between PDFs of D^0 and $\overline{D}^0$ decays, which are then assumed to be identical (Appendix B). Possible asymmetries in the PDFs shapes are tested in the systematic studies, as discussed in Section 4.1.2.

The control decays and physics backgrounds PDFs are determined in simulation using truth matching. The $m(K^+K^-)$ and $m(D^0\pi_s)$ PDFs of the $D^{*+} \to D^0(\to K^+K^-)\pi^+$ decays are each modelled using the sum of two Gaussian functions (with a common mean) and of a Johnson's S_U function (Figure 3.23),

$$\mathrm{pdf}^{K^+K^-}(m) = f_J\, J(m|\mu_J, \lambda_J, \delta_J, \gamma_J) + \\ + (1 - f_J)\left[f_{G1} G(m|\mu_{G1}, \sigma_{G1}) + (1 - f_{G1}) G(m|\mu_{G1}, \sigma_{G2})\right] , \quad (3.14)$$

with m being either $m(K^+K^-)$ or $m(D^0\pi_s)$.

The $m(K^+K^-)$ PDF of the mis-identified $D^{*+} \to D^0(\to K^-\pi^+)\pi^+$ background is parametrized using the sum of a Gaussian and a Johnson's S_U function, which is shown in Figure 3.24. Given that $m(D^0\pi_s)$ is unaffected by the mis-assigned mass hypothesis to the D^0 final state particles, the $m(D^0\pi_s)$ PDF is shared with that of the control decays.

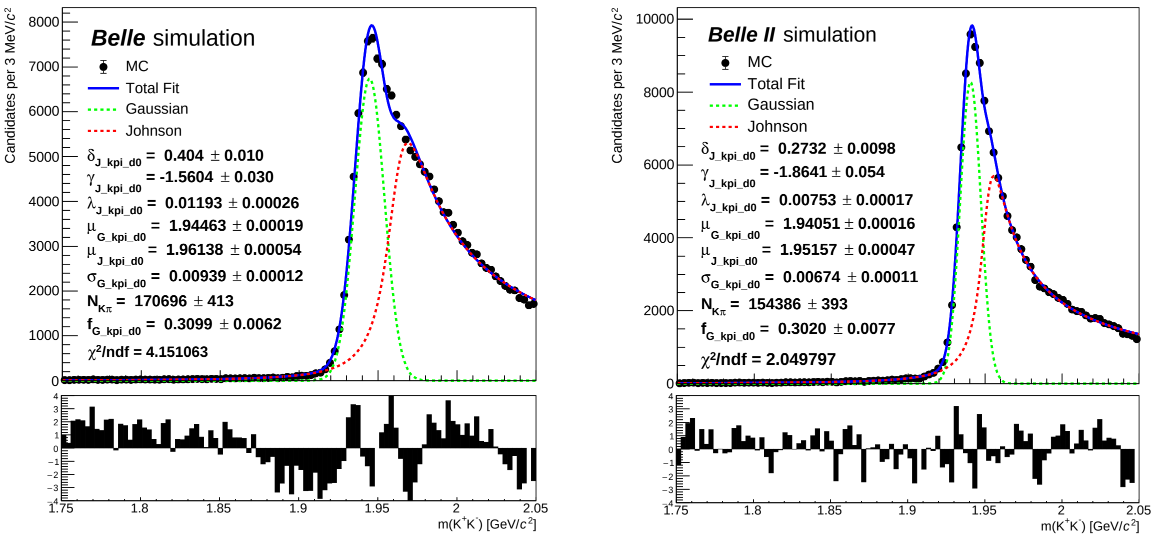

Figure 3.24: Distribution of $m(K^+K^-)$ for truth-matched $D^{*+} \to D^0(K^-\pi^+)\pi_s$ background decays in (left) Belle and (right) Belle II simulation, with fit projections overlaid. The normalized residuals (pulls) are shown in the bottom panel of each plot.

The partially reconstructed $D^{*+} \to D^0(\to \text{multibody})\pi^+$ decays are modeled as an exponential function in $m(K^+K^-)$ and as a Johnson's S_U function, with parameter γ_J fixed to unity, in $m(D^0\pi_s)$ (Figure 3.25).

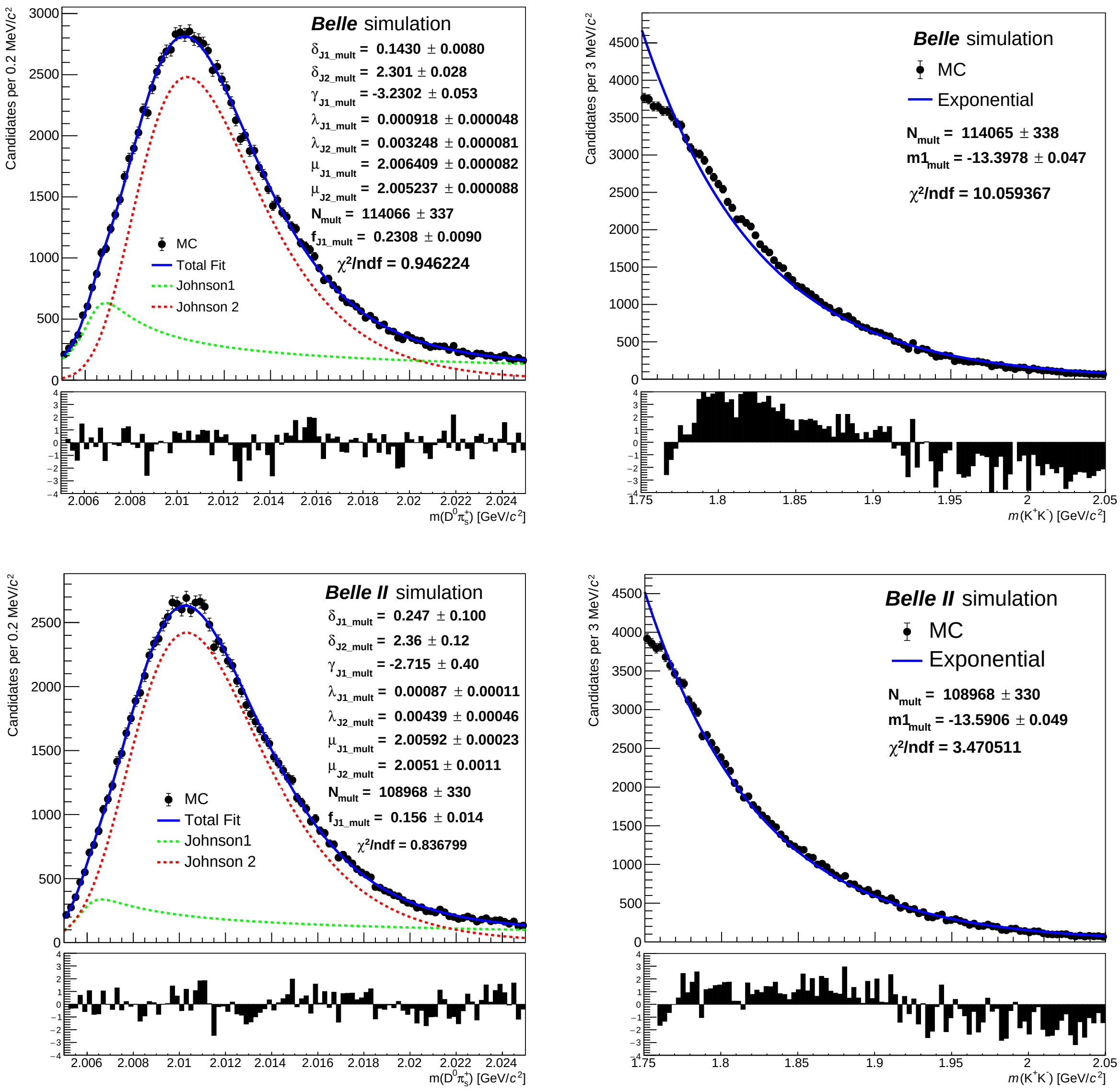

Figure 3.25: Distributions of (left) $m(D^0\pi_s)$ and (right) $m(K^+K^-)$ for truth-matched $D^{*+} \to D^0(\to \text{multibody})\pi^+$ decays in (top) Belle and (bottom) Belle II simulation, with fit projections overlaid. The normalized residuals (pulls) are shown in the bottom panel of each plot.

For each of the aforementioned components there is a corresponding one in which an unrelated soft pion is associated with the identified D^0 candidate. These random pions components (indicated as K^+K^- rnd, $K\pi$ rnd, and mult rnd) share the same $m(K^+K^-)$ distribution as the component with the correctly reconstructed soft pion and are modeled in $m(D^0\pi_s)$ with PDF derived directly from the fit to the data:

$$\text{pdf}^{i\,\text{rnd}}(m|m_0, A, B, C) = \left(1 - \exp\left(-\frac{m - m_0}{C}\right)\right) \cdot \left(\frac{m}{m_0}\right)^A + B\left(\frac{m}{m_0} - 1\right), \quad (3.15)$$

where $m = m(D^0\pi_s)$ and $m_0 = m_D^0 + m_\pi^+ = 2.00441\,\text{GeV}/c^2$ denotes the $m(D^0\pi_s)$ threshold.

The $D_s^+ \to K^+K^-\pi^+$ background in which the pion acts as the soft pion exhibits a kinematic correlation between $m(D^0\pi_s)$ and $m(K^+K^-)$, which can be calculated analytically as (Figure 3.26)

$$\big\langle m(K^+K^-)\big\rangle\,(m(D^0\pi_s)) = m_{D_s^+} + m_{D^0} - m(D^0\pi_s) = 3.83319\,\mathrm{GeV}/c^2 - m(D^0\pi_s)\,, \quad (3.16)$$

using the known D_s^+ and D^0 masses [23]. The two-dimensional PDF is written as the product of the $m(K^+K^-)$ PDF, conditional to the value of $m(D^0\pi_s)$, and of the $m(D^0\pi_s)$ PDF,

$$\mathrm{pdf}^{D_s^+}(m(K^+K^-), m(D^0\pi_s)) = \mathrm{pdf}^{D_s^+}(m(K^+K^-)|m(D^0\pi_s))\,\mathrm{pdf}^{D_s^+}(m(D^0\pi_s))\,. \quad (3.17)$$

The first term is parametrized as a Johnson's S_U function with mean parameter given by $\mu_J + \langle m(K^+K^-)\rangle\,(m(D^0\pi_s))$. An offset with respect to the analytical $\langle m(K^+K^-)\rangle$, μ_J, is used to account for possible data-simulation differences in the peak positions. The $m(D^0\pi_s)$ PDF is a first-order polynomial defined only about the threshold value of $m_D^0 + m_\pi^+$ [23]. The obtained distributions when fitting truth-matched decays are shown in Figure 3.27.

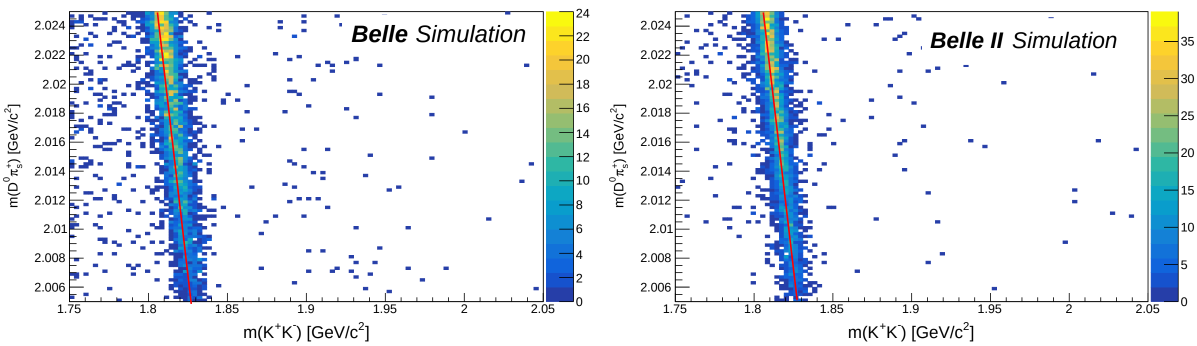

Figure 3.26: Distributions of $m(D^0\pi_s)$ versus $m(K^+K^-)$ for truth-matched $D_s^+ \to K^+K^-\pi^+$ decays in (left) Belle and (right) Belle II simulation. The red line denotes the analytical kinematic dependence of Equation (3.16).

Finally, the purely combinatorial background is described as a linear function in $m(K^+K^-)$ and as a random-pion background in $m(D^0\pi_s)$. The $m(D^0\pi_s)$ parametrization this component is shared with that of the other random-pion components. Omitting the arguments to simplify the notation, the total fit function is

$$\begin{aligned} f = {} & N^{K^+K^-}(1+qA_{\mathrm{raw}}^{K^+K^-})\,\mathrm{pdf}^{K^+K^-} + N^{K^+K^-\,\mathrm{rnd}}(1+qA_{\mathrm{raw}}^{K^+K^-\,\mathrm{rnd}})\,\mathrm{pdf}^{K^+K^-\,\mathrm{rnd}} \\ & + N^{K\pi}(1+qA_{\mathrm{raw}}^{K\pi})\,\mathrm{pdf}_{K\pi} + N^{K\pi\,\mathrm{rnd}}(1+qA_{\mathrm{raw}}^{K\pi\,\mathrm{rnd}})\,\mathrm{pdf}^{K\pi\,\mathrm{rnd}} \\ & + N^{\mathrm{mult}}(1+qA_{\mathrm{raw}}^{\mathrm{mult}})\,\mathrm{pdf}^{\mathrm{mult}} + N^{\mathrm{mult\ rnd}}(1+qA_{\mathrm{raw}}^{\mathrm{mult\ rnd}})\,\mathrm{pdf}^{\mathrm{mult\ rnd}} \\ & + N^{D_s^+}(1+qA_{\mathrm{raw}}^{D_s^+})\,\mathrm{pdf}^{D_s^+} + N^{\mathrm{comb}}(1+qA_{\mathrm{raw}}^{\mathrm{comb}})\,\mathrm{pdf}^{\mathrm{comb}} \end{aligned} \quad (3.18)$$

where $q = 1$ (-1) for D^0 $(\overline{D}^0)$ candidates and N^i and $A^i_{\rm raw}$ are, respectively, the total yield and the raw asymmetry of the component i. The parameters $c_{\rm comb}$, A and C are left free in the fit, together with the yields and asymmetries.

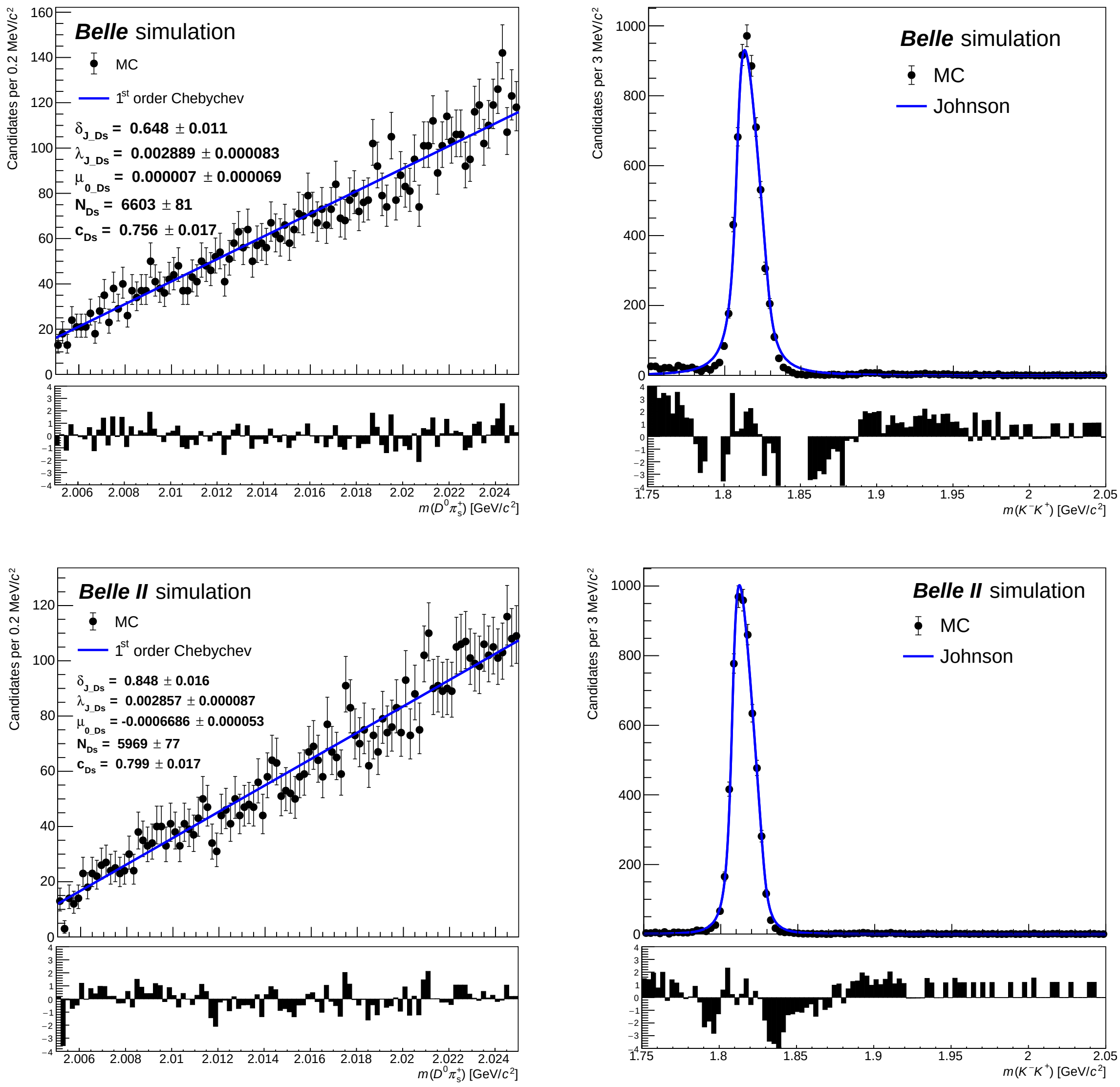

Figure 3.27: Distributions of (left) $m(D^0\pi_s)$ and (right) $m(K^+K^-)$ for truth-matched $D_s^+ \to K^+K^-\pi^+$ decays in (top) Belle and (bottom) Belle II simulation, with fit projections overlaid. The normalized residuals (pulls) are shown in the bottom panel of each plot.

To account for mismodeling of the simulation, when fitting the data the following six additional shape parameters are left free to float:

- the mean of the first Gaussian function used to model the $m(D^0\pi_s)$ distribution for the K^+K^- component ($\mu_{\rm G1\_sig\_d0pi}$, Figure 3.23);
- the width of the Johnson's S_U function used to model the $m(D^0\pi_s)$ distribution for the K^+K^- component ($\lambda_{\rm J\_sig\_d0pi}$, Figure 3.23);

- the width of the Johnson's S_U function used to model the $m(K^+K^-)$ distribution for the K^+K^- component ($\lambda_{\text{J\_sig\_d0}}$, Figure 3.23);
- the mean of the Gaussian function used to model the $m(K^+K^-)$ distribution for the $K\pi$ component ($\mu_{\text{G\_kpi\_d0}}$, Figure 3.24);
- the width of the Johnson's S_U function used to model the $m(K^+K^-)$ distribution for the $K\pi$ component ($\lambda_{\text{J\_kpi\_d0}}$, Figure 3.24);
- the tail parameter of the Johnson's S_U function used to model the $m(K^+K^-)$ distribution for the $K\pi$ component ($\gamma_{\text{J\_kpi\_d0}}$, Figure 3.24).

All other parameters are fixed to their values as determined on simulation.

3.4.4 Results on simulation

The results of the fits to the simulated events are shown in Figures 3.28 and 3.29. For Belle, we show the results on streams 0+10. The measured yields of $D^0 \to K^+K^-$ decays are 340374 ± 99 in Belle and 240771 ± 519 in Belle II, while from truth-matching we expect 341319 and 245615, respectively.

Fit parameter	Measured value	Raw asymmetry (%)
$N^{K^+K^-}$	340374 ± 599	0.00 ± 0.18
$N^{K^+K^-\,\text{rnd}}$	26010 ± 264	0.8 ± 1.0
$N^{K\pi}$	168417 ± 433	-1.39 ± 0.26
$N^{K\pi\,\text{rnd}}$	10558 ± 568	-5.4 ± 5.1
N^{mult}	79272 ± 853	1.26 ± 0.67
$N^{\text{mult rnd}}$	10762 ± 1650	-24 ± 11
$N^{D_s^+}$	7812 ± 224	-1.3 ± 2.8
N^{comb}	269690 ± 1868	0.46 ± 0.58
A	30.6 ± 1.6	–
C	0.002052 ± 0.0000045	–
c_{comb}	-0.34249 ± 0.0078	–

Table 3.7: Measured values of the parameters obtained from the fit to $D^0 \to K^+K^-$ sample in Belle simulation (streams 0+10). The uncertainties are statistical only.

The K^+K^- yields returned by the fit are underestimated by about 0.2% in Belle and by about 2.0% in Belle II, is not a surprise given the relatively poor fit quality and the difficulties to describe precisely the tails of the K^+K^- distributions. However, the corresponding raw asymmetries, $(0.00 \pm 0.18)\%$ and $(1.38 \pm 0.21)\%$, are in excellent agreement with the truth-matching values of -0.02% and 0.99%, respectively.

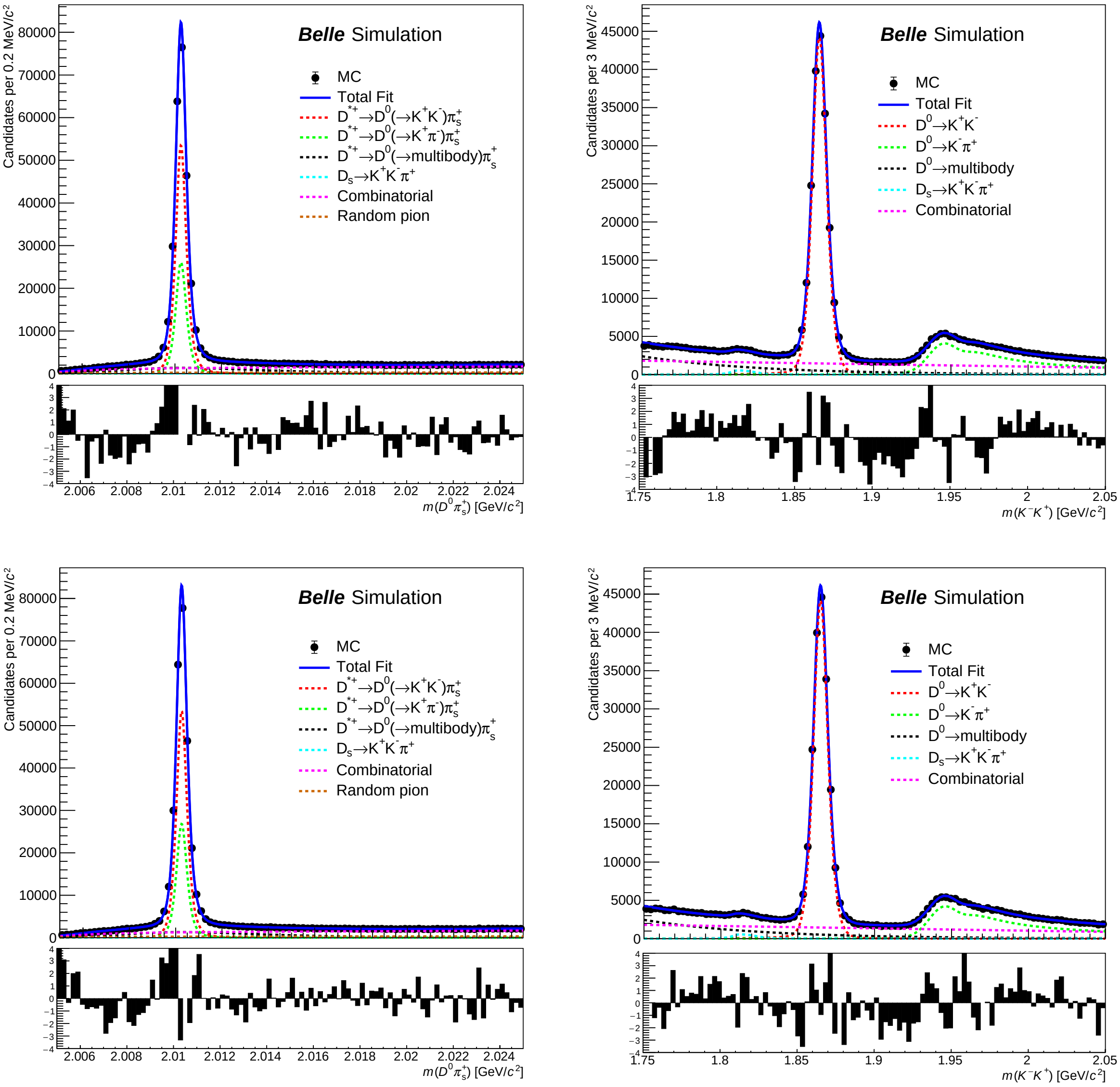

Figure 3.28: Distributions of (left) $m(D^0\pi_s)$ and (right) $m(K^+K^-)$ for (top) $D^{*+} \to D^0(\to K^+K^-)\pi^+$ and (bottom) $D^{*-} \to \overline{D}^0(\to K^+K^-)\pi^-$ in Belle simulation (streams 0+10), with fit projections overlaid. The normalized residuals (pulls) are also shown in the bottom panel of each plot.

In Section 4.1.2 we show that even with severe variations of the fit model, result in substantially worse fit quality, the estimation of the raw K^+K^- asymmetry is stable and has almost negligible systematic bias. The complete set of measured fit parameters are tabulated in Tables 3.7 and 3.8. Correlations coefficients are reported in Appendix A.

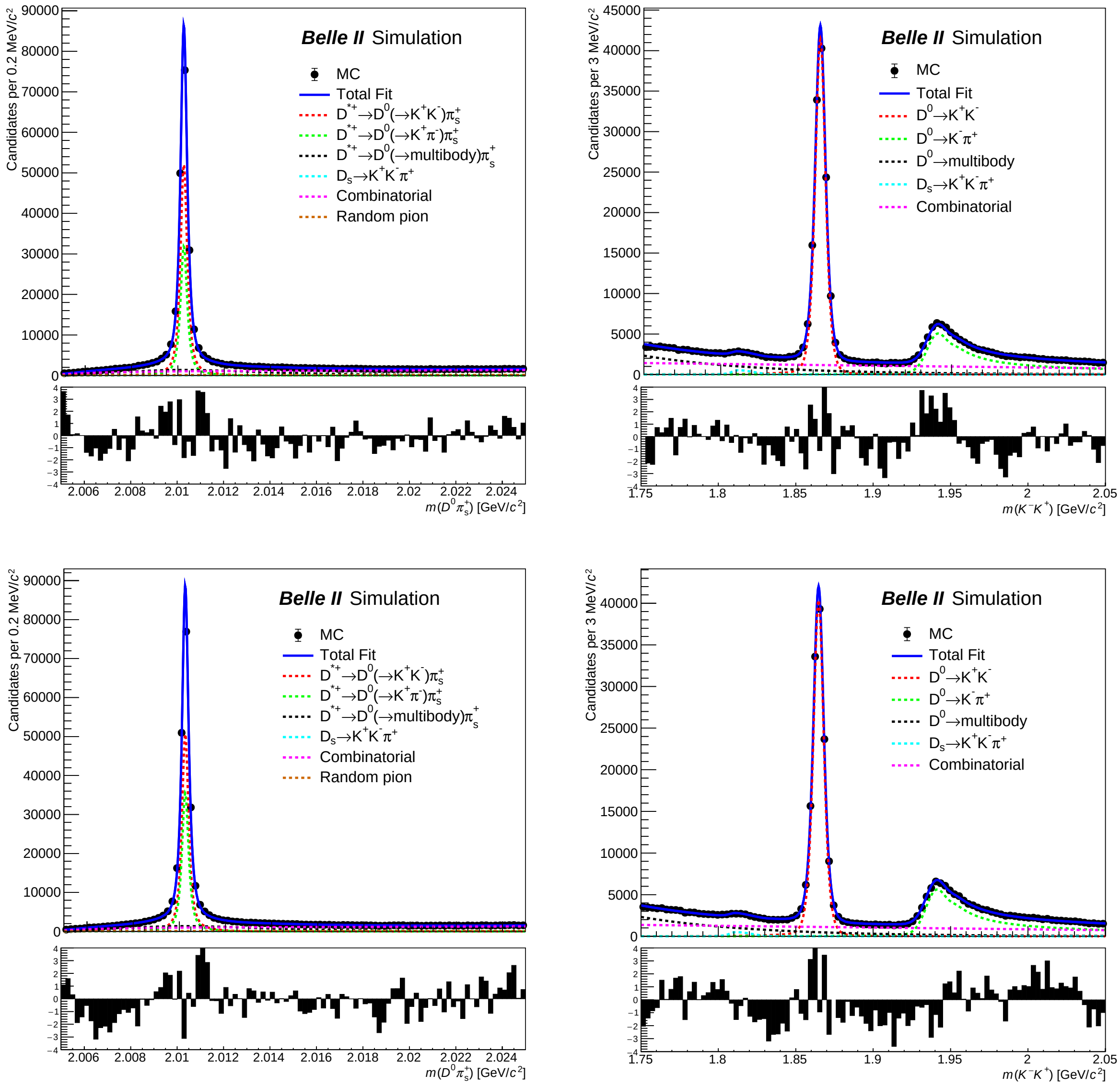

Figure 3.29: Distributions of (left) $m(D^0\pi_s)$ and (right) $m(K^+K^-)$ for (top) $D^{*+} \to D^0(\to K^+K^-)\pi^+$ and (bottom) $D^{*-} \to \overline{D}^0(\to K^+K^-)\pi^-$ in Belle II simulation, with fit projections overlaid. The normalized residuals (pulls) are also shown in the bottom panel of each plot.

Streams	$A_{\rm raw}^{K^+K^-}$ (%)
0+10	0.00 ± 0.18
1+11	-0.15 ± 0.18
2+12	-0.17 ± 0.18
3+13	-0.06 ± 0.18
4+14	0.26 ± 0.18
5+15	-0.27 ± 0.18

Table 3.9: Measured values of $A_{\rm raw}^{K^+K^-}$ from fits to samples corresponding to different $980\,{\rm fb}^{-1}$ streams of the Belle simulation. The uncertainties are statistical only.

Fit parameter	Measured value	Raw asymmetry (%)
$N^{K^+K^-}$	240771 ± 520	1.38 ± 0.21
$N^{K^+K^- \text{ rnd}}$	13975 ± 214	-0.5 ± 1.5
$N^{K\pi}$	157910 ± 445	-5.45 ± 0.28
$N^{K\pi \text{ rnd}}$	7636 ± 394	0.2 ± 4.8
N^{mult}	112116 ± 824	0.02 ± 0.55
$N^{\text{mult rnd}}$	0 (fixed)	0 (fixed)
$N^{D_s^+}$	6097 ± 172	2.6 ± 2.7
N^{comb}	213737 ± 1043	1.81 ± 0.42
A	28.3 ± 2.2	-
C	0.002041 ± 0.000065	-
c_{comb}	-0.30038 ± 0.0060	-

Table 3.8: Measured values of the parameters obtained from the fit to $D^0 \to K^+K^-$ sample in Belle II simulation. The uncertainties are statistical only. The yield of the "mult rnd" component is measured to be consistent with zero and therefore its value and its asymmetry are fixed to zero.

To complete the validation we perform the fit using all the available streams of Belle MC, each corresponding to an integrated luminosity of $980\,\text{fb}^{-1}$. The measured values of A_{raw}, shown in Table 3.9, are all in agreement with each other and with the truth-matching asymmetry. Similarly, we perform fits to three subsets of the Belle II simulation, each corresponding to an integrated luminosity of $400\,\text{fb}^{-1}$. The measured A_{raw} values are in agreement and are shown in Table 3.10.

Streams	$A_{\text{raw}}^{K^+K^-}$ (%)
1	1.35 ± 0.26
2	1.01 ± 0.26
3	1.39 ± 0.26

Table 3.10: Measured values of $A_{\text{raw}}^{K^+K^-}$ from fits to samples corresponding to $400\,\text{fb}^{-1}$ subsets of the Belle II simulation. The uncertainties are statistical only.

3.4.5 Results on data

The results of the fits to the data are shown in Figures 3.30 and 3.31. The measured K^+K^- yields are 308755 ± 574 in Belle and 145515 ± 405 in Belle II. The yields per $1\,\text{fb}^{-1}$ of unit luminosity are 315.0 ± 0.6 for Belle and 346 ± 1 for Belle II. The K^+K^- raw asymmetry is measured to be $0.17 \pm 0.19\%$ in Belle and $(1.61 \pm 0.27)\%$ in Belle II. The complete set of measured fit parameters are tabulated in Tables 3.11 and 3.12. Correlations coefficients are reported in Appendix A.

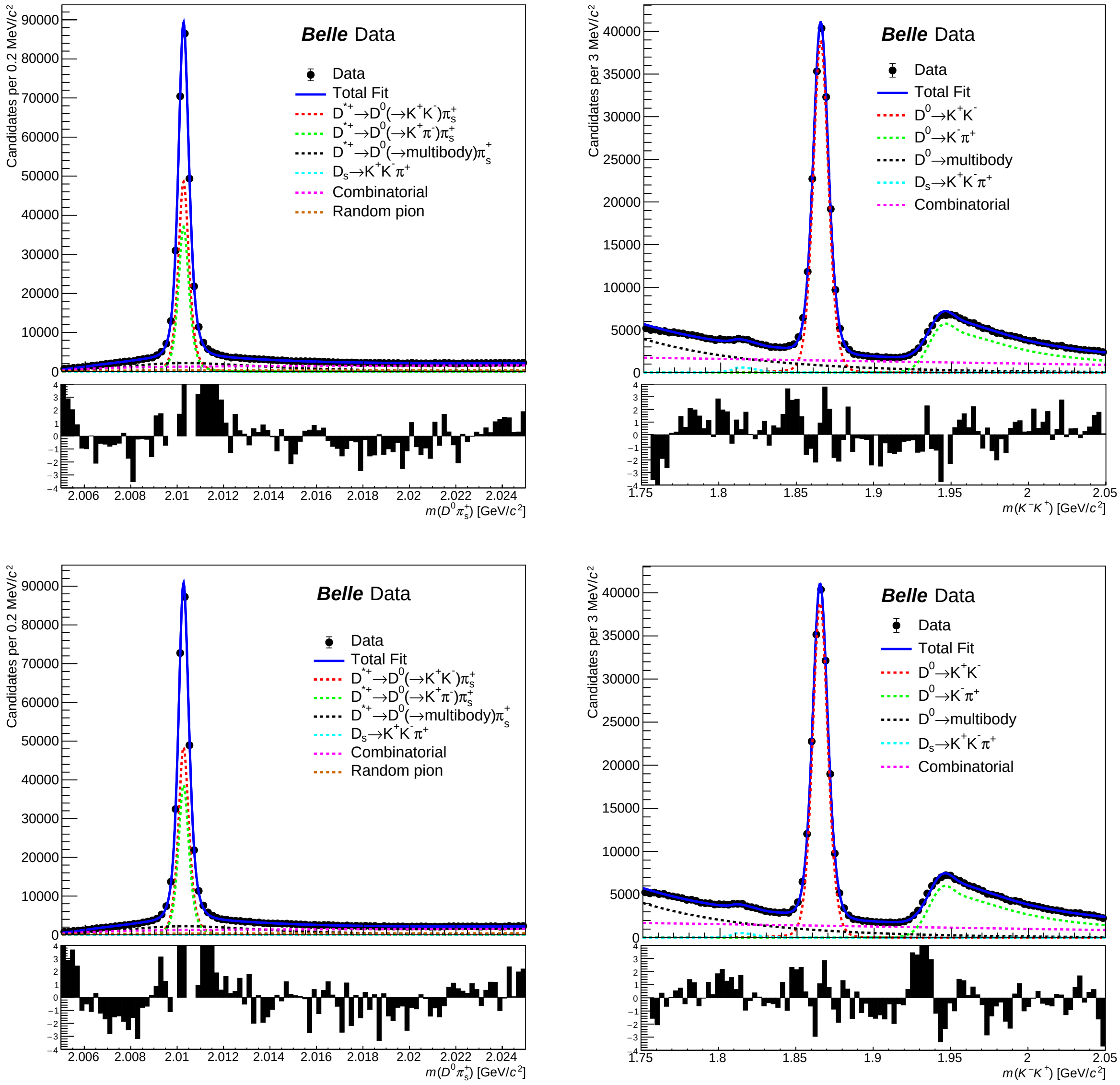

Figure 3.30: Distributions of (left) $m(D^0\pi_s)$ and (right) $m(K^+K^-)$ for (top) $D^{*+} \to D^0(\to K^+K^-)\pi^+$ and (bottom) $D^{*-} \to \overline{D}^0(\to K^+K^-)\pi^-$ in Belle data, with fit projections overlaid. The normalized residuals (pulls) are also shown in the bottom panel of each plot.

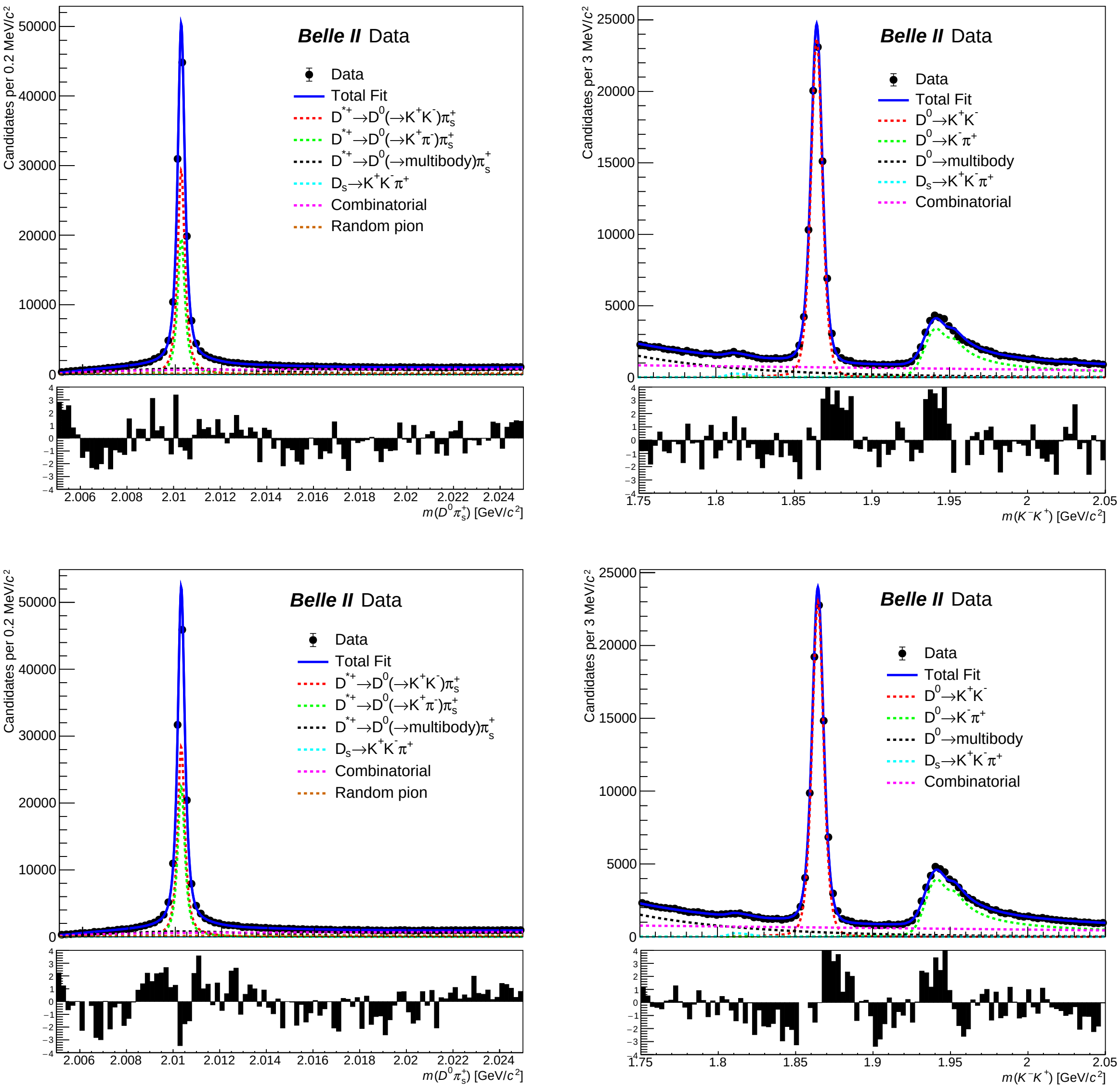

Figure 3.31: Distributions of (left) $m(D^0\pi_s)$ and (right) $m(K^+K^-)$ for (top) $D^{*+} \rightarrow D^0(\rightarrow K^+K^-)\pi^+$ and (bottom) $D^{*-} \rightarrow \overline{D}^0(\rightarrow K^+K^-)\pi^-$ in Belle II data, with fit projections overlaid. The normalized residuals (pulls) are also shown in the bottom panel of each plot.

Fit parameter	Measured value	Raw asymmetry (%)
$N^{K^+K^-}$	308755 ± 574	0.17 ± 0.19
$N^{K^+K^-\,\mathrm{rnd}}$	29538 ± 287	1.30 ± 0.94
$N^{K\pi}$	240856 ± 518	-2.16 ± 0.21
$N^{K\pi\,\mathrm{rnd}}$	18212 ± 622	-4.7 ± 3.1
N^{mult}	178096 ± 1127	-0.77 ± 0.46
$N^{\mathrm{mult\ rnd}}$	16366 ± 1934	6.93 ± 7.3
$N^{D_s^+}$	8046 ± 235	4.6 ± 2.9
N^{comb}	261850 ± 2098	0.76 ± 0.61
A	20.8 ± 1.9	-
C	0.002234 ± 0.000055	-
c_{comb}	-0.31541 ± 0.0092	-
$\mu_{\mathrm{J\_sig\_d0pi}}$	$2.01021658 \pm 0.000000089$	-
$\mu_{\mathrm{J\_sig\_d0}}$	1.864432 ± 0.000010	-
$\lambda_{\mathrm{J\_sig\_d0}}$	0.01146 ± 0.000015	-
$\delta_{\mathrm{J\_sig\_d0}}$	2.239 ± 0.026	-
$\mu_{\mathrm{J\_kpi\_d0}}$	1.95683 ± 0.00025	-
$\delta_{\mathrm{J\_kpi\_d0}}$	0.599 ± 0.011	-

Table 3.11: Measured values of the parameters obtained from the fit to $D^0 \to K^+K^-$ sample in Belle data. The uncertainties are statistical only.

Fit parameter	Measured value	Raw asymmetry (%)
$N^{K^+K^-}$	145515 ± 405	1.61 ± 0.27
$N^{K^+K^-\,\mathrm{rnd}}$	12727 ± 193	-0.9 ± 1.4
$N^{K\pi}$	105715 ± 363	-6.91 ± 0.34
$N^{K\pi\,\mathrm{rnd}}$	8717 ± 318	-11.0 ± 3.9
N^{mult}	66976 ± 731	1.06 ± 0.80
$N^{\mathrm{mult\ rnd}}$	5980 ± 1163	16 ± 11
$N^{D_s^+}$	3011 ± 130	3.2 ± 4.2
N^{comb}	126233 ± 1306	4.55 ± 0.74
A	18.6 ± 3.3	-
C	0.002431 ± 0.000096	-
c_{comb}	-0.2715 ± 0.012	-
$\mu_{\mathrm{G1\_sig\_d0pi}}$	2.010486 ± 0.000012	-
$\lambda_{\mathrm{J\_sig\_d0pi}}$	$0.00019695 \pm 0.00000054$	-
$\lambda_{\mathrm{J\_sig\_d0}}$	0.006781 ± 0.000018	-
$\mu_{\mathrm{G\_kpi\_d0}}$	1.940420 ± 0.000056	-
$\lambda_{\mathrm{J\_kpi\_d0}}$	0.006147 ± 0.000097	-
$\gamma_{\mathrm{J\_kpi\_d0}}$	-1.7399 ± 0.013	-

Table 3.12: Measured values of the parameters obtained from the fit to $D^0 \to K^+K^-$ sample in Belle II data. The uncertainties are statistical only.

Chapter 4

Evaluation of systematic uncertainties and final results

4.1 Sources of systematic uncertainties

Various sources of systematic uncertainties are considered, namely: PDF modeling in the $D^0 \to K_S^0 K_S^0$ fit, PDF modeling in the $D^0 \to K^+K^-$ fit, equalization of the control and signal sample kinematic for the cancellation of the nuisance asymmetries, uncertainties on the external input value of $\mathcal{A}_{CP}(D^0 \to K^+K^-)$. A summary of the estimated uncertainties from the aforementioned sourced is reported in Table 4.1, the total is the sum in quadrature of the individual components.

Source	Uncertainty (%)	
	Belle	Belle II
Modeling in the $D^0 \to K_S^0 K_S^0$ fit	0.04	0.05
Modeling in the $D^0 \to K^+K^-$ fit	0.02	< 0.01
Kinematic equalization	0.06	0.07
Input $\mathcal{A}_{CP}(D^0 \to K^+K^-)$	0.05	0.05
Total systematical	0.09	0.10
Total statistical	1.60	2.30

Table 4.1: Summary of uncertainties on $\mathcal{A}_{CP}(D^0 \to K_S^0 K_S^0)$. The statistical uncertainty includes contributions from both the signal and the control mode, with the latter being essentially negligible.

4.1.1 Modeling in the $D^0 \to K_S^0 K_S^0$ fit

To estimate the systematic uncertainty due to the fit model for $D^0 \to K_S^0 K_S^0$, several variations of the default fit model are carried out. We test two classes of variations: one in which we vary the PDF model, while still keeping it the same for D^0 and $\overline{D}^0$ candidates (Table 4.2), and another in which we keep the default PDF model but introduce an asymmetry in one of the shape parameters (Table 4.3). From the first set of tests we take the largest variations in $A_{\mathrm{raw}}^{K_S^0 K_S^0}$, 0.04% for Belle and 0.05% for Belle II, as systematic uncertainties. From the second set of tests we observe no significant differences between D^0 and $\overline{D}^0$ shapes and hence assign no additional systematic uncertainty due to this assumption in the default fit.

Model variation		Belle		Belle II	
#	Description	$\Delta A_{\mathrm{raw}}^{K_S^0 K_S^0}$ (%)	$-2\Delta \log L$	$\Delta A_{\mathrm{raw}}^{K_S^0 K_S^0}$ (%)	$-2\Delta \log L$
1	Signal model for Δm is identical to $K_S^0\pi\pi$ model for Δm	-0.04	4	0.05	4
2	$K_S^0\pi\pi$ model for Δm is identical to signal model for Δm	-0.02	82	0.00	34
3	Bkg model for Δm changed to Equation (3.15)	0.02	28	0.05	12
4	Bkg model for γ changed to Johnson's S_U + Gaussian	0.02	58	0.03	30
5	Variations 3 + 4	0.01	86	-0.01	12
6	Signal model for γ changed to histogram PDF	0.04	-6	0.03	-1

Table 4.2: Systematic variation of the PDF model for the $D^0 \to K_S^0 K_S^0$ fit. The table reports the change in A_{raw} and in $-2\log L$ for the varied model compared to the default. The PDFs are assumed to be the same for D^0 and $\overline{D}^0$ candidates.

Model variation		Belle			Belle II		
#	Asymmetric parameter introduced	Fitted parameter asymmetry	$\Delta A_{\mathrm{raw}}^{K_S^0 K_S^0}$ (%)	$-2\Delta \log L$	Fitted parameter asymmetry	$\Delta A_{\mathrm{raw}}^{K_S^0 K_S^0}$ (%)	$-2\Delta \log L$
1	Mean of the Johnson for Δm signal PDF	$(1.9 \pm 3.9) \times 10^{-5}$	0.00	0	$(-1.7 \pm 3.8) \times 10^{-5}$	0.00	0
2	Width of the Johnson for Δm signal PDF	$(-4.5 \pm 1.8)\%$	0.47	-6	$(5.4 \pm 2.9)\%$	-0.50	-4
3	Mean of the Johnson for γ signal PDF	$(-1.1 \pm 1.9) \times 10^{-3}$	-0.12	0	$(1.3 \pm 2.3) \times 10^{-3}$	0.00	0
4	Width of the Johnson for γ signal PDF	$(-3.6 \pm 9.9) \times 10^{-3}$	0.18	0	$(-1.0 \pm 1.3) \times 10^{-3}$	0.00	0
5	Mean of the Johnson for Δm $K_S^0\pi\pi$ PDF	$(3.7 \pm 1.8) \times 10^{-5}$	0.00	-4	$(0.6 \pm 2.3) \times 10^{-3}$	0.00	0
6	Width of the Johnson for Δm $K_S^0\pi\pi$ PDF	$(1.4 \pm 1.0)\%$	-0.01	-2	$(1.0 \pm 2.5)\%$	0.00	0
7	Mean of the Johnson for γ $K_S^0\pi\pi$ PDF	$(4.3 \pm 4.3) \times 10^{-3}$	-0.20	-2	$(1.8 \pm 6.4) \times 10^{-3}$	-0.05	0
8	Width of the Johnson for γ $K_S^0\pi\pi$ PDF	$(0.0 \pm 7.2) \times 10^{-3}$	0.00	0	$(1.13 \pm 0.97)\%$	-0.01	-2
9	Mean of the left-side Johnson for γ bkg PDF	$(-1.6 \pm 5.5) \times 10^{-3}$	0.00	0	$(0.3 \pm 4.8) \times 10^{-3}$	0.00	0
10	Width of the left-side Johnson for γ bkg PDF	$(7.5 \pm 7.7) \times 10^{-3}$	0.00	-2	$(9.8 \pm 5.1) \times 10^{-4}$	0.00	0
11	Mean of the right-side Johnson for γ bkg PDF	$(0.7 \pm 2.6) \times 10^{-3}$	0.00	-2	$(2.2 \pm 4.4) \times 10^{-3}$	0.00	0
12	Width of the right-side Johnson for γ bkg PDF	$(-4.7 \pm 9.7) \times 10^{-3}$	0.04	-2	$(-0.2 \pm 3.5) \times 10^{-3}$	0.00	0

Table 4.3: Systematic variation of the PDF model for the $D^0 \to K_S^0 K_S^0$ fit. The table reports the change in A_{raw} and in $-2\log L$ for the varied model compared to the default. The PDFs are the same as the default fit, but they are not assumed to be the same for D^0 and $\overline{D}^0$ candidates by introducing an asymmetric parameter, whose value is also reported.

4.1.2 Modeling in the $D^0 \to K^+K^-$ fit

As for the signal mode, we test two classes of variations for the $D^0 \to K^+K^-$ model: one in which we vary the PDF model, while still keeping it the same for D^0 and $\overline{D}^0$ candidates (Table 4.4), and another in which we keep the default PDF model but introduce an asymmetry in one of the shape parameters (Table 4.5). From the first set of tests, the largest variation in $A_{\mathrm{raw}}^{K^+K^-}$ is 0.02% for Belle and $< 0.01\%$ for Belle II. These values are assigned as systematic uncertainties. From the second set of tests, we observe no significant differences between D^0 and $\overline{D}^0$ shapes and hence assign no additional systematic uncertainty due to this assumption in the default fit.

Model variation		Belle		Belle II	
#	Description	$\Delta A_{\mathrm{raw}}^{K^+K^-}$ (%)	$-2\Delta\log L$	$\Delta A_{\mathrm{raw}}^{K^+K^-}$ (%)	$-2\Delta\log L$
1	Multibody model for $m(D^0\pi_s)$ changed to Johnson's S_U	0.00	0	0.00	3320
2	K^+K^- models for $m(D^0\pi_s)$ and $m(K^+K^-)$ changed to double Johnson's S_U based on simulation	0.01	35900	0.00	3460
3	Comb. and random-pion model for $m(D^0\pi_s)$ changed to Equation (3.9)	0.00	2	0.00	220
4	Variation 2 + 3	0.01	35900	0.00	4220
5	Multibody model for $m(K^+K^-)$ changed to histogram PDF	0.00	−4200	0.00	30

Table 4.4: Systematic variation of the PDF model for the $D^0 \to K^+K^-$ fit. The table reports the change in A_{raw} and in $-2\log L$ for the varied model compared to the default. The PDFs are assumed to be the same for D^0 and $\overline{D}^0$ candidates.

Model variation		Belle			Belle II		
#	Asymmetric parameter introduced	Fitted parameter asymmetry	$\Delta A_{\mathrm{raw}}^{K^+K^-}$ (%)	$-2\Delta\log L$	Fitted parameter asymmetry	$\Delta A_{\mathrm{raw}}^{K^+K^-}$ (%)	$-2\Delta\log L$
1	Mean of the Johnson for $m(D^0\pi_s)$ signal PDF	$(0.2\pm3.1)\times10^{-5}$	0.00	0	$(4.9\pm2.3)\times10^{-7}$	0.00	0
2	Width of the Johnson for $m(D^0\pi_s)$ signal PDF	$(-0.9\pm2.8)\times10^{-3}$	0.01	0	$(1.2\pm2.5)\times10^{-3}$	0.06	0
3	Mean of the Gaussians for $m(D^0\pi_s)$ signal PDF	$(3.3\pm4.7)\times10^{-6}$	0.01	0	$(12.0\pm5.6)\times10^{-7}$	−0.01	0
4	Mean of the Johnson for $m(K^+K^-)$ signal PDF	$(5.4\pm5.4)\times10^{-6}$	0.00	0	$(-13.0\pm6.2)\times10^{-4}$	0.02	0
5	Width of the Johnson for $m(K^+K^-)$ signal PDF	$(0.0\pm1.6)\times10^{-3}$	0.00	0	$(2.3\pm2.6)\times10^{-3}$	−0.01	0
6	Mean of the Gaussians for $m(K^+K^-)$ signal PDF	$(4.8\pm4.2)\times10^{-4}$	0.01	0	$(4.3\pm4.4)\times10^{-4}$	−0.04	0

Table 4.5: Systematic variation of the PDF model for the $D^0 \to K^+K^-$ fit. The table reports the change in A_{raw} and in $-2\log L$ for the varied model compared to the default. The PDFs are the same as the default fit, but they are not assumed to be the same for D^0 and $\overline{D}^0$ candidates by introducing an asymmetric parameter, whose value is also reported.

4.1.3 Kinematic equalization

The kinematic weighting of the $D^0 \to K^+K^-$ control sample does not perfectly remove all differences observed in the D^{*+} and π_s momentum and polar angle distributions. The residual differences are approximately a factor two smaller than those observed before the weighting. We therefore take half the variation in $A_{\mathrm{raw}}^{K^+K^-}$ introduced by the weighting procedure, 0.06% in Belle and 0.07% in Belle II, as a systematic uncertainty.

4.1.4 Input $\mathcal{A}_{CP}(D^0 \to K^+K^-)$

The *CP* asymmetry in $D^0 \to K_S^0 K_S^0$ decays can be determined as

$$\mathcal{A}_{CP}(D^0 \to K_S^0 K_S^0) = A_{\mathrm{raw}}^{K_S^0 K_S^0} - A_{\mathrm{raw}}^{K^+K^-} + \mathcal{A}_{CP}(D^0 \to K^+K^-)\,, \tag{4.1}$$

where $\mathcal{A}_{CP}(D^0 \to K^+K^-)$ is an external input. In particular, $\mathcal{A}_{CP}(D^0 \to K^+K^-)$ computed from the results reported in Refs. [25, 53] and [54] are used.

$$\mathcal{A}_{CP}(D^0 \to K^+K^-) = \mathcal{A}_{CP}^{\mathrm{dir}}(D^0 \to K^+K^-) + \Delta Y = (6.7 \pm 5.4)\times 10^{-4}\,, \tag{4.2}$$

where $\mathcal{A}_{CP}^{\mathrm{dir}}$ is the direct *CP* asymmetry and ΔY ($\approx -A_\Gamma$) is the asymmetry arising from *CP* violation in mixing and in the interference between mixing and decay [25]. The uncertainty in the input value of $\mathcal{A}_{CP}(D^0 \to K^+K^-)$ (Equation (4.2)) is propagated as a systematic uncertainty on the measurement.

4.2 Results and summary

Using D^{*+}-tagged $D^0 \to K_S^0 K_S^0$ and $D^0 \to K^+K^-$ decays reconstructed with an integrated luminosity $980\,\text{fb}^{-1}$ of Belle data, and $420\,\text{fb}^{-1}$ of Belle II data, we measure the time-integrated *CP* asymmetry in $D^0 \to K_S^0 K_S^0$ decays, following Equation (3.4), to be

$$\mathcal{A}_{CP}(D^0 \to K_S^0 K_S^0) = (1.2 \pm 1.6(\text{stat}) \pm 0.1(\text{syst}))\% \text{ (blind)} \tag{4.3}$$

$$\mathcal{A}_{CP}(D^0 \to K_S^0 K_S^0) = (1.6 \pm 2.3(\text{stat}) \pm 0.1(\text{syst}))\% \text{ (blind)} \tag{4.4}$$

respectively. The two results are in agreement with each other and with previous determinations [50]. The Belle result has a statistical precision slightly worse than the published measurement (1.6% compared to 1.5%) [51]. This is exclusively due to the tighter criteria on $p_{\text{cms}}(D^{*+})$ used in this analysis ($2.5\,\text{GeV}/c$ compared to $2.2\,\text{GeV}/c$). Releasing the $p_{\text{cms}}(D^{*+})$ requirement would not effectively change the final precision, as discussed in Appendix C, and the tighter requirement is justified by the need to suppress contamination from B decays to a negligible level. Our Belle results has, however, a factor-two better systematic uncertainty compared to the published result thanks to the usage of the $D^0 \to K^+K^-$ control mode, which provides a more precise $\mathcal{A}_{CP}$ external input compared to the $D^0 \to K_S^0\pi^0$ control mode used in Ref. [51].

Considering that the only source of correlation between the two results is the external input value of $\mathcal{A}_{CP}(D^0 \to K^+K^-)$, a combination of our Belle and Belle II results is performed to yield

$$\mathcal{A}_{CP}(D^0 \to K_S^0 K_S^0) = (1.3 \pm 1.3(\text{stat}) \pm 0.1(\text{syst}))\% \text{ (blind)}\,. \tag{4.5}$$

This result is $\approx 14\%$ more precise than the previous Belle measurement and is competitive with the world-best measurement from LHCb [52].

4.3 Future scope

Future task for the analysis is to perform the unblinding of the data for the final results on the measurement of $\mathcal{A}_{CP}$ in $D^0 \to K_S^0 K_S^0$ with Belle and Belle II data.

As an extension on the analysis, we plan analyse the (Belle + Belle II) data-set to use the novel charm flavor tagger [61] and update the results. It is also planned to analyse the (Belle + Belle II) data-set for the decay $D^{*+} \to D^0 \to K_S^0\ (\to \pi^0\ \pi^0) K_S^0\ (\to \pi^+\ \pi^-)$.

Chapter 5

Identification of charged pions using $K^0_S \to \pi^+\pi^-$ decays and the *s*Plot method

This chapter presents a study of particle identification performance for charged pions is studied using a Belle II simulated sample of $K^0_S \to \pi^+\pi^-$. The relative difference between true efficiencies and that obtained from the sPlot technique is studied for different pion-identification criteria in bins of pion momenta.

5.1 Introduction

Inclusive $K^0_S \to \pi^+\pi^-$ decays provides access to large samples of charged pions with momentum below 1 GeV/c, which can be used to study the performance of the particle-identification (PID) algorithms at low momentum [62]. The aim of this work is to develop and validate, using simulation, an analysis method based on the *s*Plot technique [60] to study the PID performance in the context of the Belle II *Systematic Correction Framework* [63]. A fit model is developed for the invariant-mass distribution of the K^0_S candidates, $m(\pi^+\pi^-)$, and used to compute per-candidate weights (dubbed *s*Weights) that can be used to statistically subtract the background and determine the signal distributions of the PID variables. These signal distribution can then be used to evaluate the PID performance in data and/or simulation, by computing PID efficiencies and mis-identification rates as a function of pion kinematics, which are key ingredients for many physics analyses.

This chapter is structured as follows: the data sample and selection criteria used are presented in Section 5.2; the model used to fit the $m(\pi^+\pi^-)$ distribution, from which *s*Weights are computed, is described in Section 5.3; the *s*Plot method for the evaluation of the pion-identification efficiency is validated by comparing with truth-level information in Section 5.4; the results from this analysis are compared with those based on charged pions from $D^{*+} \to D^0(\to K^-\pi^+)\pi^+$ decays in Section 5.5 before concluding.

5.2 Data samples and software

The analysis uses $K_S^0 \to \pi^+\pi^-$ candidates reconstructed using centrally produced skims (`SystematicsCombinedHadronic 10601300`) of simulated events, corresponding to an integrated luminosity of $10\,\text{fb}^{-1}$. The simulation version corresponds to `MC14ri_a` and the software version used is `release-05-02-18`.

Variable	Criteria
$\|d_z\|(\pi^\pm)$	< 4 cm
$\|d_T\|$	< 3.5 cm
# CDC hits ($\pi^\pm$)	> 20
K_S^0 flight-time	> 0.007 ns
Λ^0 mass veto	> 1.130683 GeV/c^2
Prescale factor	50

Table 5.1: Selection criteria used on top of the skim selection.

In the skim, the $K_S^0 \to \pi^+\pi^-$ candidates are selected from the `K_S0:merged` list by requesting candidates with converged fits from `TreeFitter` [64], which satisfy $0.4 < m(\pi^+\pi^-) < 0.6\,\text{GeV}/c^2$ and have the cosine of the angle between the momentum and the flight direction greater than 0.998. The resulting `KS0:skim` list is then filtered at the analysis level with the criteria reported in Table 5.1, most of which are inherited from Ref. [62]. The pion tracks are required to have $|d_z| < 2\,\text{cm}$ and at least 20 CDC hits. The latter requirement ensures good PID performance from the dE/dx measured in the CDC and improves momentum and $m(\pi^+\pi^-)$ resolution. The transverse distance of the K_S^0 decay vertex from the origin is required to be less than 3.5 cm, corresponding to the distance of the innermost layer of the SVD, to restrict the analysis to charged pions that have traversed the tracking detectors that provide measurements of the dE/dx. The K_S^0 decay time is requested to be greater than 0.007 ns to suppress the background due random combination of two charged pions originating from the interaction region. A veto on the invariant mass computed by swapping the pion and proton hypothesis, $m(p\pi^-) > 1.130683\,\text{GeV}/c^2$, is used to eliminate candidates arising from $\Lambda^0 \to p\pi^-$ decays. The χ^2 probability of K_S^0 vertex from `TreeFitter` is required to be greater than 0.01. A pre-scale factor of 1/50 is also applied.

5.3 Model for the $m(\pi^+\pi^-)$ distribution

The $m(\pi^+\pi^-)$ distribution of the selected candidates is modeled using a signal component and a background component. The signal component is described by the sum of a Gaussian distribution and a Johnson S_U distribution [58],

$$\text{pdf}_{\text{sig}}(m(\pi^+\pi^-)) = f_J J(m|\mu_J, \sigma_J, \delta_J, \gamma_J) + (1 - f_J)\left[f_G G(m|\mu_G, \sigma_G)\right], \quad (5.1)$$

with

$$J(x|\mu,\sigma,\delta,\gamma) = \frac{e^{-\frac{1}{2}\left[\gamma\ +\ \delta\ \sinh^{-1}\left(\frac{x-\mu}{\sigma}\right)\right]^2}}{\sqrt{1+\left(\frac{x-\mu}{\sigma}\right)^2}}. \tag{5.2}$$

The background component is modeled using a 2nd order Chebyshev polynomial. The total fit function is defined as

$$f(m(\pi^+\pi^-)) = N_{\text{sig}}\text{pdf}_{\text{sig}}(m(\pi^+\pi^-))\ + N_{\text{bkg}}\text{pdf}_{\text{bkg}}(m(\pi^+\pi^-), \tag{5.3}$$

where $N_{\text{sig(bkg)}}$ represents the signal (background) yield. The results of a binned maximum-likelihood fit to the $m(\pi^+\pi^-)$ distribution, where all parameters are left free to float, are reported in Figure 5.1.

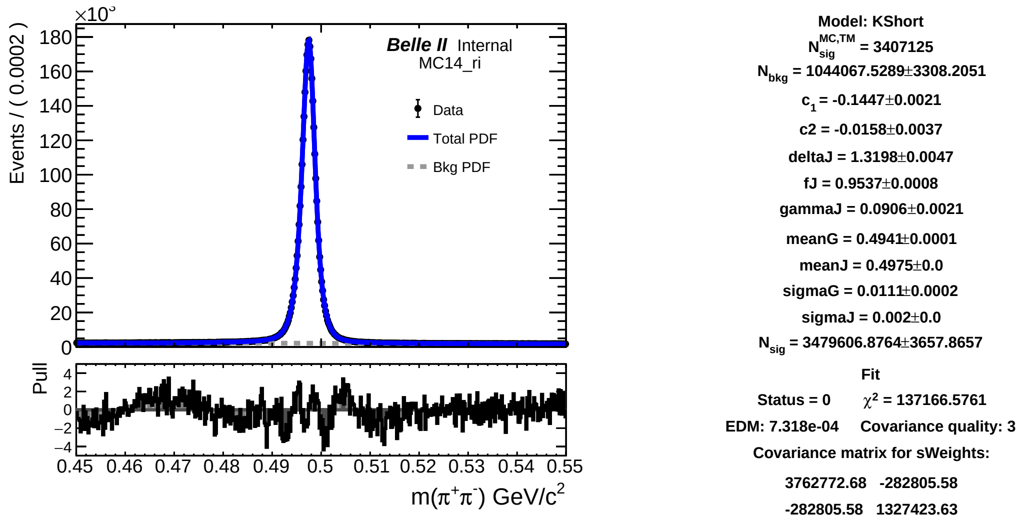

Figure 5.1: Distributions of $m(\pi^+\pi^-)$ with fit results overlaid.

5.4 Validation of the *s*Plot technique with truth-level information

The *s*Weights computed from the $m(\pi^+\pi^-)$ fit are used to derive background-subtracted distributions of momentum and the $\cos\theta$ of the two pions from the selected K^0_S signal decays, which are compared in Figure 5.2 with the signal distributions based truth-matching with `isSignal==1`. There is fairly good agreement between the momentum and the $\cos\theta$ distributions of the pions.

The *s*Weights are then used to compute signal efficiencies for different pion-identification criteria (pionID > 0.1, 0.5 and 0.9) as a function of momentum and polar angle, as shown in Figure 5.3. The same figure shows also the relative difference with the true efficiencies

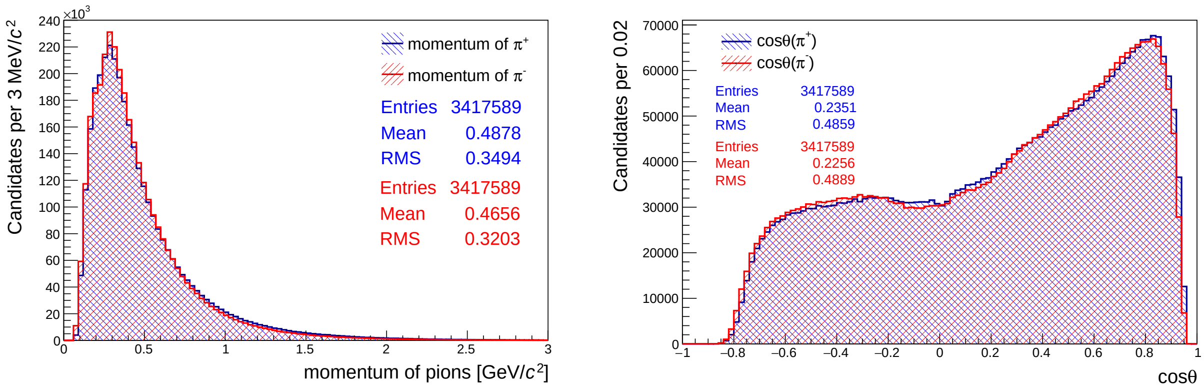

Figure 5.2: Overlapped distributions of (left) momenta and (right) $\cos\theta$ for the pions.

determined using truth-matching:

$$\text{mc\_syst\_error} = \frac{(\epsilon_{sW} - \epsilon_{TM})}{\epsilon_{TM}}, \tag{5.4}$$

where ϵ_{sW} is the sWeighted efficiency and ϵ_{TM} is the efficiency based on truth-matching. The relative difference between true and measured efficiencies is observed to increase in bins of momenta with the maximum difference being $\approx 7.5\%$, and as a function of $\cos\theta$ for tighter pion-identification requirements.

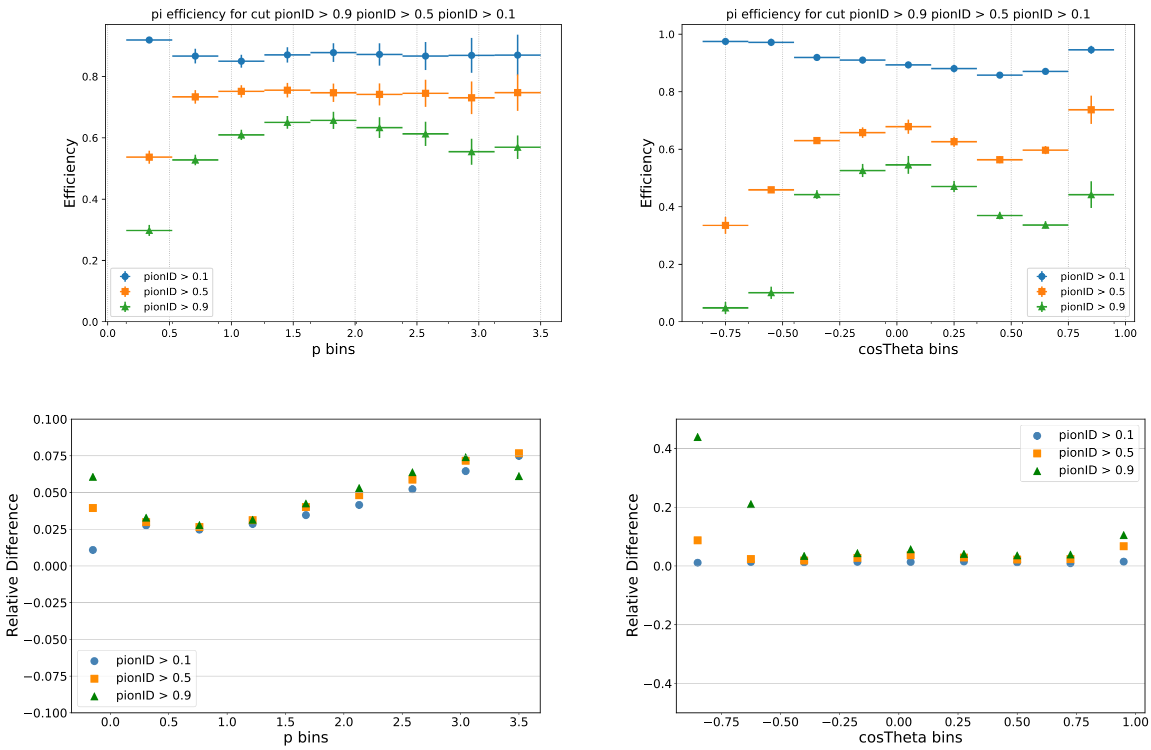

Figure 5.3: (Top) Measured efficiencies and (bottom) relative difference between measured and true efficiencies of different pion-identification criteria as a function of (left) momentum and (right) cosine of the polar angle.

The differences between true and measured efficiencies may arise from systematic uncertainties in the analysis method and/or in inaccuracies of the truth-matching procedure. We test the impact of the analysis method by varying the $m(\pi^+\pi^-)$ fit model and by checking for the presence of correlations $m(\pi^+\pi^-)$ and kinematic/PID variables.

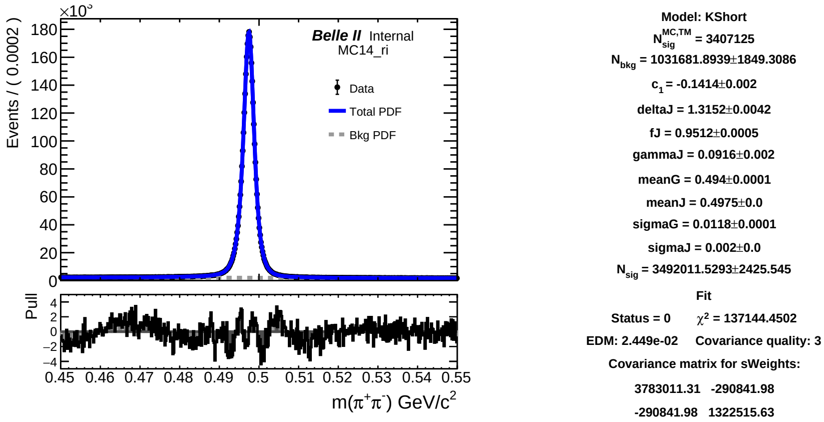

Figure 5.4: Results of the $m(\pi^+\pi^-)$ fit based on the alternative background model.

The $m(\pi^+\pi^-)$ fit model is varied by changing the background shape to a 1st order polynomial. Such alternative fit (Figure 5.4) shows an equally good description of the data, but this only marginally affects the determination of the signal efficiencies, which agree with the nominal results within 0.5%.

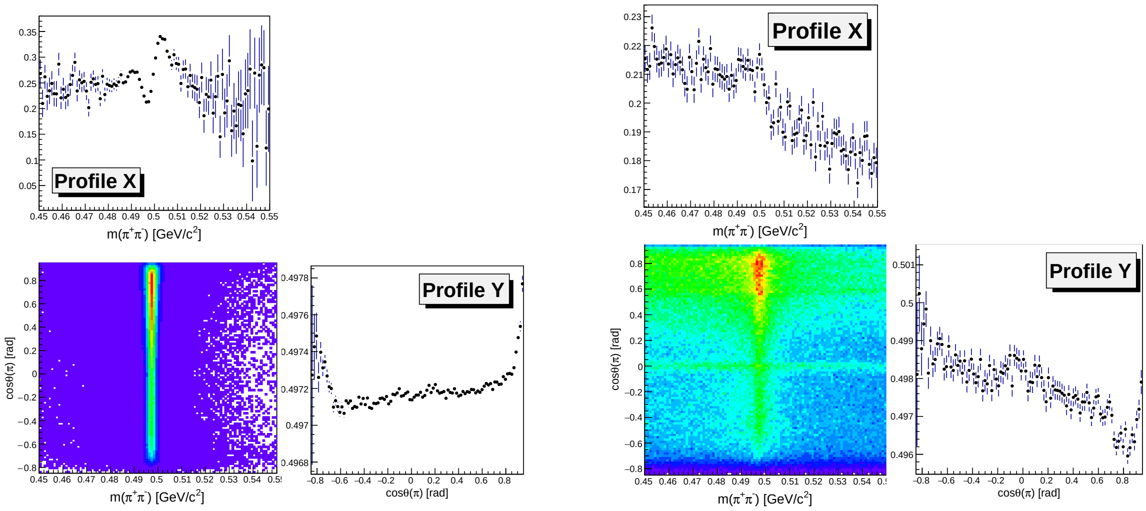

Figure 5.5: Distribution and profile of K^0_S $\cos\theta$ versus $m(\pi^+\pi^-)$ for (left) signal and (right) background decays.

The kinematic dependence of the deviation between sWeighted and truth-matching efficiencies may be due to the presence of correlations between $m(\pi^+\pi^-)$ and the pion kinematics (Figure 5.6 and Figure 5.5), which invalidates one of the underlying assumption of the sPlot method. The correlation is mainly present for the background decays,

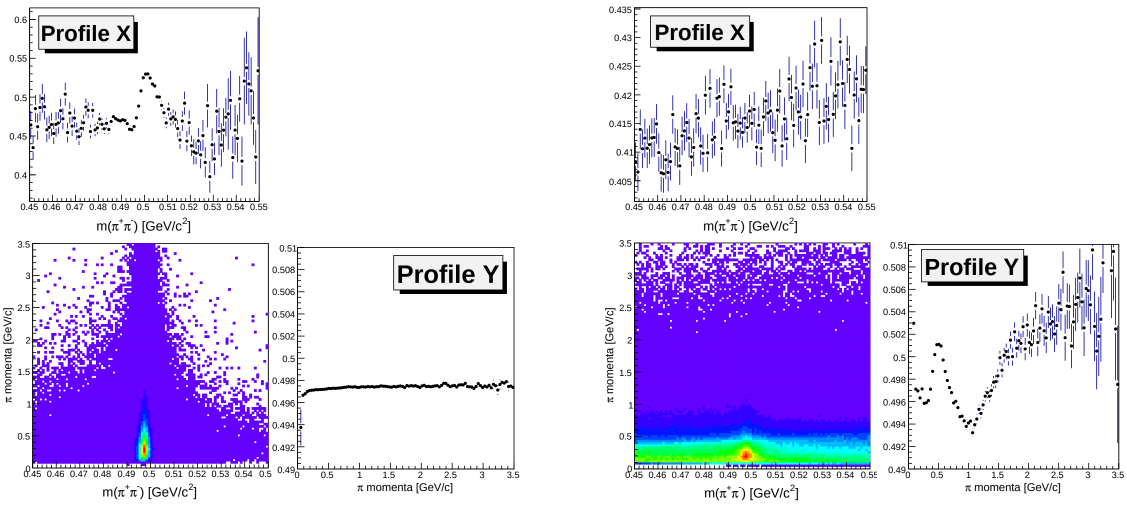

Figure 5.6: Distribution and profile of K_S^0 momentum versus $m(\pi^+\pi^-)$ for (left) signal and (right) background decays.

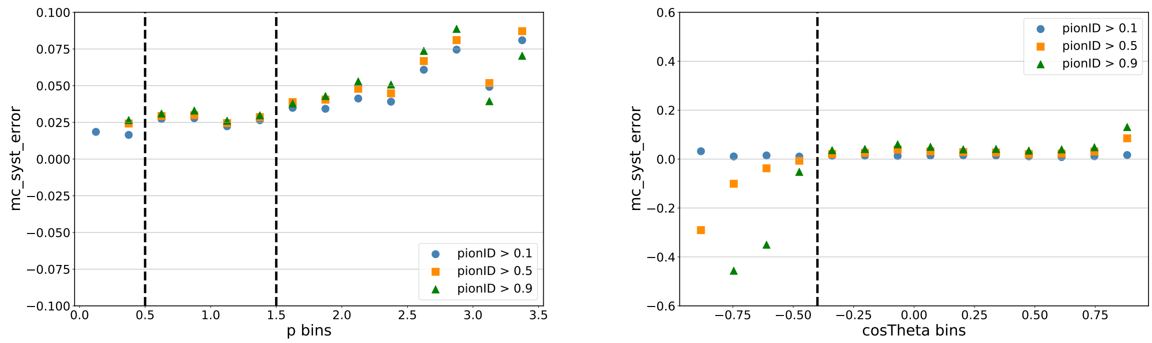

Figure 5.7: Bins of momentum (left) and $\cos\theta$ (right). Bins are shown using dashed black lines.

and mainly between $m(\pi^+\pi^-)$ and momentum as also shown in Figure 5.6. The impact of these correlations is evaluated by computing sWeights based on three independent fits to the $m(\pi^+\pi^-)$ distributions of candidates restricted in disjoint ranges of momentum and $\cos\theta$. Figure 5.7 shows the chosen bins. The momentum range is split into $[0, 0.5]$ GeV/c, where there is a slight downward trend of mc_syst_err, $[0.5, 1.5]$ GeV/c, where the distribution of mc_syst_err is flat, and $[1.5, 3.5]$ GeV/c, where an increasing trend is visible. The bins of $\cos\theta$ are chosen to be $[-0.95, -0.4]$ and $[-0.4, 0.95]$. Figure 5.8 and Figure 5.9 show the $m(\pi^+\pi^-)$ distributions in the disjoint bins of momenta and $\cos\theta$, respectively, with fit projections overlaid. A comparison of the resulting mc_syst_err with that obtained from the default analysis, also shown in the figures, indicates that correlations between kinematic variables and $m(\pi^+\pi^-)$ are not the source of the discrepancies between sWeighted and truth-matching efficiencies.

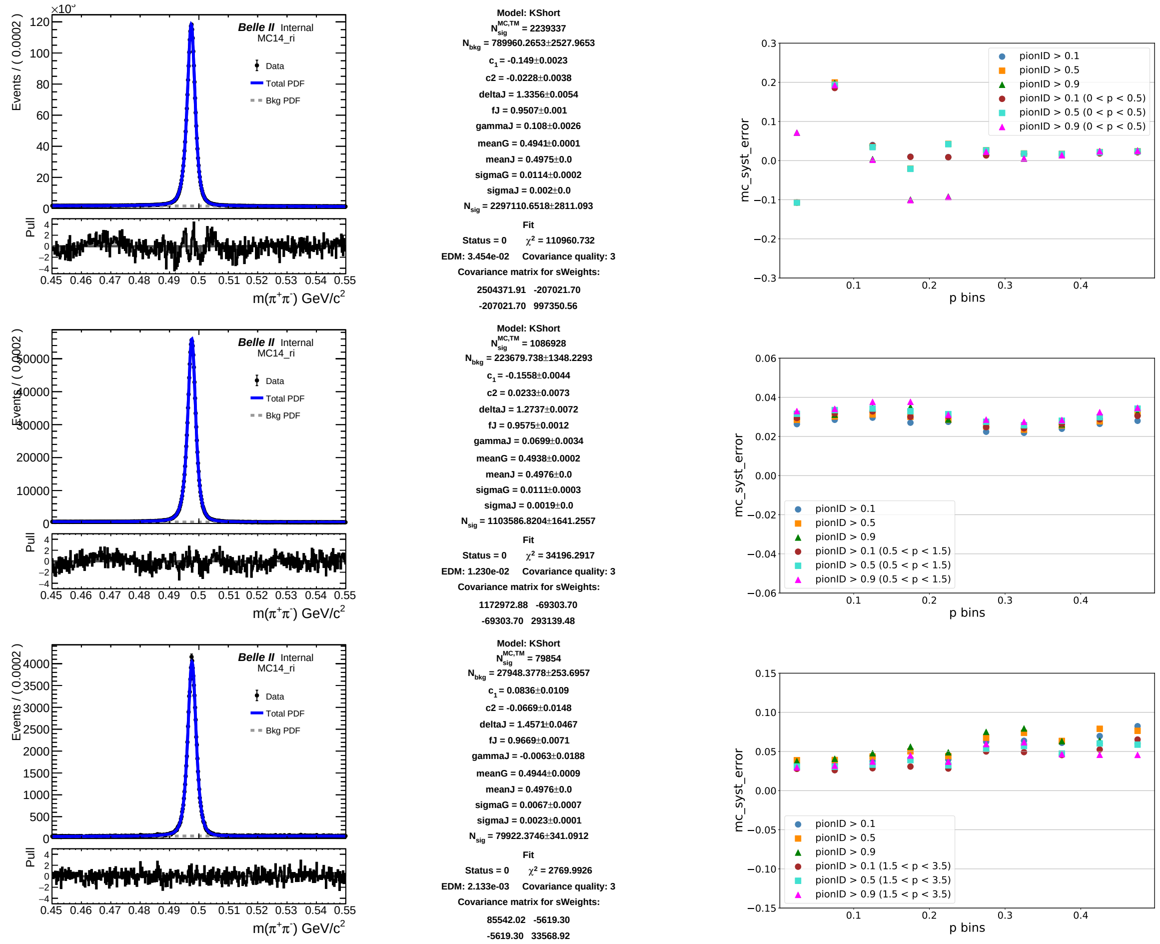

Figure 5.8: (Left) Distributions of $m(\pi^+\pi^-)$ for (top) $0 < p < 0.5\,\mathrm{GeV}/c$, (middle) $0.5 < p < 1.5\,\mathrm{GeV}/c$ and (bottom) $1.5 < p < 3.5\,\mathrm{GeV}/c$, with fit results overlaid. (Right) Comparisons of the resulting mc_syst_err with the default analysis, in which the $m(\pi^+\pi^-)$ distribution integrated in momentum is fit.

5.5 Comparison with results on the D^{*+} sample

The pion-identification efficiencies measured in this analysis are compared to those measured using charged pions from $D^0 \to K^-\pi^+$ candidates that arise from $D^{*+} \to D^0\pi^+$ decays. The pions from the D^0 decay have a larger momentum compared to the pions from the K^0_S decay, but as shown in Figure 5.10 there is enough overlap in the kinematic distributions to allow for a meaningful comparison. The D^{*+} sample used in the comparison consists of MC14 run-dependent simulated events (`MC14rd_e10`), which are reconstructed and analyzed in the systematic framework using an *s*Plot method similar to that discussed in the note. The sample corresponds to an integrated luminosity of $14.6\,\mathrm{fb}^{-1}$.

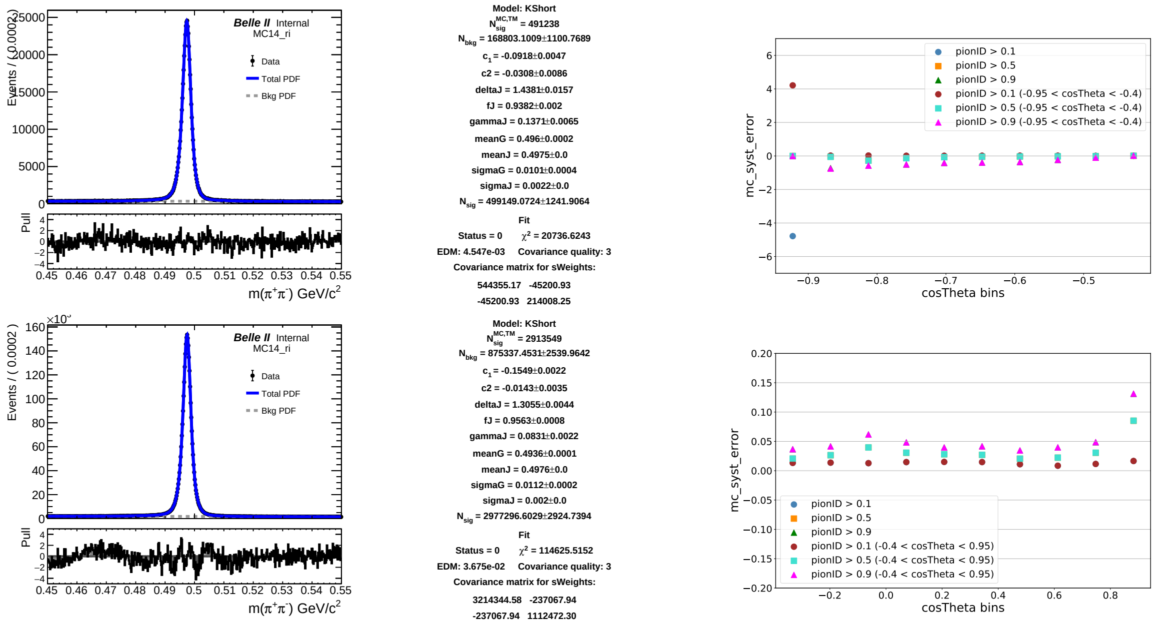

Figure 5.9: (Left) Distributions of $m(\pi^+\pi^-)$ for (top) $-0.95 < \cos\theta < -0.4$ and (bottom) $-0.4 < \cos\theta < 0.95$, with fit results overlaid. (Right) Comparisons of the resulting mc_syst_err with the default analysis, in which the $m(\pi^+\pi^-)$ distribution integrated in $\cos\theta$ is fit.

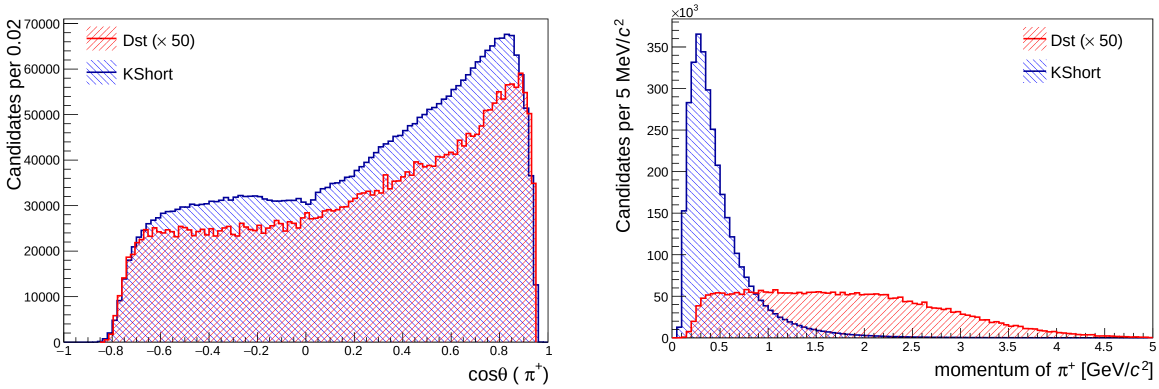

Figure 5.10: Overlapped distributions of cosθ (left) and momenta (right) for the pions from $K^0_S \to \pi^+ \, \pi^-$ and $D^{*+} \longrightarrow D^0(\longrightarrow K^-\pi^+)\pi^+$. The distribution that correspond to the `Dst` are model are normalized to luminosity by a factor of 0.68 and fifty times enhanced for comparison.

The ratio between the pion-identification efficiencies obtained with the two samples is computed in bins of momentum and $\cos\theta$ for the different requirements of the cut on pionID . The results, reported in Figure 5.11, show that the pion-identification efficiencies are statistically consistent.

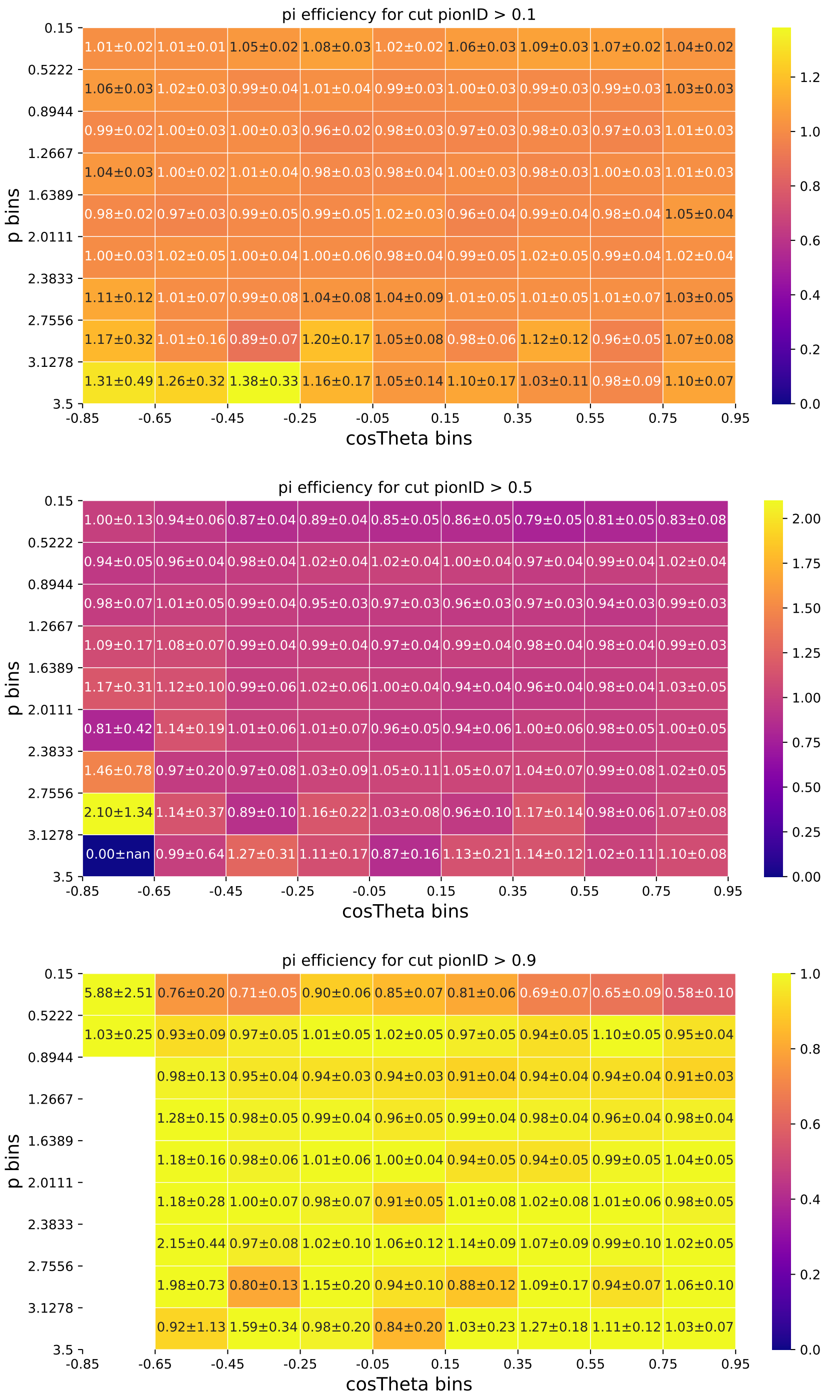

Figure 5.11: Ratio of efficiencies derived using the K_S^0 and D^{*+} samples, in bins of $\cos\theta$ and momentum, for pionID greater than (top) 0.1, (middle) 0.5 and (bottom) 0.9.

5.6 Summary

The $K_S^0 \to \pi^+ \pi^-$ sample gives access to low momentum pions, which are useful for studies of particle-identification performance. Using simulated data, we have developed and validated and analysis procedure based on the *s*Plot method that can be used as part of the Belle II *Systematic Correction Framework* to perform these studies.

Chapter 6

Data/MC comparison of the cluster properties of the Belle II SVD

6.1 Introduction

To indirectly investigate new physics at Belle II, accurate decay vertex determination and low-momentum monitoring are essential. Two layers, layer 1 and layer 2, make up the six-layer VerteX Detector (VXD), which reconstructs charged particles close to the contact point. A brief overview of the Belle II SVD is discussed in Section 2.2.2. A schematic view of the complete VXD can be found in Figure 6.1.

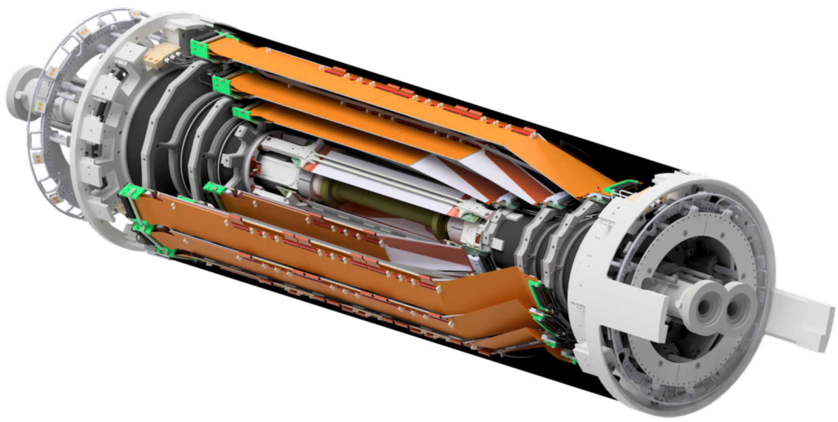

Figure 6.1: The Belle II vertex detector (VXD). The VXD is made up of the pixel detector (PXD) (two inner most layers) and silicon strip (SVD) detectors (layers 3 -6) [65].

As a part of the service task, I prepared a software module to study the cluster properties (cluster energy, cluster signal to noise ratio (SNR) and cluster size) as a function of the track incident angle and made a preliminary comparison of the Data and MC.

6.2 Data samples and software

We simulated and reconstructed 10000 generic Υ(4S) events with official beam background files. The data sample used is `Phase3, Proc9, experiment 7`. The run numbers corresponding to this data sample are: `1353, 1355, 1356, 1359, 1360, 1364, 1365, 1366, 1367` with an integrated luminosity of 13 pb^{-1}. The software version used for this analysis is `release-03-2-04`.

6.3 Incident angle convention of a track

To study the cluster properties as a function of the track incident angle, we need to understand the convention used to determine the track incident angle. The convention of track incident angle is clearly shown in Figure 6.2.

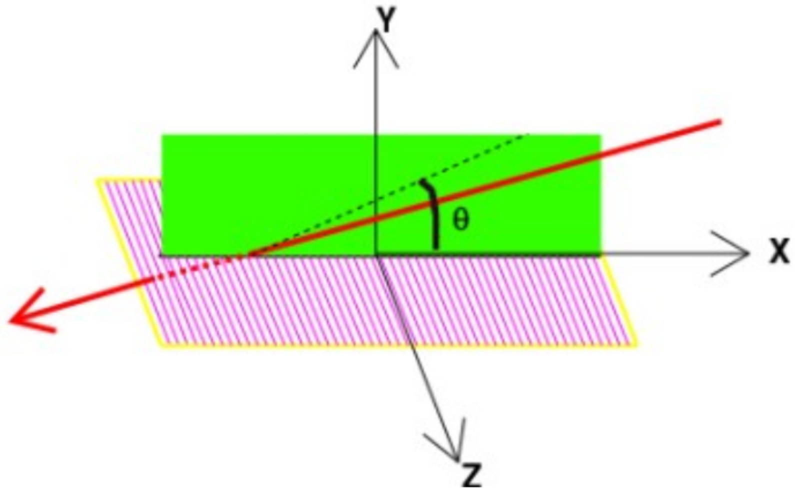

Figure 6.2: Schematic diagram showing the convention for track incident angle [66].

We assume the SVD sensor plane to be XZ plane. The strips of the sensor (pink) are taken to be parallel to the Z axis. XY plane (green) perpendicular to the sensor plane (XZ). A track passing through the sensor is shown by red arrow. Dashed line is the projection of the track on the XY plane. Incident angle θ is the angle between X axis and the projection of the track (dashed: extrapolated track) on XY plane. The tangent of the incident angle θ. The U, V direction tangent of the track extrapolated to the sensor can be obtained from `SVDIntercept`.

6.4 Selection of tracks

Fitted tracks are obtained using pion hypothesis. To make sure the tracks originate from the interaction point the cuts applied are : $|d_0| < 0.2$ cm and $|z_0| <0.5$ cm. Here, d_0 is the signed distance to the IP in the $r-\phi$ plane and z_0 is the z co-ordinate of the perigee. The number of tracks coming from IP is required to exceed four. The track related clusters are reconstructed using the relations between `SVDClusters` and `Recotracks`. The intercepts related to the selected tracks selected using the relation between `SVDIntercepts` and `Recotracks`. Finally the cluster properties are stored only if the layer, ladder, sensor of the selected intercepts are exactly the same as that of the selected track related cluster.

6.5 Cluster properties

Particle interaction with the detector material generates a group of hits in multiple segments. To identify the particles that make up an event and to assign them the kinematic parameter (energy, momenta, etc), the signals received from the readout channels must be grouped, so as to approximate the real origin of each hit in the detector. This processes is called '***clustering***' and the groups are termed as ***'clusters'***. The deposited charge is shared among a number of strips.

The SVD clusterizer algorithm scans each SVD sensor and groups of strips to form SVD clusters. Only meaningful strips are selected in this process, whilst neglecting fake hits and random noise, by using clustering thresholds. These clusters are characterized by different properties like :

- ***Cluster energy:*** Total energy deposited in a cluster is called *cluster energy.* Cluster energy is important for accurately determining the type and kinematics of the particle.

- ***Signal-to-Noise Ratio (SNR)***: The Signal-to-Noise Ratio (SNR) is defined as the cluster charge divided by the noise value of the strip. If the cluster width is more than 1, the noise value is estimated as the sum in quadrature of the noises of clustered strips. SVD strips are selected for clustering only if they satisfy a minimum criteria on their SNR.

- ***Cluster size:*** The number of adjacent detector elements or channels that are triggered by the passage of a charged particle through the detector material is called *cluster size.* This property is important to determine spatial resolution.

In the following section, the data-MC comparison of these cluster properties are studied. The comparison for cluster energy is given in Figure 6.3.

6.6 Results

Data and MC are roughly in agreement for the cluster energy spectra of clusters for L3.1.2 U/V and L4.1.2.U/V.

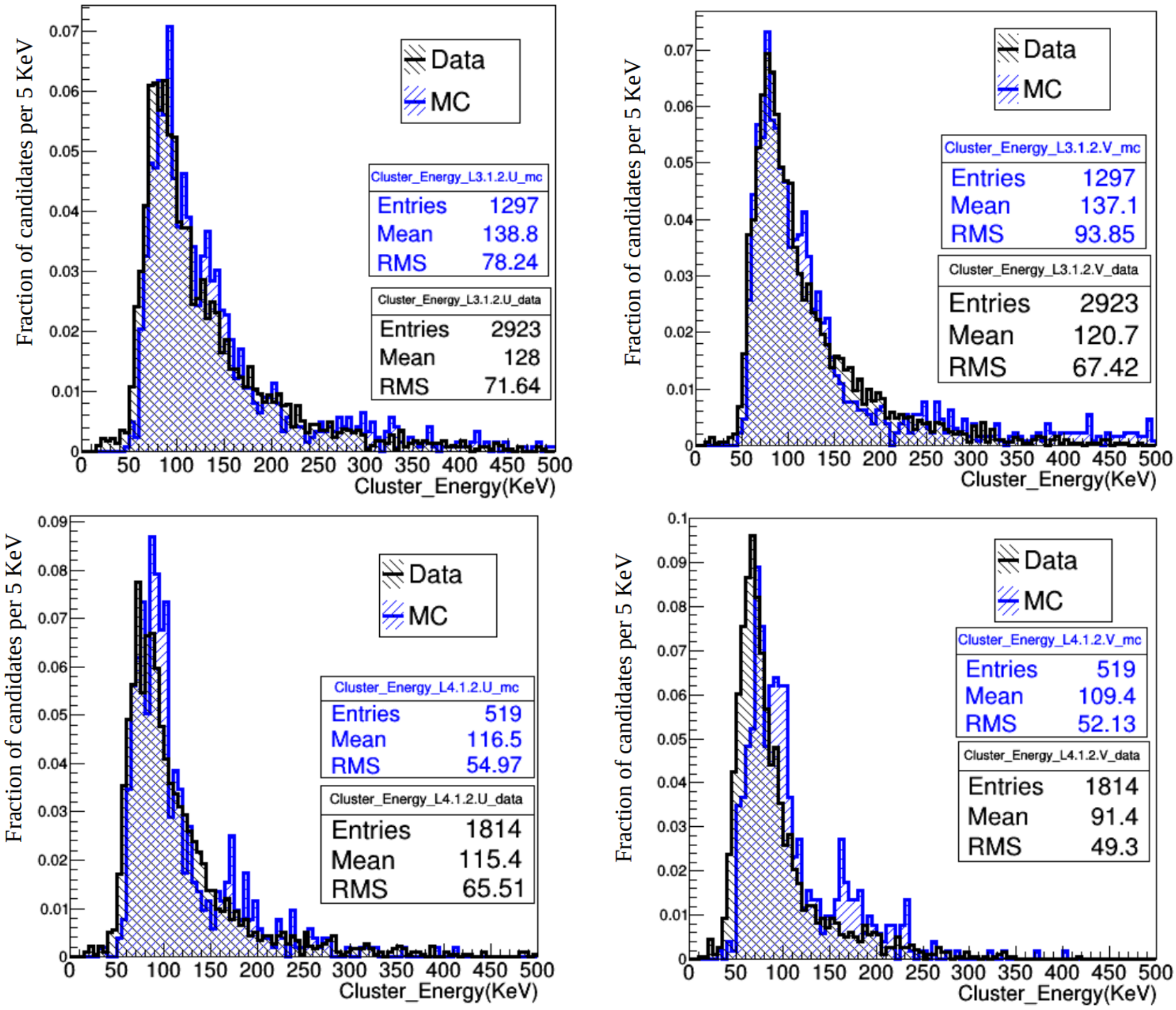

Figure 6.3: Cluster energy spectra for layers 3.1.2 U (top left), 3.1.2 V (top left), 4.1.2 U (bottom left) and 4.1.2 V (bottom right).

The SNR is measured to be larger for the *V* side as compared to that of the *U* side. This is due to the longer strips giving a larger capacitive load to the pre-amplifier. The Data and MC are roughly in agreement for U/V separately as shown in Figure 6.4.

Cluster size for data in *U* side is larger than that in MC. Distribution of cluster size for *V* side are in better agreement for MC and data as compared to the U/P side as shown in Figure 6.5

6.7 Summary

Data and MC are roughly in agreement for the cluster energy spectra for sensors L3.1.2 and L4.1.2 for both U and V side. The SNR for the *V* side is measured to be larger as compared to that of the *U* side. Larger SNR for the V side is due to longer strips giving a larger capacitive load to the pre-amplifier. Distribution of cluster size for *V* side are in better agreement for MC and data as compared to the U side.

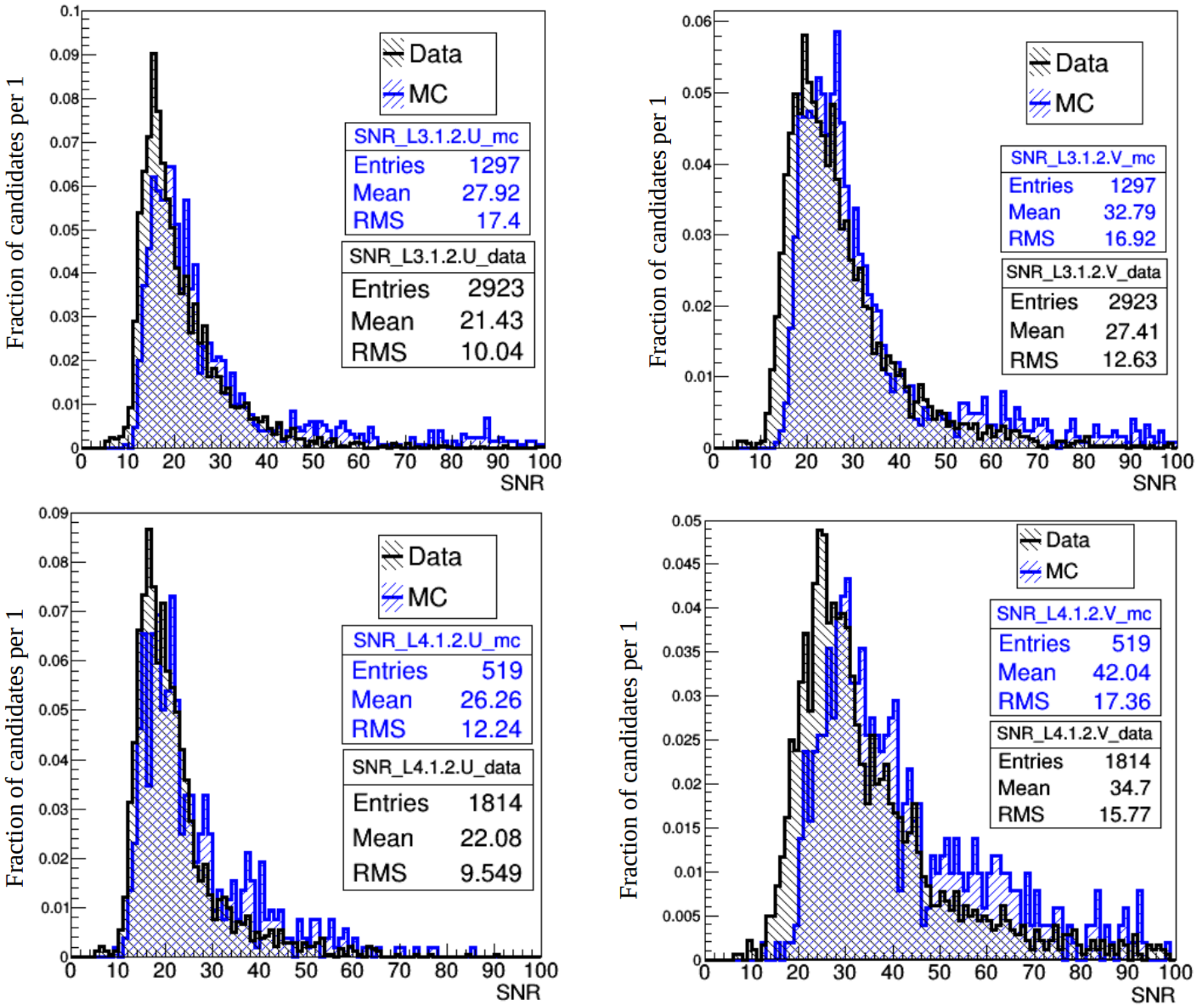

Figure 6.4: SNR for layers 3.1.2 U (top left), 3.1.2 V (top left), 4.1.2 U (bottom left) and 4.1.2 V (bottom right).

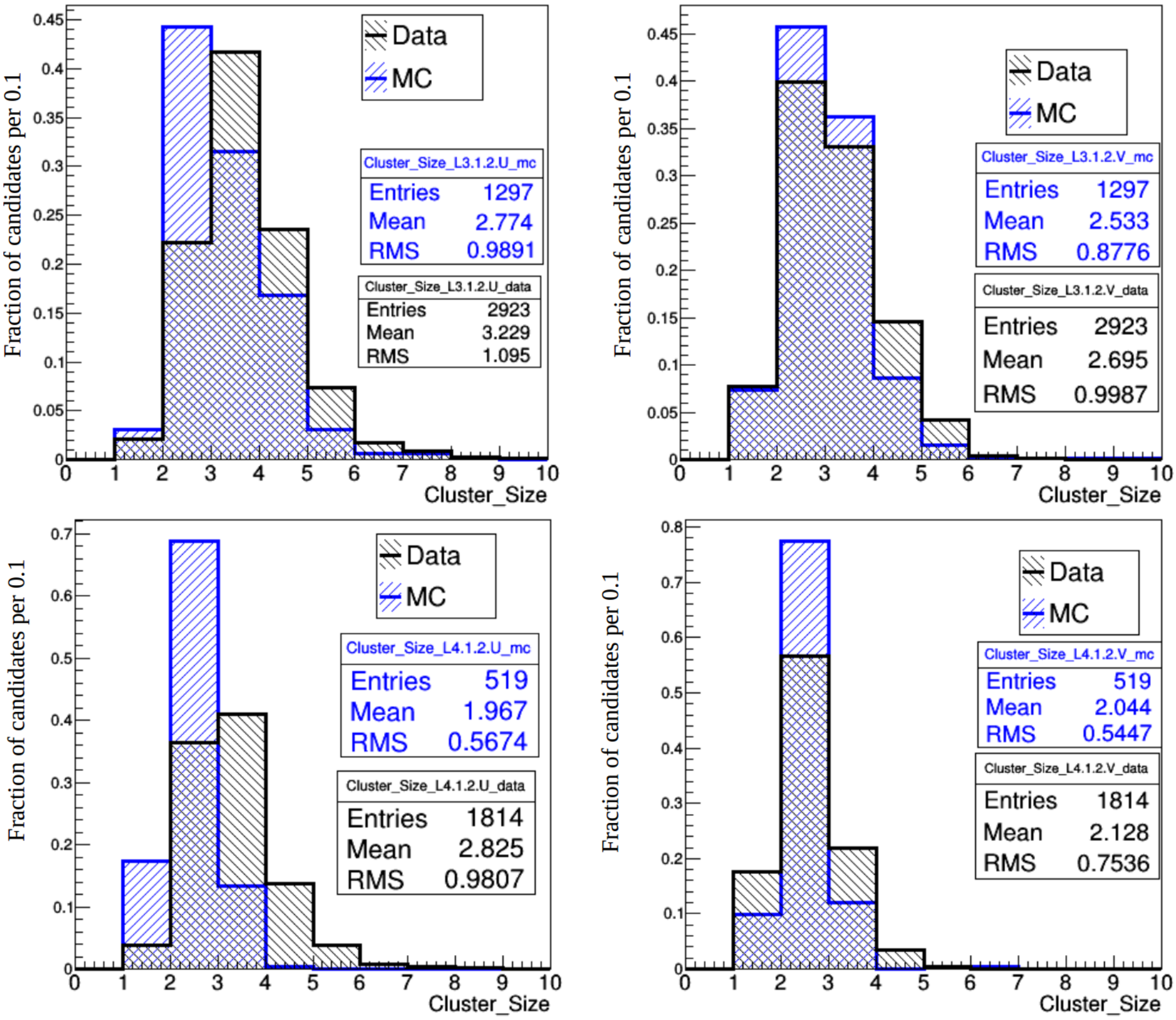

Figure 6.5: Cluster size for layers 3.1.2 U (top left), 3.1.2 V (top left), 4.1.2 U (bottom left) and 4.1.2 V (bottom right).

Chapter 7

Summary and conclusions

Using D^{*+}-tagged $D^0 \to K_S^0 K_S^0$ and $D^0 \to K^+K^-$ decays reconstructed with an integrated luminosity $980\,\mathrm{fb}^{-1}$ of Belle data, and $420\,\mathrm{fb}^{-1}$ of Belle II data, the time-integrated *CP* asymmetry in $D^0 \to K_S^0 K_S^0$ decays, is measured to be

$$\mathcal{A}_{CP}(D^0 \to K_S^0 K_S^0) = (1.3 \pm 1.3(\text{stat}) \pm 0.1(\text{syst}))\% \text{ (blind)}\,. \tag{7.1}$$

This result is $\approx 14\%$ more precise than the previous Belle measurement and is competitive with the world-best measurement from LHCb [52] and consistent with no *CP* violation. Future task for the analysis is to perform the unblinding of the data for the final results on the measurement of $\mathcal{A}_{CP}$ in $D^0 \to K_S^0 K_S^0$ with Belle and Belle II data. These results are to be published soon.

I have also contributed towards the software development activities for the experiment. I performed a study on the identification of low momentum charged pions using the decay $K_S^0 \to \pi^+ \pi^-$ decays, in the context of the `Belle II Systematics Correction Framework`. I addition, have also contributed to studying the data/MC comparison of the cluster properties of the Belle II SVD.

Bibliography

[1] A. D. Sakharov, *Violation of CP invariance, C asymmetry, and baryon asymmetry of the universe*, Pisma Zh. Eksp. Teor. Fiz. **5** (1967) 32–35. Usp. Fiz. Nauk **161** (1991) 61.

[2] N. Cabibbo, *Unitary Symmetry and Leptonic Decays*, Phys. Rev. Lett. **10** (1963) 531–533.

[3] M. Kobayashi and T. Maskawa, *CP Violation in the Renormalizable Theory of Weak Interaction*, Prog. Theor. Phys. **49** (1973) 652–657.

[4] R. Aaij et al., LHCb collaboration, *Observation of CP violation in charm decays*, Phys. Rev. Lett. **122** (2019) 211803.

[5] E. Noether, *Invariante Variationsprobleme*, Nachrichten von der Gesellschaft der Wissenschaften zu Göttingen, Mathematisch-Physikalische Klasse **1918** (1918) 235–257. `http://eudml.org/doc/59024`.

[6] T. D. Lee and C.-N. Yang, *Question of Parity Conservation in Weak Interactions*, Phys. Rev. **104** (1956) 254–258.

[7] R. L. Garwin, L. M. Lederman, and M. Weinrich, *Observations of the Failure of Conservation of Parity and Charge Conjugation in Meson Decays: The Magnetic Moment of the Free Muon*, Phys. Rev. **105** (1957) 1415–1417.

[8] C. S. Wu, E. Ambler, R. W. Hayward, D. D. Hoppes, and R. P. Hudson, *Experimental Test of Parity Conservation in β Decay*, Phys. Rev. **105** (1957) 1413–1414.

[9] J. H. Christenson, J. W. Cronin, V. L. Fitch, and R. Turlay, *Evidence for the 2π Decay of the K_2^0 Meson*, Phys. Rev. Lett. **13** (1964) 138–140.

[10] J. E. Augustin et al., SLAC-SP-017, *Discovery of a Narrow Resonance in e^+e^- Annihilation*, Phys. Rev. Lett. **33** (1974) 1406–1408.

[11] J. J. Aubert et al., E598, *Experimental Observation of a Heavy Particle J*, Phys. Rev. Lett. **33** (1974) 1404–1406.

[12] S. W. Herb et al., E288, *Observation of a Dimuon Resonance at 9.5-GeV in 400-GeV Proton-Nucleus Collisions*, Phys. Rev. Lett. **39** (1977) 252–255.

[13] F. Abe et al., CDF, *Observation of top quark production in $\bar{p}p$ collisions*, Phys. Rev. Lett. **74** (1995) 2626–2631.

[14] S. Abachi et al., D0, *Search for high mass top quark production in $p\bar{p}$ collisions at $\sqrt{s} = 1.8$ TeV*, Phys. Rev. Lett. **74** (1995) 2422–2426.

[15] V. Fanti et al., NA48, *A New measurement of direct CP violation in two pion decays of the neutral kaon*, Phys. Lett. B **465** (1999) 335–348.

[16] A. Alavi-Harati et al., KTeV, *Observation of direct CP violation in $K_{S,L} \to \pi\pi$ decays*, Phys. Rev. Lett. **83** (1999) 22–27.

[17] B. Aubert et al., BaBar, *Observation of CP violation in the B^0 meson system*, Phys. Rev. Lett. **87** (2001) 091801.

[18] K. Abe et al., Belle, *Observation of large CP violation in the neutral B meson system*, Phys. Rev. Lett. **87** (2001) 091802.

[19] B. Aubert et al., BaBar, *Observation of direct CP violation in $B^0 \to K^+\pi^-$ decays*, Phys. Rev. Lett. **93** (2004) 131801.

[20] B. Aubert et al., BaBar, *Observation of CP violation in $B^0 \to K^+\pi^-$ and $B^0 \to \pi^+\pi^-$*, Phys. Rev. Lett. **99** (2007) 021603.

[21] L.-L. Chau and W.-Y. Keung, *Comments on the Parametrization of the Kobayashi-Maskawa Matrix*, Phys. Rev. Lett. **53** (1984) 1802.

[22] L. Wolfenstein, *Parametrization of the Kobayashi-Maskawa Matrix*, Phys. Rev. Lett. **51** (1983) 1945.

[23] R. Workman et al., Particle Data Group, *Review of particle physics*, Prog. Theor. Exp. Phys. **2022** (2022) 083C01.

[24] A. L. K. Y. Grossman and Y. Ni, *New physics and CP violation in singly Cabibbo suppressed D decays*, Phys. Rev. D **75** (2007) 036008.

[25] R. Aaij et al., LHCb collaboration, *Measurement of the time-integrated CP asymmetry in $D^0 \to K^+K^-$ decays*, Phys. Rev. Lett. **131** (2023) no. 9, 091802.

[26] M. Chala, A. Lenz, A. V. Rusov, and J. Scholtz, *ΔA_{CP} within the Standard Model and beyond*, JHEP **07** (2019) 161.

[27] F. Buccella, A. Paul, and P. Santorelli, *$SU(3)_F$ breaking through final state interactions and CP asymmetries in $D \to PP$ decays*, Phys. Rev. D **99** (2019) 113001.

[28] Y. Grossman and S. Schacht, *The emergence of the $\Delta U = 0$ rule in charm physics*, JHEP **07** (2019) 020.

[29] S. Kurokawa et al., *Overview of the KEKB accelerators*, Nucl. Instrum. Meth. **449** (2003) 1–7.

[30] A. Abashian et al., Belle Collaboration, *The Belle detector*, Nucl. Instrum. Meth. **479** (2002) 117–232.

[31] M. Wang et al., *Beam test of the BELLE extreme forward calorimeter at KEK*, Nucl. Instrum. Meth. **455** (2000) 319–323.

[32] E. Nygård et al., *CMOS low noise amplifier for microstrip readout Design and results*, Nucl. Instrum. Meth. **301** (1991) 506–516.

[33] S.Uno et al., *Study of a drift chamber filled with a helium - ethane mixture*, Nucl. Instrum. Meth. **330** (1993) 55–63.

[34] D. Mohapatra, *Observation of $b \longrightarrow d\gamma$ decays and determination of $|V_{td}/V_{ts}|$*, 2006.

[35] Akai et al., *SuperKEKB collider*, Nucl. Instrum. Meth. **907** (2018) 188–199.

[36] Y. Funakoshi et al., *The SuperKEKB Has Broken the World Record of the Luminosity*, JACoW **IPAC2022** (2022) 1–5.

[37] *SuperB Conceptual Design Report, INFN/AE - 07/2, SLAC-R-856, LAL 07-15*, .

[38] T. Abe et al., Belle-II, *Belle II Technical Design Report*, `arXiv:1011.0352 [physics.ins-det]`.

[39] C. Irmler et al., *Run and slow control system of the Belle II silicon vertex detector*, Nucl. Instrum. Meth. **958** (2020) 162706.

[40] T. Bilka et al., *Belle II Vertex Detector Performance*, PoS Vertex 2019 **373** (2020) .

[41] M. Frenchand et al., *Design and results from the APV25, a deep sub-micron CMOS front-end chip for the CMS tracker*, Nucl. Instrum. Meth. **466** (2001) 359–365.

[42] K. Adamczyk et al., *Belle II silicon vertex detector*, Nucl. Instrum. Meth. **831** (2016) 80–84.

[43] S. Iwata et al., *Progress of Theoretical and Experimental Physics*, **2016** (2016) 033H01.

[44] V. Aulchenko et al., *Time and energy reconstruction at the electromagnetic calorimeter of the Belle-II detector*, Journal of Instrumentation **12** (2017) C08001.

[45] I.Adachi et al., *Detectors for extreme luminosity: Belle II*, Nucl. Instrum. Meth. **907** (2018) 46–59.

[46] M. Gelb et al., *B2BII: Data Conversion from Belle to Belle II*, Comput. Softw. Big Sci. **2** (2018) no. 1, 9.

[47] T. Kuhr, C. Pulvermacher, M. Ritter, T. Hauth, and N. Braun, Belle-II Framework Software Group, *The Belle II Core Software*, Comput. Softw. Big Sci. **3** (2019) no. 1, 1.

[48] Belle II collaboration, *Belle II Analysis Software Framework (basf2)*, `https://doi.org/10.5281/zenodo.5574115`.

[49] U. Nierste and S. Schacht, *CP violation in* $D^0 \to K_S^0 K_S^0$, Phys. Rev. D **92** (2015) 054036.

[50] Y. Amhis et al., Heavy Flavor Averaging Group, *Averages of b-hadron, c-hadron, and* τ*-lepton properties as of 2021*, . updated results and plots available at `https://hflav.web.cern.ch/`.

[51] N. Dash et al., Belle collaboration, *Search for CP violation and measurement of the branching fraction in the decay* $D^0 \to K_S^0 K_S^0$, Phys. Rev. Lett. **119** (2017) 171801.

[52] R. Aaij et al., LHCb collaboration, *Measurement of CP asymmetry in* $D^0 \to K_S^0 K_S^0$ *decays*, Phys. Rev. D **104** (2021) no. 3, L031102.

[53] R. Aaij et al., LHCb collaboration, *Search for time-dependent CP violation in* $D^0 \to K^+K^-$ *and* $D^0 \to \pi^+\pi^-$ *decays*, Phys. Rev. D **104** (2021) no. 7, 072010.

[54] T. Aaltonen et al., CDF collaboration, *Measurement of CP-violating asymmetries in* $D^0 \to \pi^+\pi^-$ *and* $D^0 \to K^+K^-$ *decays at CDF*, Phys. Rev. D **85** (2012) 012009.

[55] B. Casey, *HadronB*, Belle Note 390 (2001).

[56] `https://belle.kek.jp/secured/runinfo/dst/skimmed_file/SkimmedFile/e000007/selection.html`.

[57] J.-F. Krohn et al., Belle II Analysis Software Group, *Global decay chain vertex fitting at Belle II*, Nucl. Instrum. Meth. **A976** (2020) 164269.

[58] N. L. Johnson, *Systems of frequency curves generated by methods of translation*, Biometrika **36** (1949) 149–176.

[59] A. Di Canto, *Measurement of CP-violating asymmetries in* $D^0 \to \pi^+\pi^-$ *and* $D^0 \to K^+K^-$ *decays at CDF.* PhD thesis, Pisa U., 4, 2012.

[60] M. Pivk and F. R. Le Diberder, *sPlot: A statistical tool to unfold data distributions*, Nucl. Instrum. Meth. **A555** (2005) 356–369.

[61] I. Adachi et al., Belle II Collaboration, *Novel method for the identification of the production flavor of neutral charmed mesons*, Phys. Rev. D **107** (2023) 112010.

[62] U. Tamponi, *Study of hadron-ID using untagged K_S*, BELLE2-NOTE-TE-2019-024.

[63] Belle II collaboration, *Systematic Corrections Framework*, https://syscorrfw.readthedocs.io/en/latest/index.html.

[64] J.-F. Krohn et al., Belle II analysis software Group, *Global decay chain vertex fitting at B-factories*, Nucl. Instrum. Meth. **976** (2020) 164269.

[65] K. Adamczyk et al., *The design, construction, operation and performance of the Belle II silicon vertex detector*, Journal of Instrumentation **17** (2022) no. 11, P11042.

[66] S. Halder et al., *Performance of Belle II Silicon Vertex Detector in Phase-2*, BELLE2-NOTE-TE-2019-026.

Appendix A

Correlations between fit parameters

	A_{bkg}	$A_{K_S^0\pi\pi}$	$A_{K_S^0K_S^0}$	N_{bkg}	$N_{K_S^0\pi\pi}$	$N_{K_S^0K_S^0}$
α	-0.001	0.003	0.002	-0.139	0.089	0.058
A_{bkg}		-0.086	-0.055	0.001	-0.000	-0.001
$A_{K_S^0\pi\pi}$			-0.075	-0.003	0.003	-0.001
$A_{K_S^0K_S^0}$				-0.002	-0.001	0.005
N_{bkg}					-0.097	-0.063
$N_{K_S^0\pi\pi}$						-0.069
$N_{K_S^0K_S^0}$						

	A_{bkg}	$A_{K_S^0\pi\pi}$	$A_{K_S^0K_S^0}$	N_{bkg}	$N_{K_S^0\pi\pi}$	$N_{K_S^0K_S^0}$
α	-0.001	-0.001	0.000	-0.165	0.112	0.062
A_{bkg}		-0.110	-0.060	0.001	-0.001	-0.000
$A_{K_S^0\pi\pi}$			-0.036	0.001	-0.002	0.001
$A_{K_S^0K_S^0}$				0.000	0.001	-0.002
N_{bkg}					-0.126	-0.069
$N_{K_S^0\pi\pi}$						-0.028
$N_{K_S^0K_S^0}$						

Table A.1: Correlation matrix from the $K_S^0K_S^0$ fit to the (top) Belle and (bottom) Belle II simulation.

	A_{bkg}	$A_{K^0_S\pi\pi}$	$A_{K^0_S K^0_S}$	N_{bkg}	$N_{K^0_S\pi\pi}$	$N_{K^0_S K^0_S}$
α	0.001	0.001	-0.002	-0.145	0.094	0.050
A_{bkg}		-0.092	-0.048	-0.000	-0.001	0.002
$A_{K^0_S\pi\pi}$			-0.074	-0.002	0.001	0.001
$A_{K^0_S K^0_S}$				0.002	0.001	-0.005
N_{bkg}					-0.104	-0.054
$N_{K^0_S\pi\pi}$						
$N_{K^0_S K^0_S}$						

	A_{bkg}	$A_{K^0_S\pi\pi}$	$A_{K^0_S K^0_S}$	N_{bkg}	$N_{K^0_S\pi\pi}$	$N_{K^0_S K^0_S}$
α	0.000	-0.001	0.002	-0.164	0.128	0.050
A_{bkg}		-0.123	-0.048	0.000	0.001	-0.001
$A_{K^0_S\pi\pi}$			-0.038	0.001	-0.002	0.001
$A_{K^0_S K^0_S}$				-0.002	0.000	0.003
N_{bkg}					-0.141	-0.056
$N_{K^0_S\pi\pi}$						-0.031
$N_{K^0_S K^0_S}$						

Table A.2: Correlation matrix from the $K^0_S K^0_S$ fit to the (top) Belle and (bottom) Belle II data.

	A	A_{Ds}	A_{comb}	A_{kpi_rnd}	A_{kpi}	A_{mult_rnd}	A_{mult}	A_{sig_rnd}	A_{sig}	C	N_{comb}	N_{ds_peak}	N_{kpi_peak}	N_{kpi_rnd}	N_{mult_peak}	N_{mult_rnd}	N_{sig_peak}	N_{sig_rnd}	c_{comb}
A_{Ds}	0.001																		
A_{comb}	-0.004	-0.128																	
A_{kpi_rnd}	0.003	0.125	-0.770																
A_{kpi}	0.001	0.000	-0.011	-0.045															
A_{mult_rnd}	-0.071	-0.090	-0.682	0.487	0.021														
A_{mult}	-0.012	0.052	-0.059	0.042	-0.031	-0.402													
A_{sig_rnd}	0.001	0.070	-0.259	0.209	0.003	0.104	0.026												
A_{sig}	0.000	-0.001	-0.008	0.007	-0.003	0.020	-0.041	-0.052											
C	0.781	-0.001	0.001	-0.000	-0.000	0.037	0.003	-0.001	0.000										
N_{comb}	-0.107	-0.004	-0.001	-0.025	-0.000	-0.248	-0.001	-0.000	-0.000	0.055									
N_{ds_peak}	0.004	0.011	-0.002	0.005	0.000	0.015	-0.002	0.000	0.000	-0.009	-0.187								
N_{kpi_peak}	0.078	0.000	-0.001	-0.001	0.001	-0.003	-0.001	0.000	0.000	-0.047	-0.013	-0.001							
N_{kpi_rnd}	-0.013	0.001	0.005	0.053	0.000	0.032	0.001	-0.001	-0.000	0.009	-0.415	0.066	-0.040						
N_{mult_peak}	0.587	-0.001	-0.007	0.006	0.000	-0.111	-0.019	0.001	0.000	-0.279	-0.131	0.044	0.028	0.012					
N_{mult_rnd}	-0.237	0.003	0.003	0.004	-0.000	0.322	0.012	0.000	-0.000	0.111	-0.751	0.035	-0.013	0.109	-0.373				
N_{sig_peak}	0.027	0.000	-0.000	0.000	0.000	0.004	-0.000	0.000	0.000	-0.018	-0.014	0.000	-0.001	0.005	-0.014	0.012			
N_{sig_rnd}	-0.054	0.002	-0.001	0.009	-0.000	0.068	0.000	-0.003	-0.000	0.032	-0.297	0.093	-0.003	0.139	-0.011	0.202	-0.052		
c_{comb}	0.039	0.004	-0.004	-0.016	-0.000	0.223	0.001	0.001	0.000	-0.020	-0.554	0.149	-0.007	-0.336	0.060	0.665	0.007	0.166	

	A	A_{Ds}	A_{comb}	A_{kpi_rnd}	A_{kpi}	A_{mult}	A_{sig_rnd}	A_{sig}	C	N_{comb}	N_{ds_peak}	N_{kpi_peak}	N_{kpi_rnd}	N_{mult_peak}	N_{sig_peak}	N_{sig_rnd}	c_{comb}
A_{Ds}	−0.001																
A_{comb}	0.012	−0.214															
A_{kpi_rnd}	−0.005	0.141	−0.616														
A_{kpi}	0.004	0.004	−0.000	−0.082													
A_{mult}	−0.000	−0.008	−0.559	0.286	−0.025												
A_{sig_rnd}	−0.001	0.054	−0.215	0.134	0.003	0.058											
A_{sig}	0.000	0.002	0.011	−0.003	−0.007	−0.038	−0.083										
C	−0.747	0.002	−0.009	0.004	−0.002	0.005	0.001	−0.000									
N_{comb}	−0.463	0.021	−0.066	0.079	−0.008	0.023	0.012	−0.001	0.188								
N_{ds_peak}	0.006	−0.034	0.015	−0.014	0.001	−0.004	−0.003	0.000	−0.010	−0.191							
N_{kpi_peak}	0.094	0.001	−0.005	0.010	0.004	0.003	0.001	0.000	−0.042	−0.051	−0.001						
N_{kpi_rnd}	0.003	−0.027	0.113	−0.158	0.011	−0.052	−0.024	0.001	−0.003	−0.436	0.052	−0.059					
N_{mult_peak}	0.530	−0.005	0.022	−0.017	0.003	−0.001	−0.003	0.000	−0.210	−0.686	0.043	0.033	0.058				
N_{sig_peak}	0.038	0.000	0.000	−0.000	−0.000	−0.000	−0.000	−0.000	−0.015	−0.012	−0.000	−0.003	0.002	−0.007			
N_{sig_rnd}	−0.037	−0.006	0.015	−0.017	0.001	−0.006	0.001	0.001	0.010	−0.163	0.064	−0.004	0.087	0.036	−0.085		
c_{comb}	0.289	0.004	−0.038	0.062	−0.005	0.024	0.010	−0.000	−0.115	−0.243	0.157	0.001	−0.413	0.482	0.003	0.052	

Table A.3: Correlation matrix from the K^+K^- fit to the (top) Belle and (bottom) Belle II simulation.

	δ_{J_kpi}	$\delta_{J\_sig\_dz}$	γ_{J_kpi}	$\lambda_{J\_sig\_dz}$	μ_{J_kpi}	$\mu_{J\_sig\_d0pi}$	$\mu_{J\_sig\_dz}$	A	A_{Ds}	A_{comb}	A_{kpi_rnd}	A_{kpi}	A_{mult_rnd}	A_{mult}	A_{sig_rnd}	C	N_{comb}	N_{ds_peak}	N_{kpi_peak}	N_{kpi_rnd}	N_{mult_peak}	N_{mult_rnd}	N_{sig_peak}	N_{sig_rnd}	c_{comb}	f_{G_kpi}	
δ_{J_kpi}	-0.127																										
$\delta_{J\_sig\_dz}$	-0.691	0.090																									
γ_{J_kpi}	-0.739	0.087	0.823																								
$\lambda_{J\_sig\_dz}$	0.000	-0.004	-0.001	-0.000																							
μ_{J_kpi}	0.017	-0.047	-0.013	-0.013	0.001																						
$\mu_{J\_sig\_dz}$	-0.118	0.990	0.083	0.080	-0.004	-0.059																					
$\mu_{J\_sig\_d0pi}$	-0.033	-0.004	0.021	0.026	0.011	0.002	-0.003																				
A	-0.003	-0.020	0.003	0.003	-0.002	-0.001	-0.021	-0.005	0.114	-0.771																	
A_{Ds}	-0.000	0.004	0.000	0.000	0.001	-0.000	0.004	-0.000	0.001	-0.010	-0.042																
A_{comb}	-0.001	-0.022	0.006	0.003	-0.001	-0.001	-0.022	-0.018	-0.119	-0.708	0.506	0.019															
A_{kpi_rnd}	-0.003	0.005	0.003	0.003	-0.000	0.000	0.005	0.005	0.057	-0.067	0.045	-0.027	-0.421														
A_{kpi}	0.000	-0.008	0.000	-0.000	-0.001	-0.001	-0.008	-0.001	0.069	-0.255	0.209	0.003	0.106	0.012													
A_{mult_rnd}	-0.001	-0.002	0.001	0.001	0.000	0.000	-0.002	-0.000	-0.001	-0.007	0.007	-0.000	0.022	-0.045	-0.061												
A_{mult}	0.015	0.005	-0.010	-0.012	-0.020	-0.000	0.005	-0.703	-0.001	-0.004	0.004	0.000	0.007	-0.002	0.001	0.000											
A_{sig_rnd}	0.088	0.052	-0.077	-0.074	-0.002	-0.002	0.042	-0.134	0.003	-0.013	-0.011	-0.002	-0.062	-0.007	-0.002	-0.000	0.029										
C	-0.019	-0.004	0.021	0.019	0.001	-0.003	-0.001	-0.006	-0.029	-0.003	0.005	0.002	0.005	-0.001	0.001	-0.000	0.008	-0.178									
N_{comb}	0.151	0.021	0.114	0.117	0.006	-0.003	0.020	0.064	0.000	0.002	-0.003	0.000	-0.002	0.001	-0.000	0.000	-0.023	-0.027	0.003								
N_{kpi_peak}	-0.105	-0.042	0.014	0.059	-0.001	0.001	-0.039	-0.003	-0.002	0.023	0.027	0.005	-0.008	-0.002	-0.004	0.000	0.003	-0.388	0.066	-0.019							
N_{mult_peak}	0.029	0.035	-0.025	-0.022	-0.003	0.006	0.031	0.497	-0.004	0.001	-0.002	0.001	-0.027	0.004	-0.000	0.000	-0.105	-0.182	0.048	0.014	0.014						
N_{sig_peak}	0.050	-0.070	-0.040	-0.038	0.005	-0.001	-0.063	0.026	0.000	-0.002	0.003	0.000	0.003	-0.000	-0.000	-0.001	-0.012	-0.016	0.002	-0.007	0.010	-0.020	0.014				
N_{sig_rnd}	-0.022	-0.027	0.021	0.020	-0.007	-0.007	-0.013	-0.059	-0.003	0.005	0.002	0.001	0.016	0.000	0.006	0.000	0.023	-0.284	0.092	0.001	0.130	-0.023	0.192	-0.055			
c_{comb}	0.87229	0.017	-0.015	0.067	0.017	0.002	-0.001	-0.009	0.055	-0.002	-0.009	-0.010	-0.002	0.069	0.007	0.005	-0.000	-0.008	-0.529	0.136	-0.008	-0.389	0.100	0.649	0.005	0.151	
f_{G_kpi}	0.79628	0.579	-0.082	-0.396	-0.145	0.000	0.010	-0.077	-0.020	0.000	-0.004	-0.001	-0.001	0.003	-0.001	0.001	-0.000	0.008	0.041	-0.005	-0.088	-0.090	0.015	-0.005	0.031	-0.009	0.052

	γ_{J_kpi}	λ_{J_kpi}	$\lambda_{J\_sig\_d0pi}$	$\lambda_{J\_sig\_dz}$	$\mu_{G1\_sig\_d0pi}$	μ_{G_kpi}	A	A_{Ds}	A_{comb}	A_{kpi_rnd}	A_{kpi}	A_{mult_rnd}	A_{mult}	A_{sig_rnd}	A_{sig}	C	N_{comb}	N_{ds_peak}	N_{kpi_peak}	N_{kpi_peak}	N_{kpi_rnd}	.N_{mult_peak}	N_{mult_rnd}	N_{sig_peak}	N_{sig_rnd}	c_{comb}
λ_{J_kpi}	0.209																									
$\lambda_{J\_sig\_d0pi}$	0.012	0.030																								
$\lambda_{J\_sig\_dz}$	−0.032	−0.033	0.031																							
$\mu_{G1\_sig\_d0pi}$	−0.001	0.002	0.056	0.002																						
μ_{G_kpi}	−0.001	0.364	−0.000	−0.014	−0.001																					
A	−0.018	0.012	0.069	0.004	0.075	−0.001																				
A_{Ds}	−0.003	−0.001	0.000	−0.002	−0.001	0.001	0.008																			
A_{comb}	−0.037	−0.005	−0.003	−0.013	−0.003	−0.000	0.033	−0.063																		
A_{kpi_rnd}	0.014	0.013	0.002	0.013	0.001	0.004	−0.019	0.065	−0.680																	
A_{kpi}	0.003	0.006	0.003	0.001	0.001	−0.000	0.001	0.000	−0.025	−0.063																
A_{mult_rnd}	0.069	0.018	0.004	0.038	0.007	−0.007	−0.095	−0.124	−0.666	0.418	0.033															
A_{mult}	−0.015	−0.003	0.001	−0.012	−0.005	0.003	0.039	0.055	−0.004	0.000	−0.038	−0.479														
A_{sig_rnd}	0.005	0.001	0.001	0.003	−0.004	0.000	−0.001	0.044	−0.192	0.138	0.006	0.060	0.014													
A_{sig}	0.003	0.002	−0.000	0.002	0.002	0.000	−0.002	−0.002	−0.011	0.009	−0.007	0.026	−0.049	−0.090												
C	−0.001	−0.004	−0.014	−0.003	−0.151	−0.000	−0.656	0.003	0.001	0.000	−0.001	−0.007	0.011	0.002	−0.001											
N_{comb}	−0.063	−0.056	−0.024	−0.084	0.002	0.014	−0.058	0.027	0.167	−0.160	−0.011	−0.445	0.115	−0.029	−0.007	0.000										
N_{ds_peak}	0.015	0.006	0.001	0.019	−0.000	−0.004	−0.000	0.020	−0.008	0.013	0.000	0.016	−0.003	0.005	0.000	0.001	−0.141									
N_{kpi_peak}	0.072	0.099	0.078	−0.007	0.029	0.014	0.079	0.001	−0.002	−0.002	0.006	−0.002	0.004	0.001	0.000	−0.012	−0.019	−0.000								
N_{kpi_rnd}	−0.084	0.075	−0.037	0.037	−0.027	0.006	−0.037	−0.008	0.011	0.111	0.003	0.062	−0.023	0.000	0.001	0.008	−0.393	0.055	−0.074							
N_{mult_peak}	−0.057	−0.034	0.001	−0.031	−0.024	−0.005	0.440	0.017	0.073	−0.041	−0.004	−0.201	0.082	−0.001	−0.005	0.004	−0.065	0.040	0.016	−0.003						
N_{mult_rnd}	0.111	0.036	0.007	0.068	0.010	−0.015	−0.185	−0.038	−0.216	0.156	0.011	0.555	−0.159	0.028	0.010	−0.000	−0.800	0.026	−0.005	0.153	−0.378					
N_{sig_peak}	−0.034	−0.032	0.049	0.049	0.023	−0.009	0.035	−0.001	−0.003	0.003	−0.000	0.008	−0.003	−0.000	−0.000	−0.007	−0.019	0.001	−0.004	0.005	−0.016	0.014				
N_{sig_rnd}	0.018	0.011	−0.053	0.096	−0.044	−0.005	−0.076	−0.006	−0.041	0.041	0.002	0.111	−0.030	0.025	0.003	0.011	−0.260	0.067	−0.010	0.121	−0.040	0.200	−0.086			
c_{comb}	0.164	0.002	0.004	0.055	−0.001	−0.023	0.004	−0.024	−0.186	0.098	0.006	0.436	−0.112	0.029	0.007	0.002	−0.687	0.126	−0.003	−0.157	0.002	0.753	0.009	0.185		

Table A.4: Correlation matrix from the K^+K^- fit to the (top) Belle and (bottom) Belle II data.

Appendix B

Shapes of $D^0/\overline{D}^0$ samples

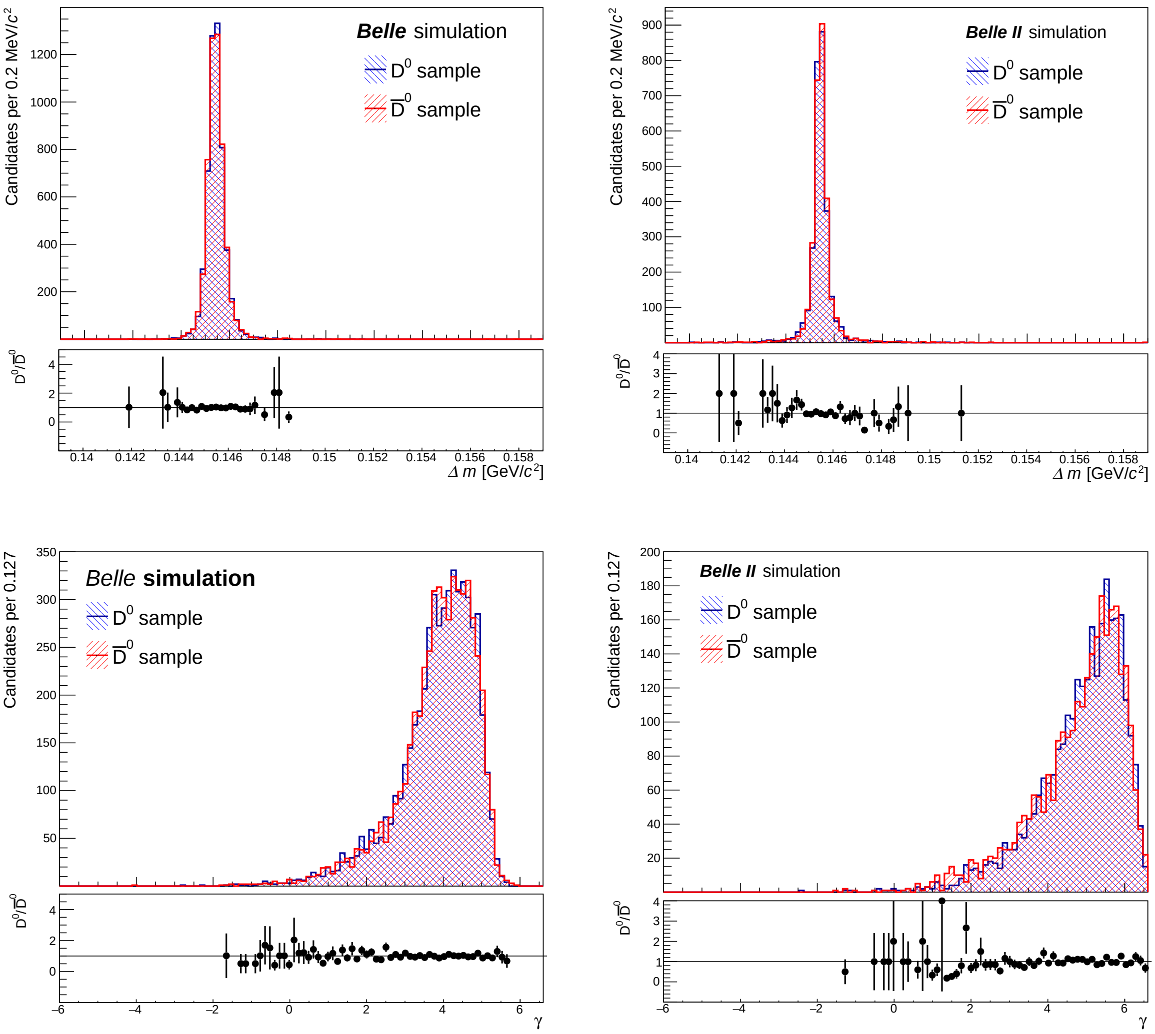

Figure B.1: Overlapping distributions of Δm (top) and γ (bottom), for the signal component, for Belle (left) and Belle II (right) simulation. The D^0 samples are shown in blue and the $\overline{D}^0$ samples are shown in red. The ratio for the two samples are also shown in the bottom panel of each plot.

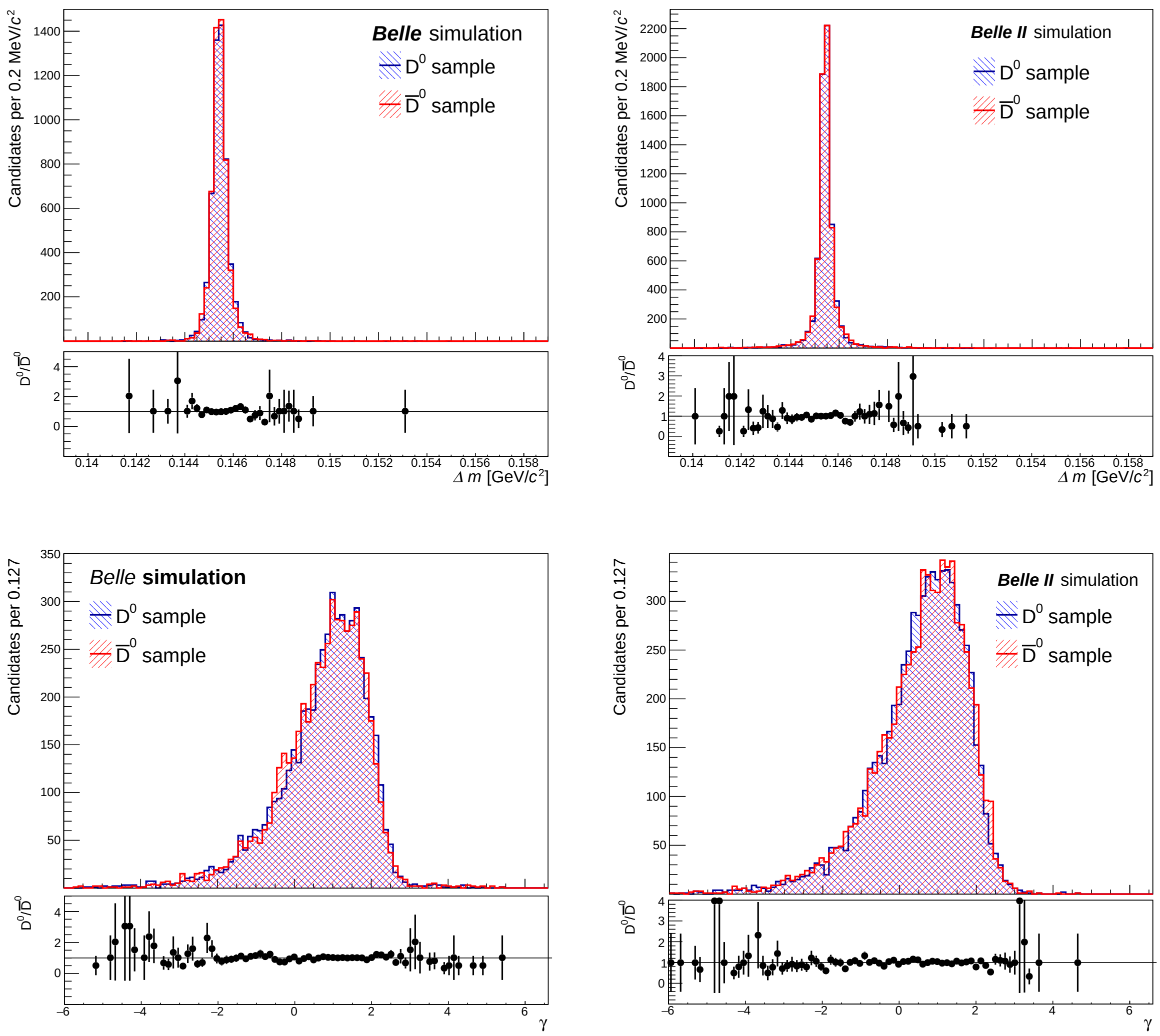

Figure B.2: Overlapping distributions of Δm (top) and γ (bottom), corresponding to the $D^0 \to K_S^0\pi\pi$ component, for Belle (left) and Belle II (right) simulation. The D^0 samples are shown in blue and the $\overline{D}^0$ samples are shown in red. The ratio for the two samples are also shown in the bottom panel of each plot.

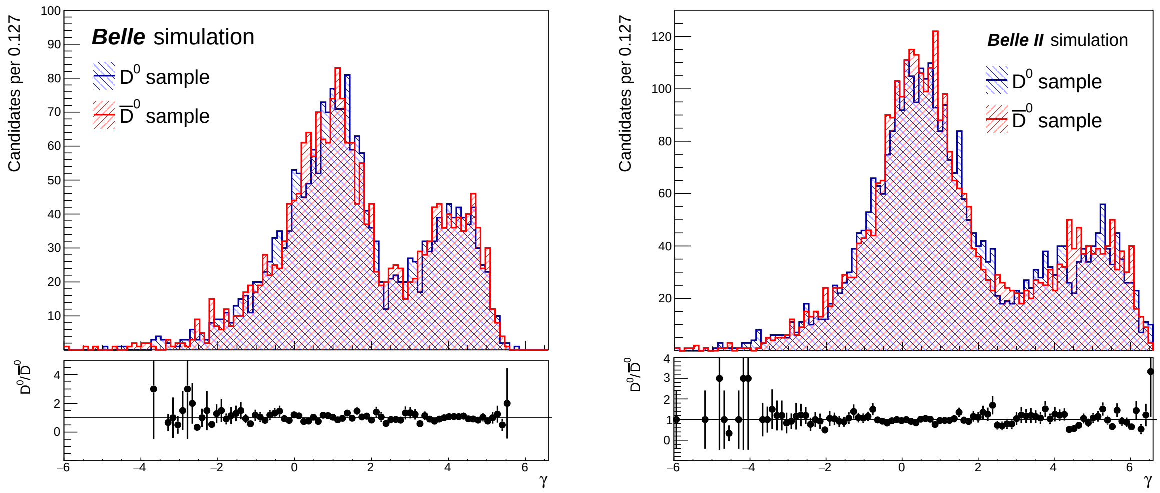

Figure B.3: Overlapping distributions of γ, for the non-peaking component, for Belle (left) and Belle II (right) simulation. The ratio for the two samples are also shown in the bottom panel of each plot.

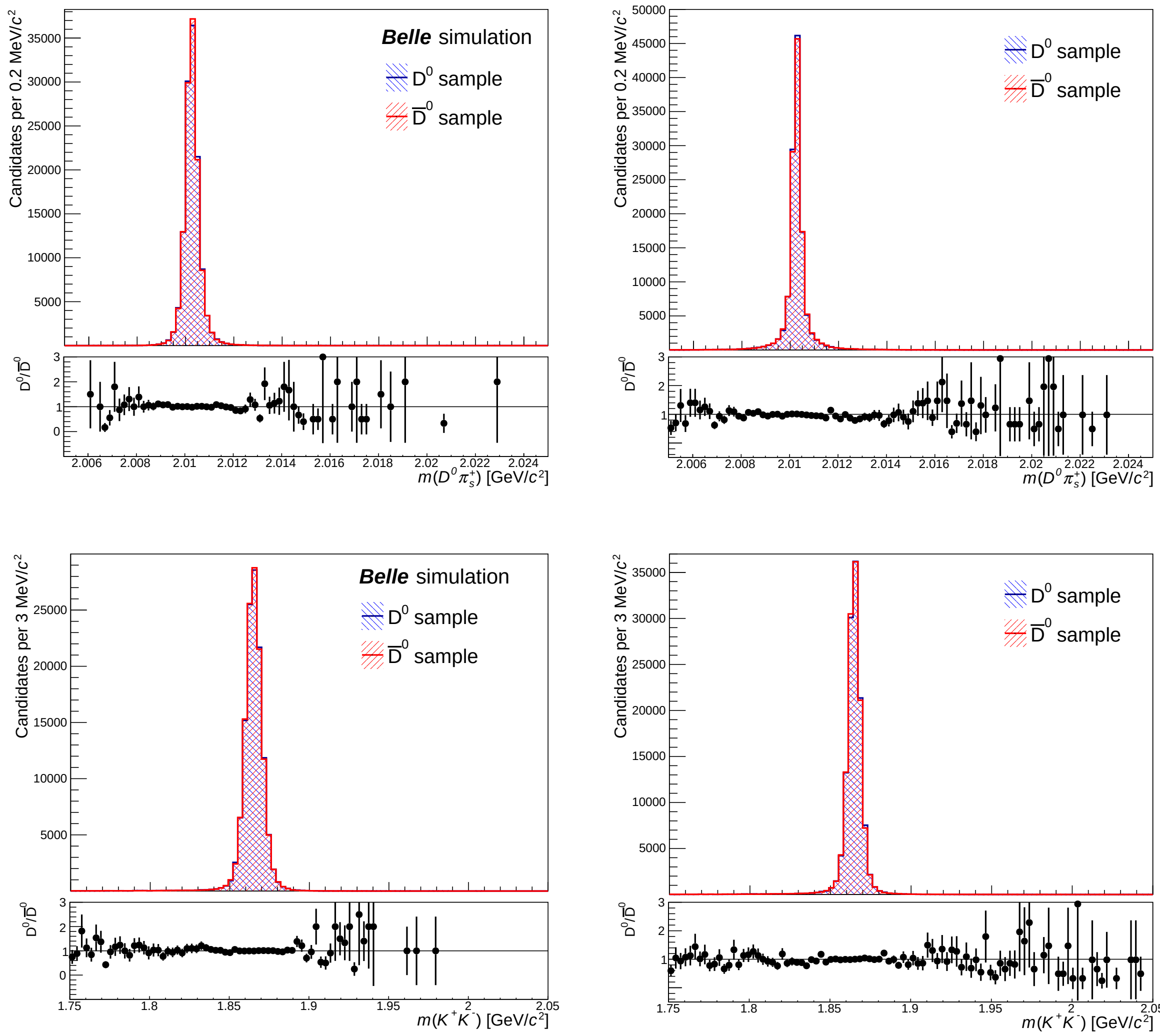

Figure B.4: Overlapping distributions of $m(D^0\pi_s)$ (top) and $m(K^+K^-)$ (bottom), corresponding to the signal component for Belle (left) and Belle II (right) simulation. The D^0 samples are shown in blue and the $\overline{D}^0$ samples are shown in red. The ratio for the two samples are also shown in the bottom panel of each plot.

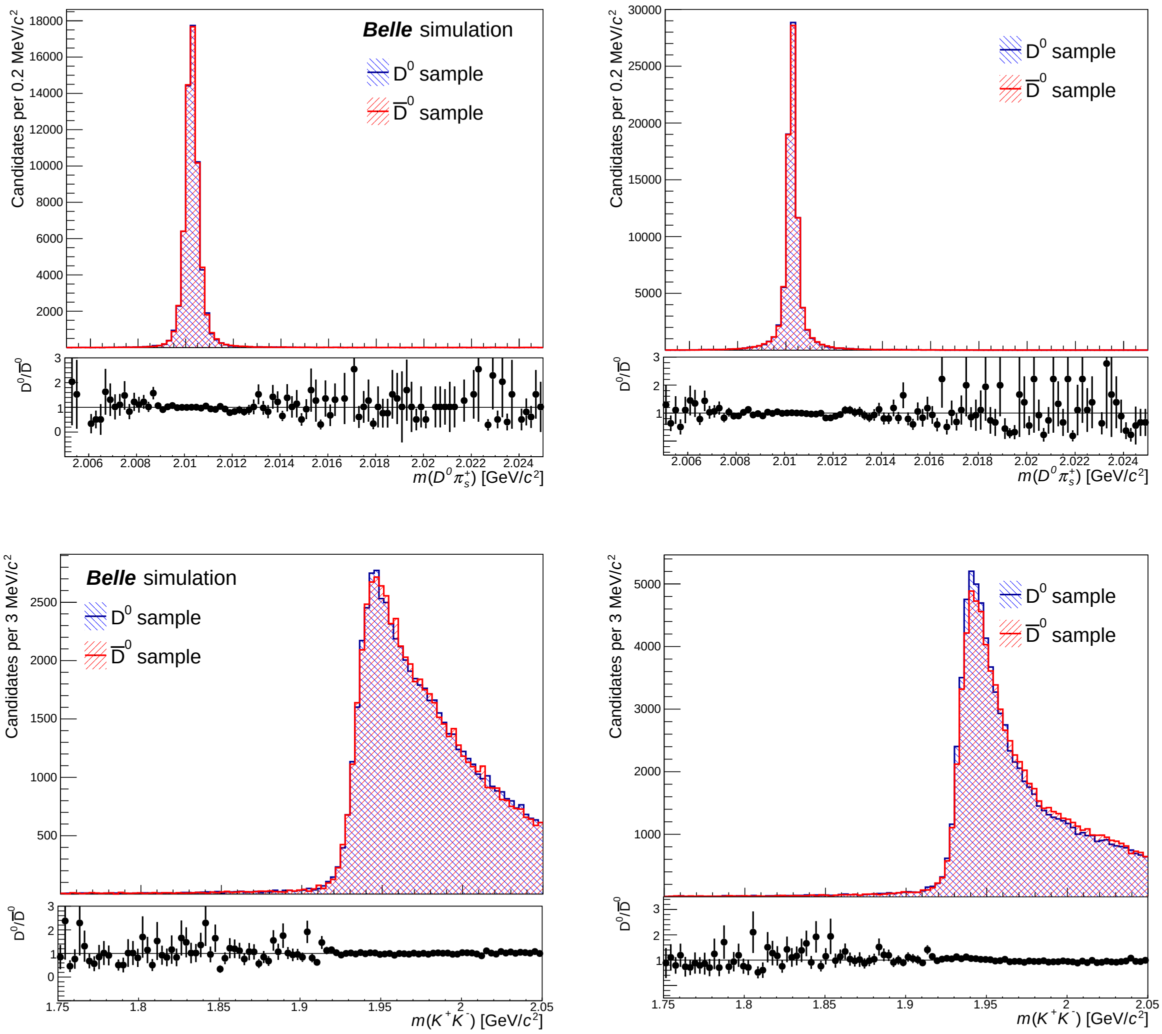

Figure B.5: Overlapping distributions of $m(D^0\pi_s)$ (left) and $m(K^+K^-)$ (right), corresponding to the Kπ background component for Belle (left) and Belle II (right) simulation. The D^0 samples are shown in blue and the $\overline{D}^0$ samples are shown in red. The ratio for the two samples are also shown in the bottom panel of each plot.

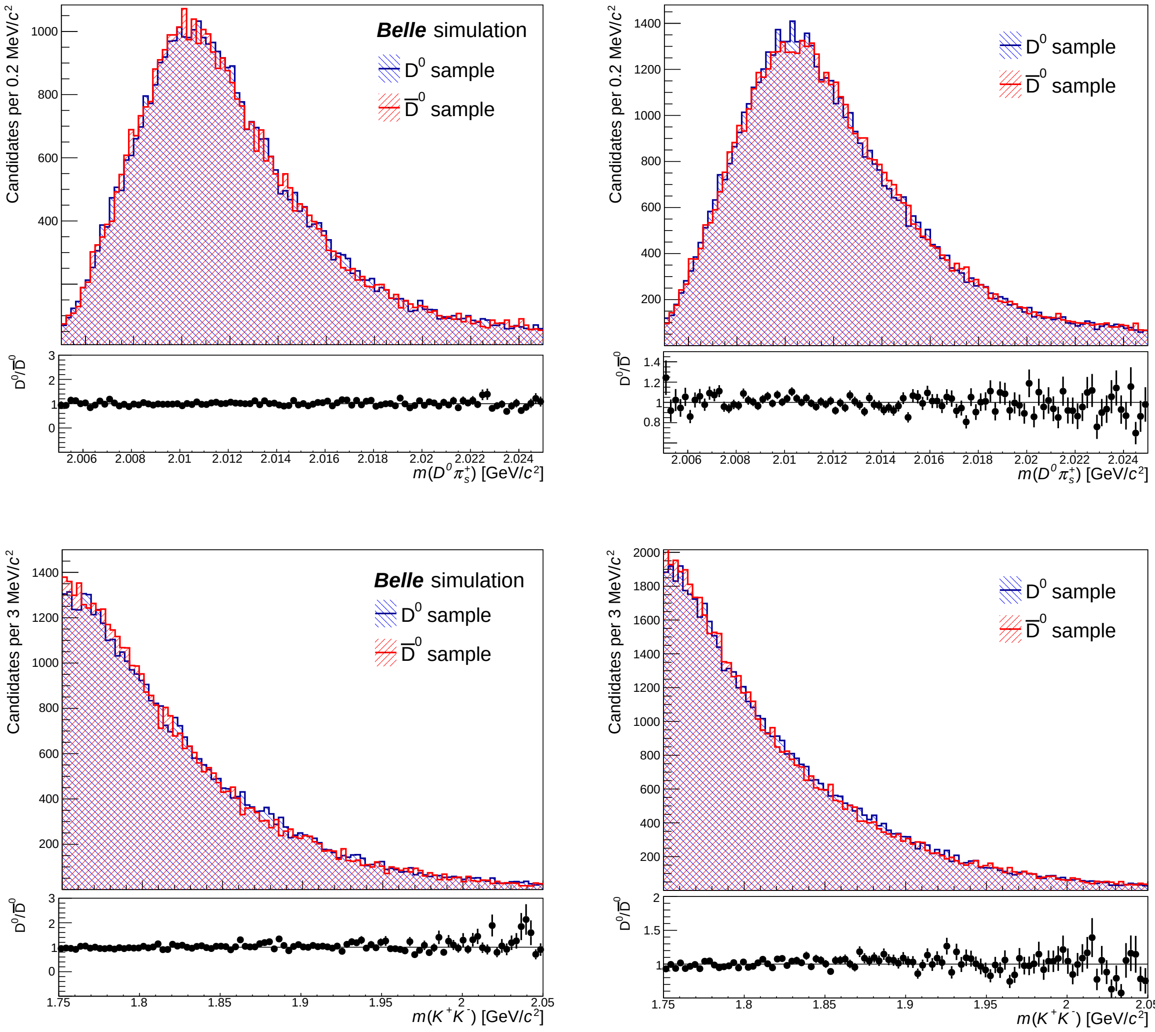

Figure B.6: Overlapping distributions of $m(D^0\pi_s)$ (left) and $m(K^+K^-)$ (right), corresponding to the multibody background component for Belle (left) and Belle II (right) simulation. The D^0 samples are shown in blue and the $\overline{D}^0$ samples are shown in red. The ratio for the two samples are also shown in the bottom panel of each plot.

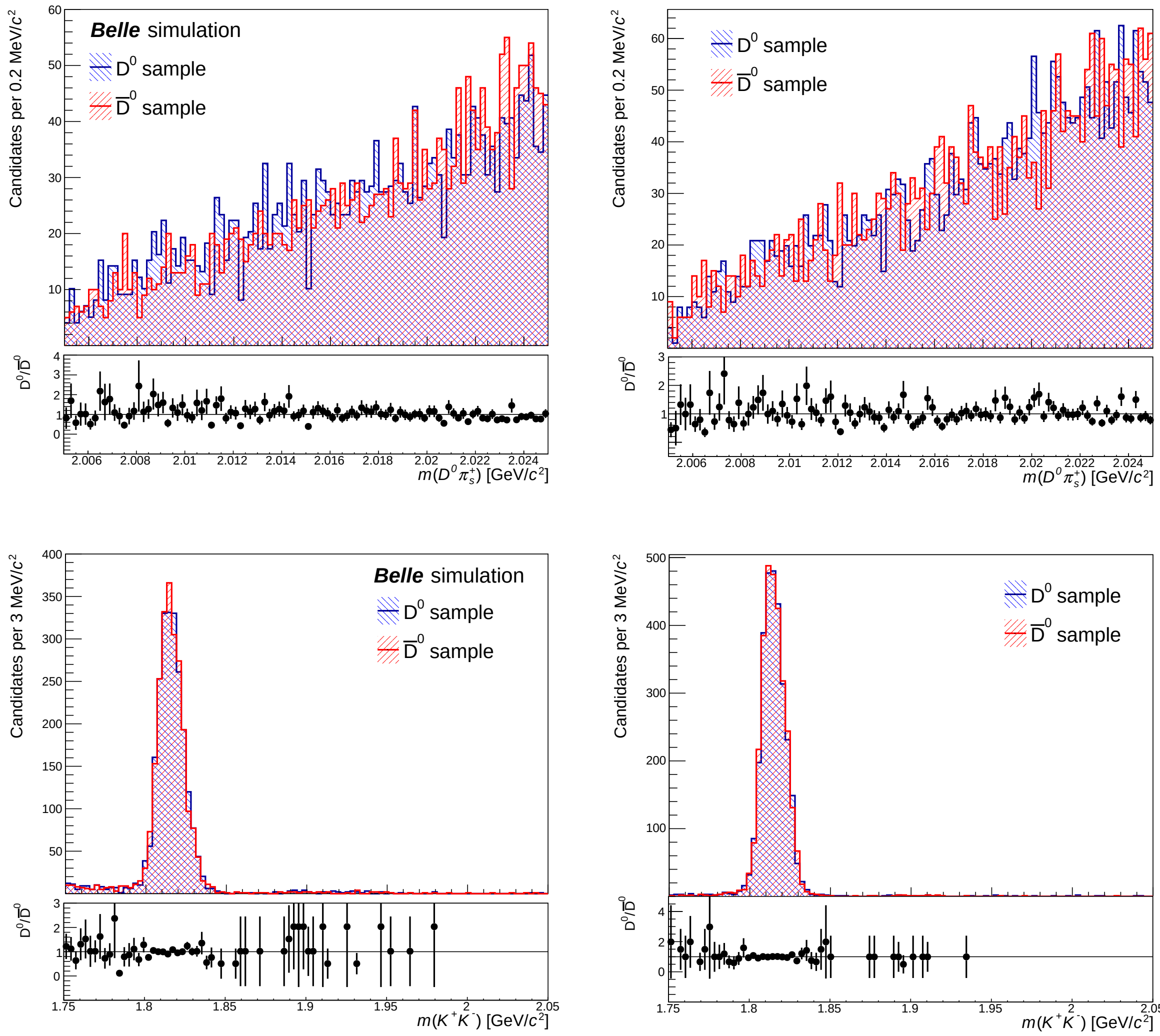

Figure B.7: Overlapping distributions of $m(D^0\pi_s)$ (left) and $m(K^+K^-)$ (right), corresponding to the D_s background component for Belle (left) and Belle II (right) simulation.. The D^0 samples are shown in blue and the $\overline{D}^0$ samples are shown in red. The ratio for the two samples are also shown in the bottom panel of each plot.

Appendix C

Results with $p_{\text{cms}}(D^{*+}) > 2.2\,\text{GeV}/c$

The results of the $D^0 \to K_S^0 K_S^0$ fit to the data selected with the looser $p_{\text{cms}}(D^{*+})$ requirement are shown in Figures C.1 and C.2. The measured yields for $D^0 \to K_S^0 K_S^0$ are 5483 ± 83 in Belle and 2508 ± 55 in Belle II. The corresponding raw asymmetry is measured to be $(2.1 \pm 1.5)\%$ in Belle and $(2.1 \pm 2.2)\%$ in Belle II, in agreement between the two samples. The complete set of measured fit parameters for $D^0 \to K_S^0 K_S^0$ are tabulated in Table C.1.

$$\mathcal{A}_{CP}(D^0 \to K_S^0 K_S^0) \text{ in Belle} = (1.89 \pm 1.53)\% \text{ (blind) and} \tag{C.1}$$

$$\mathcal{A}_{CP}(D^0 \to K_S^0 K_S^0) \text{ in Belle II} = (1.47 \pm 2.19)\% \text{ (blind)}\,, \tag{C.2}$$

Combining the Belle and Belle II results, following Equation (3.4), we obtain

$$\mathcal{A}_{CP}(D^0 \to K_S^0 K_S^0) = (1.75 \pm 1.25)\% \text{ (blind)}\,. \tag{C.3}$$

When rounding the uncertainty, the final statistical precision is the same as that using the tighter $p_{\text{cms}}(D^{*+}) > 2.5\,\text{GeV}/c$ requirement.

Fit parameter	Measured value	Raw asymmetry (%)
$N^{K_S^0 K_S^0}$	5483 ± 83	2.1 ± 1.5
$N^{K_S^0 \pi\pi}$	16915 ± 141	-1.04 ± 0.83
N^{bkg}	16344 ± 141	-0.94 ± 0.84
α	-22.66 ± 0.89	-
$N^{K_S^0 K_S^0}$	2508 ± 55	1.6 ± 2.2
$N^{K_S^0 \pi\pi}$	6575 ± 90	-1.6 ± 1.3
N^{bkg}	8707 ± 102	2.2 ± 1.2
α	-24.53 ± 1.2	-

Table C.1: Measured values of the parameters obtained from the fit to $D^0 \to K_S^0 K_S^0$ sample in (top) Belle and (bottom) Belle II data. The uncertainties are statistical only.

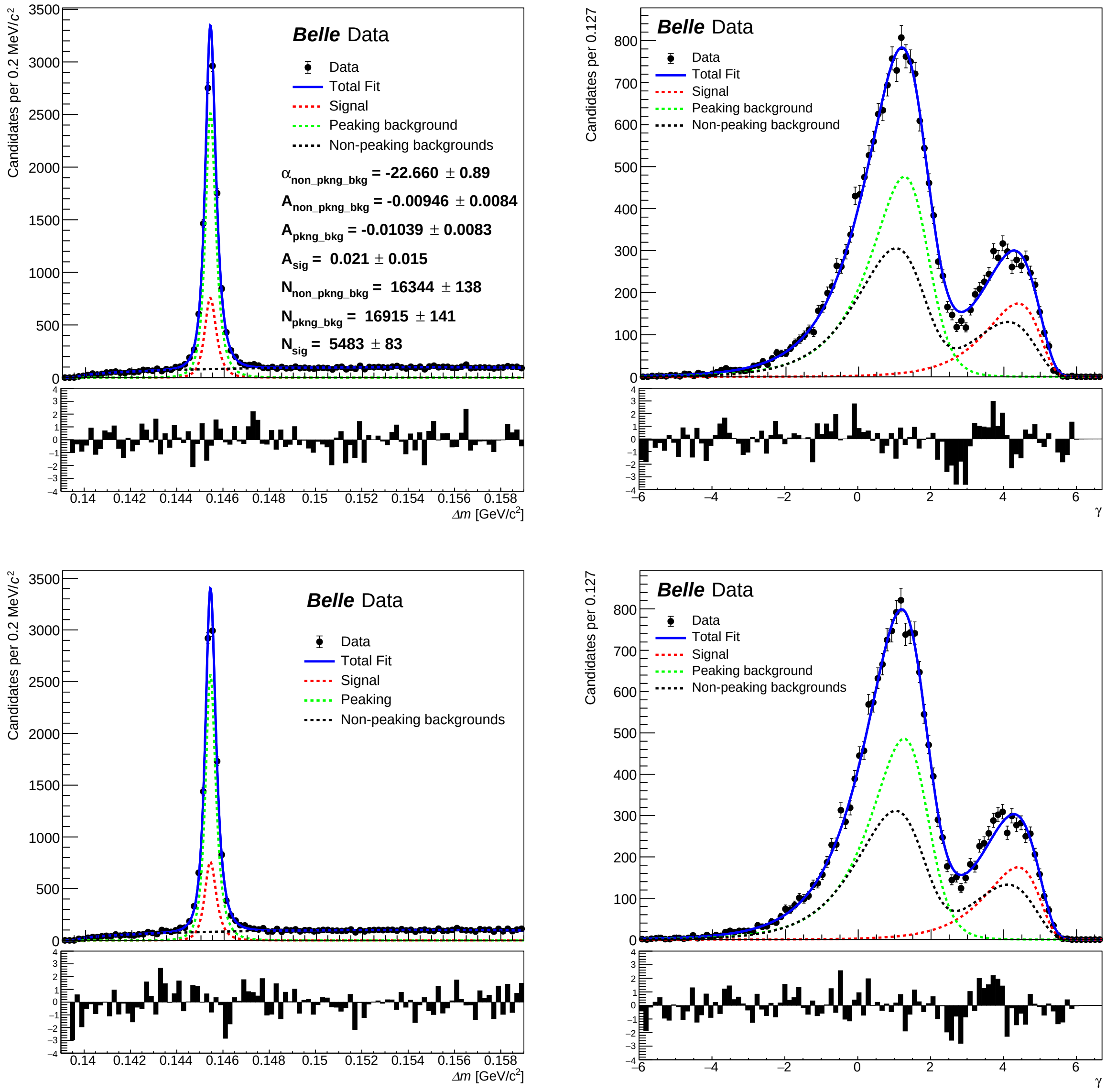

Figure C.1: Distributions of (left) Δm and (right) γ for (top) $D^0 \to K^0_S K^0_S$ and (bottom) $\bar{D}^0 \to K^0_S K^0_S$ candidates in Belle data, with $p_{\rm cms}(D^{*+}) > 2.2\,{\rm GeV}/c$ and fit projections overlaid. The normalized residuals (pulls) are shown in the bottom panel of each plot.

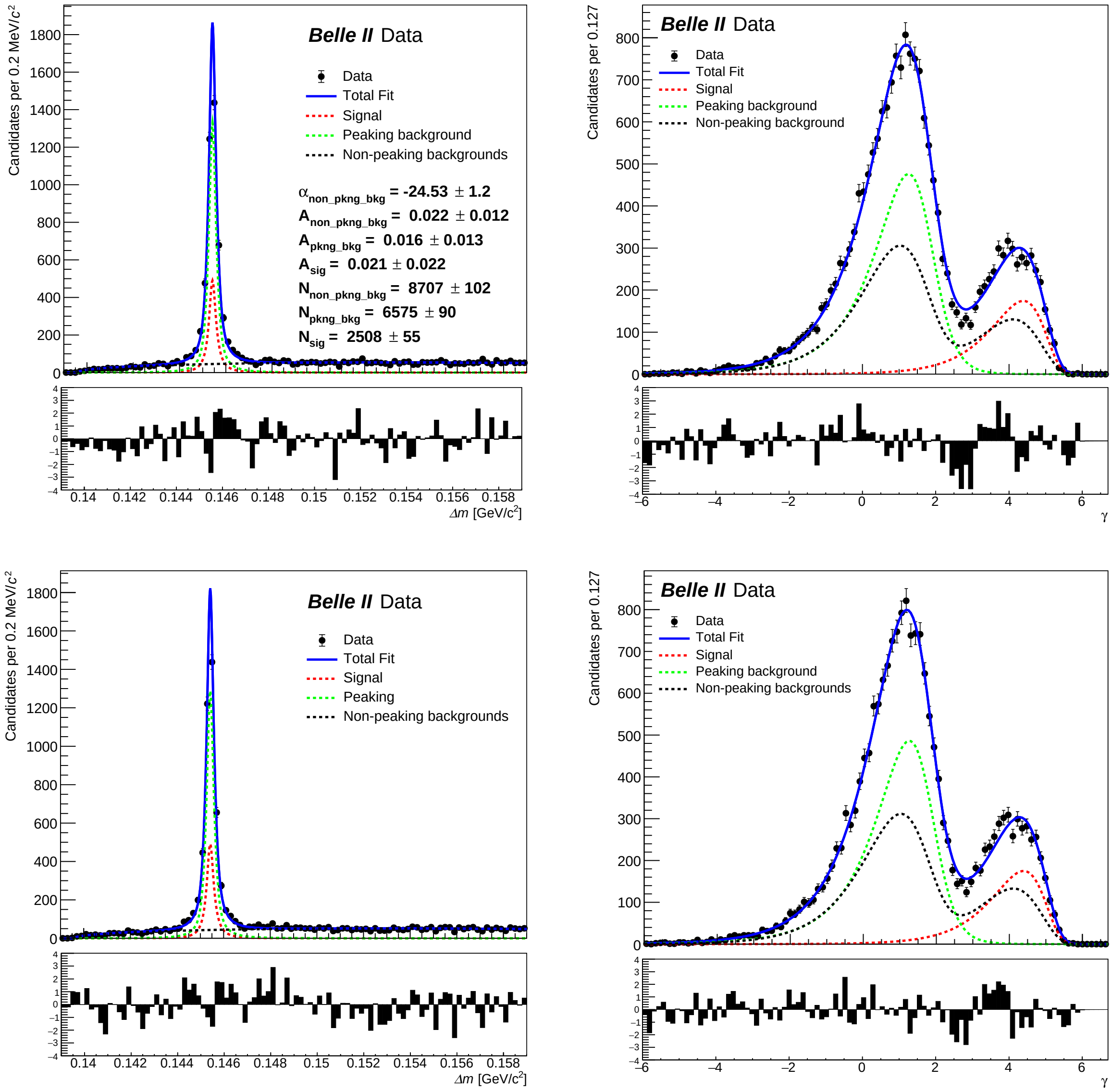

Figure C.2: Distributions of (left) Δm and (right) γ for (top) $D^0 \to K^0_S K^0_S$ and (bottom) $\overline{D}^0 \to K^0_S K^0_S$ candidates in Belle II data, with $p_{\text{cms}}(D^{*+}) > 2.2\,\text{GeV}/c$ and fit projection overlaid. The normalized residuals (pulls) are shown in the bottom panel of each plot.

The results of the $D^0 \to K^+K^-$ fit to Belle and Belle II data are shown in Figures C.3 and C.4. The complete set of measured fit parameters for $D^0 \to K^+K^-$ are tabulated in Table C.2 and Table C.3.

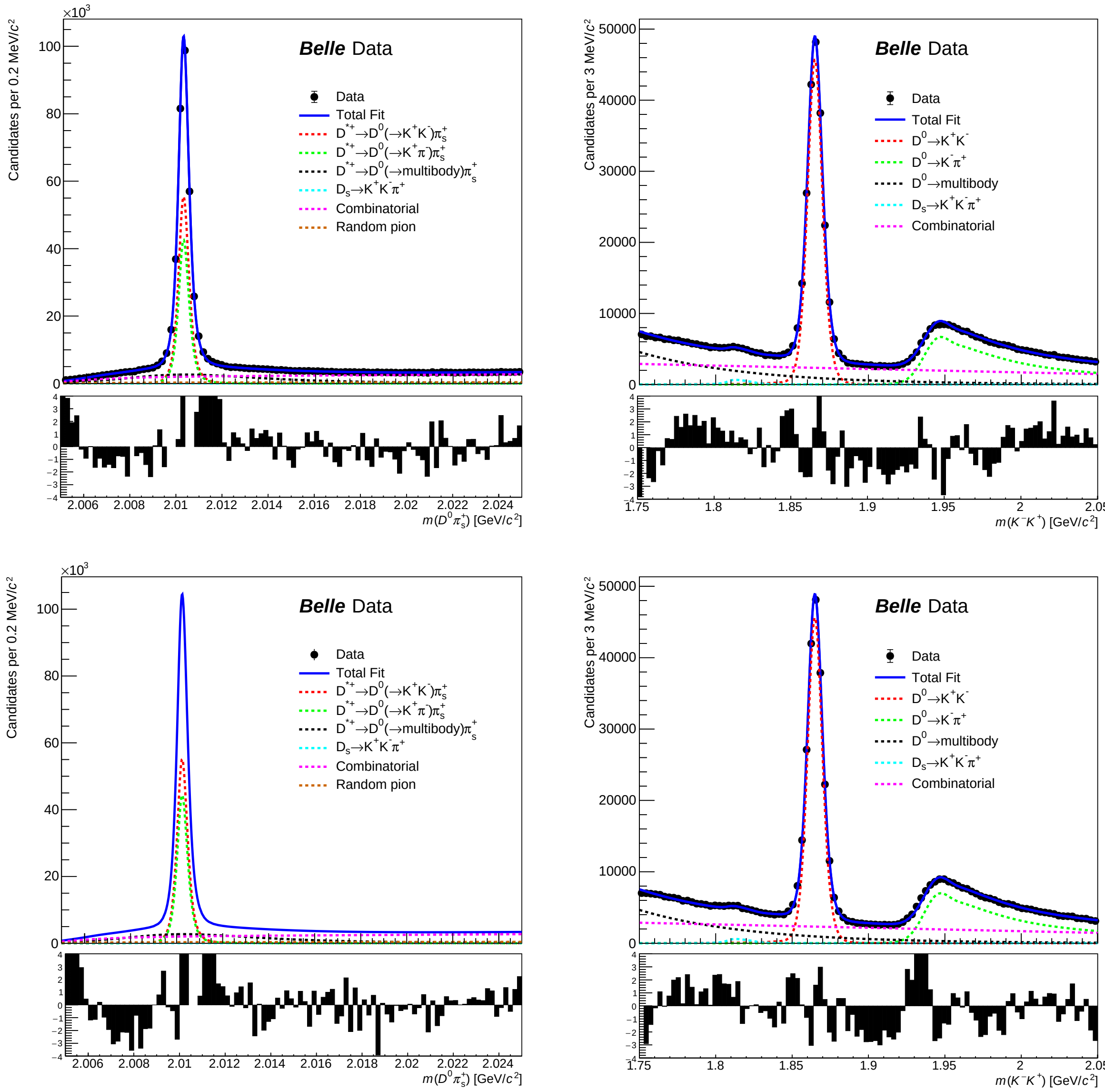

Figure C.3: Distributions of (left) $m(D^0\pi_s)$ and (right) $m(K^+K^-)$ for (top) $D^{*+} \to D^0(\to K^+K^-)\pi^+$ and (bottom) $D^{*-} \to \overline{D}^0(\to K^+K^-)\pi^-$ in Belle data, with fit $p_{\rm cms}(D^{*+}) > 2.2$ GeV/c and projections overlaid. The normalized residuals (pulls) are also shown in the bottom panel of each plot.

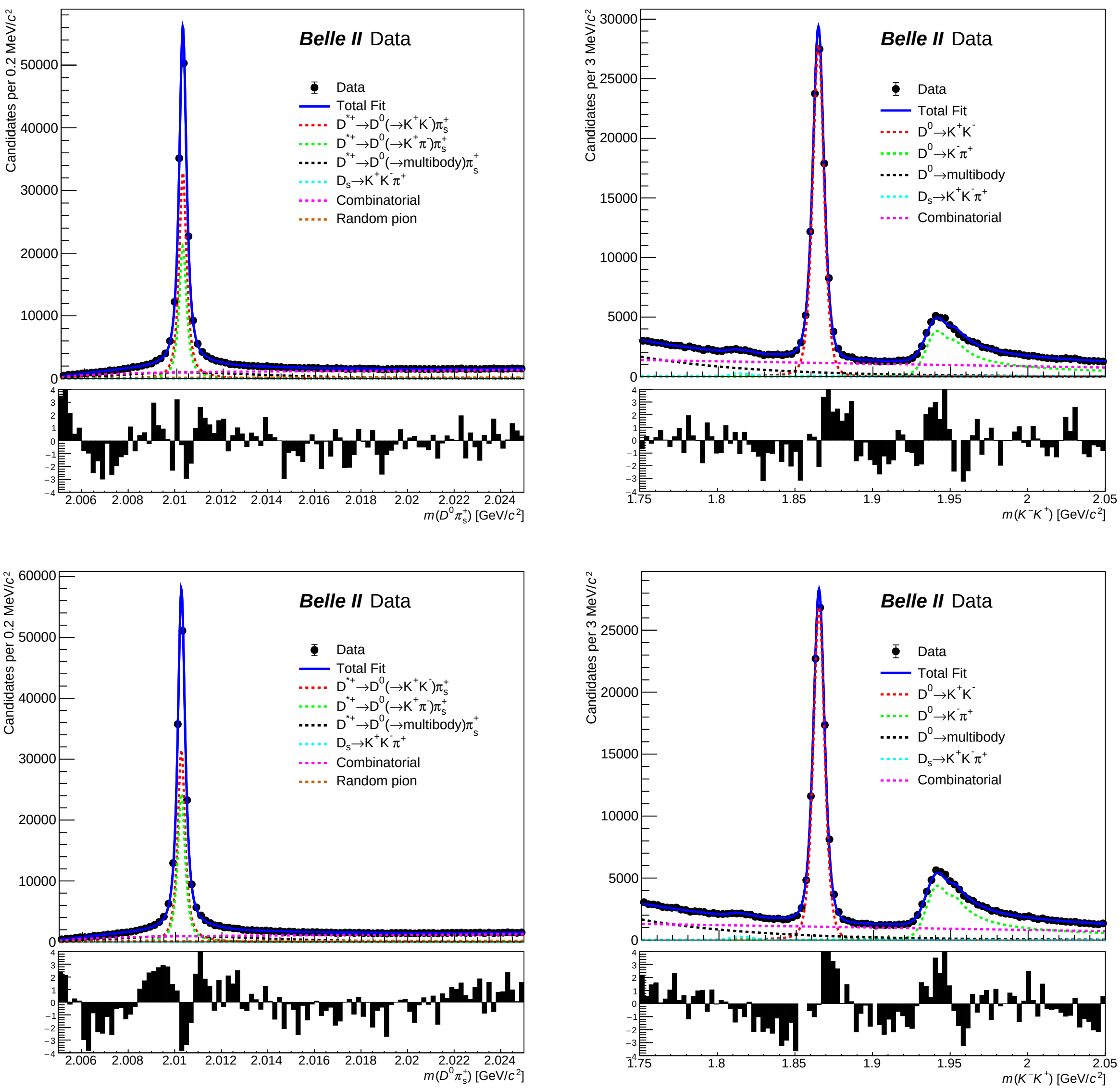

Figure C.4: Distributions of (left) $m(D^0\pi_s)$ and (right) $m(K^+K^-)$ for (top) $D^{*+} \to D^0(\to K^+K^-)\pi^+$ and (bottom) $D^{*-} \to \overline{D}^0(\to K^+K^-)\pi^-$ in Belle data, with fit projections overlaid. The normalized residuals (pulls) are also shown in the bottom panel of each plot.

Fit parameter	Measured value	Raw asymmetry (%)
$N^{K^+K^-}$	354363 ± 619	0.23 ± 0.17
$N^{K^+K^-\,\mathrm{rnd}}$	37557 ± 325	1.06 ± 0.86
$N^{K\pi}$	278737 ± 562	-2.01 ± 0.21
$N^{K\pi\,\mathrm{rnd}}$	25366 ± 764	-5.52 ± 2.3
N^{mult}	219117 ± 1147	1.05 ± 0.39
$N^{\mathrm{mult\ rnd}}$	0	0
$N^{D_s^+}$	8796 ± 275	4.9 ± 2.9
N^{comb}	433807 ± 1580	0.74 ± 0.61
A	31.9 ± 1.4	-
C	0.002169 ± 0.000042	-
c_{comb}	-0.3289 ± 0.0048	-
$\mu_{\mathrm{J\_sig\_d0pi}}$	$2.01020968 \pm 0.000000082$	-
$\mu_{\mathrm{J\_sig\_d0}}$	1.86439 ± 0.0000094	-
$\lambda_{\mathrm{J\_sig\_d0}}$	0.01120 ± 0.000014	-
$\delta_{\mathrm{J\_sig\_d0}}$	2.222 ± 0.025	-
$\mu_{\mathrm{J\_kpi\_d0}}$	1.95850 ± 0.00022	-
$\delta_{\mathrm{J\_kpi\_d0}}$	0.5712 ± 0.0077	-

Table C.2: .
Measured values of the parameters obtained from the fit to $D^0 \to K^+K^-$ sample in Belle data with $p_{\mathrm{cms}}(D^{*+}) > 2.2\,\mathrm{GeV}/c$. The uncertainties are statistical only.

Fit parameter	Measured value	Raw asymmetry (%)
$N^{K^+K^-}$	166157 ± 45	2.03 ± 0.26
$N^{K^+K^-\,\mathrm{rnd}}$	17055 ± 222	-0.85 ± 1.3
$N^{K\pi}$	117582 ± 387	-6.94 ± 0.32
$N^{K\pi\,\mathrm{rnd}}$	10881 ± 391	-4.91 ± 3.4
N^{mult}	80329 ± 775	0.75 ± 0.68
$N^{\mathrm{mult\ rnd}}$	0	0
$N^{D_s^+}$	3226 ± 152	-0.26 ± 4.4
N^{comb}	208047 ± 1019	3.46 ± 0.41
A	26.4 ± 2.4	-
C	0.002314 ± 0.000073	-
c_{comb}	-0.2916 ± 0.0061	-
$\mu_{\mathrm{G1\_sig\_d0pi}}$	2.010492 ± 0.000054	-
$\lambda_{\mathrm{J\_sig\_d0pi}}$	$0.00020168 \pm 0.00000053$	-
$\lambda_{\mathrm{J\_sig\_d0}}$	0.0067 ± 0.000016	-
$\mu_{\mathrm{G\_kpi\_d0}}$	1.940694 ± 0.000054	-
$\lambda_{\mathrm{J\_kpi\_d0}}$	0.006072 ± 0.000095	-
$\gamma_{\mathrm{J\_kpi\_d0}}$	-1.814 ± 0.012	-

Table C.3: Measured values of the parameters obtained from the fit to $D^0 \to K^+K^-$ sample in Belle II data. The uncertainties are statistical only.